

**UCLA**

**UCLA Electronic Theses and Dissertations**

**Title**

Particle Manipulation in Viscous Streaming

**Permalink**

<https://escholarship.org/uc/item/27h0j2b0>

**Author**

Chong, Kwitae

**Publication Date**

2013

Peer reviewed|Thesis/dissertation

UNIVERSITY OF CALIFORNIA  
Los Angeles

# **Particle Manipulation in Viscous Streaming**

A dissertation submitted in partial satisfaction  
of the requirements for the degree  
Doctor of Philosophy in Mechanical Engineering

by

**Kwi Tae Chong**

2013

© Copyright by  
Kwi Tae Chong  
2013

## ABSTRACT OF THE DISSERTATION

# Particle Manipulation in Viscous Streaming

by

**Kwi Tae Chong**

Doctor of Philosophy in Mechanical Engineering

University of California, Los Angeles, 2013

Professor Jeff Eldredge, Chair

The necessity of micromanipulation to separate, focus and transport discrete objects on a microscopic scale has emerged in recent years in areas from assisted fertilization to precision machining. This work explores the manipulation of microparticles suspended in viscous streaming flow. Streaming is a steady large-scale circulatory flow generated by the nonlinear interaction of the primary oscillatory motion. The first part of the study focuses on particle transport and trapping in the streaming flow generated by a single oscillating cylinder. The streaming flow is obtained by asymptotic expansion from previous work and the resulting velocity field is used to integrate the Maxey-Riley equation with the Saffman lift for the motion of an inertial spherical particle immersed in this flow. It is found that inertial particles spiral inward and become trapped inside one of the four streaming cells established by the cylinder oscillation, regardless of the particle size, density and flow Reynolds number. It is shown that the Faxén correction terms divert the particles from the fluid particle trajectories, and once diverted, the Saffman lift force is most responsible for effecting the inward motion and trapping. Results compare favorably with previous experiments.

We extend this study to various arrangements of oscillating probes. High fidelity computations are used to simulate the flow field to capture particle transport. It is shown that, by controlling the sequence of starting and stopping the

oscillation of individual probes, inertial particles can be transported in a predictable manner between trapping points. In order to reduce the considerable expense of generating the flow field, we also explore the use of steady Stokes flow to serve as an approximate surrogate for the flow between probes. The boundary conditions for this flow are obtained by matching with the inner Stokes layer solution in the asymptotic expansion for small amplitude. Finally, the practical characteristics of transport by streaming are discussed.

Overall, this study reveals that viscous streaming is an effective mechanism with which to manipulate small particles. To the best of my knowledge, this work is the first to investigate inertial particle trapping and transport in viscous streaming theoretically and computationally.

The dissertation of Kwi Tae Chong is approved.

Xiaolin Zhong

Pirouz Kavehpour

Dino Di Carlo

Jeff Eldredge, Committee Chair

University of California, Los Angeles

2013

To my wife...

# TABLE OF CONTENTS

<b>1</b>	<b>Introduction . . . . .</b>	<b>1</b>
1.1	Non-Contacting micromanipulation . . . . .	2
1.2	Hydrodynamic micromanipulation . . . . .	4
1.3	Viscous Streaming . . . . .	5
1.4	Preview of Paper . . . . .	9
<b>2</b>	<b>Problem Statement . . . . .</b>	<b>11</b>
2.1	Governing Equation and Boundary Condition . . . . .	13
2.1.1	First-order solution . . . . .	14
2.1.2	Second-order solution . . . . .	16
2.2	Change of Reference Frame . . . . .	19
2.3	Lagrangian and Eulerian System . . . . .	23
<b>3</b>	<b>Methodology . . . . .</b>	<b>26</b>
3.1	Viscous Vortex Particle Method (VVPM) . . . . .	28
3.1.1	Basic Equations . . . . .	30
3.1.2	Vortex Method . . . . .	30
3.1.3	Particle Convection and Stretching . . . . .	32
3.1.4	Particle Strength Exchange . . . . .	33
3.1.5	Vortex Sheet and Diffusion . . . . .	33
3.1.6	Particle Redistribution . . . . .	36
3.2	Boundary Element Method (BEM) . . . . .	38
3.3	Validation of VVPM and BEM . . . . .	40



3.4	Computation of Inertial Particle Trajectory . . . . .	46
<b>4</b>	<b>Inertial Particle Trapping . . . . .</b>	<b>51</b>
4.1	Inertial Particle Trapping . . . . .	51
4.2	Inertial particle Trapping Mechanism . . . . .	55
4.3	Inertial particle trapping speed . . . . .	63
4.4	Inner and outer streaming . . . . .	66
<b>5</b>	<b>Inertial Particle Transport . . . . .</b>	<b>68</b>
5.1	Problem Statement . . . . .	68
5.2	Modified Maxey-Riley Equation . . . . .	82
5.3	Transport inside Stokes layer . . . . .	85
5.4	Transport outside Stokes layer . . . . .	90
<b>6</b>	<b>Conclusion and Future Works . . . . .</b>	<b>98</b>
<b>A</b>	<b>Analytical Solution of Coefficient Matrix . . . . .</b>	<b>101</b>
	<b>References . . . . .</b>	<b>103</b>

## LIST OF FIGURES

1.1	Schematic of vorticella [83]. . . . .	5
1.2	(Left) Lagrangian streamlines (top half) and instantaneous Stokes-layer vorticity (bottom half) of canonical streaming pattern for $Re \gg 1$ and $Re_s \ll 1$ (here, $Re = 80$ ). (Right) Streaming regimes (adapted from Wang[85]). . . . .	6
2.1	Oscillating two-dimensional cylinder of radius $R$ with amplitude $A$ .	12
2.2	Instantaneous contour of (a) streamline (b) vorticity for First-order solution at $t\Omega = \pi/4$ . . . . .	15
2.3	Contour of (a) streamline (b) vorticity for second-order steady solution and instantaneous contour of (c) streamline (d) vorticity for second-order oscillatory solution at $t\Omega = \pi/4$ . . . . .	17
2.4	Mean vorticity along 45 degree line from 2nd order steady solution (blue solid line) and matched asymptotic analysis of Schlichting (black dot). . . . .	18
2.5	Instantaneous contour of (a) streamline (b) vorticity for First-order solution at $t\Omega = \pi/4$ in a inertial reference frame . . . . .	21
2.6	Contour of (a) streamline (b) vorticity for second-order steady solution and instantaneous contour of (c) streamline (d) vorticity for second-order oscillatory solution at $t\Omega = \pi/4$ in inertial reference frame . . . . .	22
2.7	(a) Mean Eulerian streamlines and (b) mean Lagrangian streamline for $Re = 40$ . . . . .	25

3.1	Velocity history (a) and time averaged velocity history (b) of VVPM for $A/R = 0.1$ and $Re = 40$ at $(\sqrt{2}R, \sqrt{2}R)$ during $t/T \in [0, 20]$ . Black dashed line denotes the Holtsmark's analytical solution. Blue and green indicates the VVPM simulation for $dx = 0.01$ and $dx = 0.02$ , respectively. . . . .	41
3.2	Contour of steady Eulerian streamlines from (a) analytical solution and VVPM of (b) $dx = 0.02$ , $tol = 10^{-7}$ , $\omega_{tol} = 2.5 \times 10^{-4}$ , (c) $dx = 0.01$ , $tol = 10^{-9}$ , $\omega_{tol} = 1.0 \times 10^{-5}$ , (d) $dx = 0.01$ , $tol = 10^{-10}$ , $\omega_{tol} = 1.0 \times 10^{-6}$ . . . . .	42
3.3	Mean vorticity along 45 degree line from matched asymptotic analysis of Schlichting (black dot) and VVPM of $dx = 0.02$ , $tol = 10^{-7}$ , $\omega_{tol} = 2.5 \times 10^{-4}$ (blue), $dx = 0.01$ , $tol = 10^{-9}$ , $\omega_{tol} = 1.0 \times 10^{-5}$ (red) and $dx = 0.01$ , $tol = 10^{-10}$ , $\omega_{tol} = 1.0 \times 10^{-6}$ (cyan). Matched asymptotic analysis and initial portion of VVPM simulations indicate decaying in order of $O(r^{-2})$ . . . . .	43
3.4	Contour of (a) streamline and (b) vorticity from Boundary Element Methods . . . . .	44
3.5	Mean vorticity along 45 degree line from matched asymptotic analysis of Schlichting (black dot) and BEM (blue). . . . .	45
4.1	Inertial particle trajectory (in red) based on trajectory sampled once per cycle (blue dots) for $Re = 40$ , $a/R = 0.175$ and $\rho_p/\rho_f = 1$ . . . . .	52

4.2	Inertial particles trajectories (in blue), sampled once per cycle, for $Re = 40$ , $a/R = 0.175$ . Initial locations depicted with blue circles. (a) $\rho_p/\rho_f = 1.05$ , (b) 1, (c) 0.95. In (b), red squares denote the instants $t/T = 290$ and 350. Lagrangian streamlines are depicted in light gray. (d) Inertial (red) and fluid (green) particle trajectories over one oscillation cycle, $t/T \in [317, 318]$ for $\rho_p/\rho_f = 1$ . Black arrows depict the total hydrodynamic force vectors in equation (3.45). Blue dots denote inertial particle trajectory sampled once per cycle. . . . .	53
4.3	Comparison of trapping position from current results (red squares) and experiments (blue circles) of Lutz <i>et al.</i> [45]. Dashed and solid lines depict, respectively, inner streaming cell size $\delta_{DC}/R$ and inner streaming cell center location. . . . .	54
4.4	Illustration of the tendency of a inertial particle to deviate from a Lagrangian streamline. Note that $\alpha < 0$ in the upper right portion of the streamline, and $\alpha > 0$ in the lower left portion. . . . .	56
4.5	(a) History of $\alpha$ during the cycle $t/T \in [290, 350]$ for $Re = 40$ , $a/R = 0.175$ , $\rho_p/\rho_f = 1$ . (b) Contributions to $d\alpha/dt$ from each term in equation (4.5): Stokes drag (black); convective term (cyan); Basset history (magenta); Saffman lift (blue); Faxén corrections (green); $\overline{\mathbf{w}} \times d\overline{\mathbf{U}}/dt$ (yellow). . . . .	59
4.6	Hydrodynamic force (black arrows) at sampled times along the inertial particle trajectory (blue solid line) during the intervals $t/T \in [0, 485]$ and $t/T \in [1300, 1370]$ for $Re = 40$ , $a/R = 0.175$ and $\rho_p/\rho_f = 1$ . All portions of the inertial particle trajectory not in these intervals are shown as a blue dotted line. . . . .	60

4.7	Saffman lift force (black arrow), relative particle velocity, $\mathbf{w}$ (green arrow), and local profile of fluid velocity, $\mathbf{u}$ , perpendicular to $\mathbf{w}$ (blue arrows) at $t/T = 317.5$ and $t/T = 318$ . Velocity vectors are plotted with the same scale. Red line denotes the inertial particle trajectory during the oscillation cycle $t/T \in [317, 318]$ . Local fluid particle trajectories, sampled once per period, shown with blue dots.	61
4.8	The final limit cycle for inertial particles of various sizes: $a/R = 0.1$ (blue); $a/R = 0.115$ (red); $a/R = 0.13$ (green); $a/R = 0.145$ (cyan); $a/R = 0.16$ (black); $a/R = 0.175$ (magenta), each plotted over one cycle for $Re = 40$ , $\rho_p/\rho_f = 1$ . Mean Lagrangian streamlines shown in gray for reference.	63
4.9	(a) The sampled history of the $x$ position of an inertial particle (- - -) and an exponential fit to the envelope (—), for $Re = 40$ , $\rho_p/\rho_f = 1$ and $a/R = 0.175$ . (b) Trapping timescale dependence on $a/R$ , for $Re = 40$ , $\rho_p/\rho_f = 1$ . This figure contains results for $\epsilon = 0.2\sqrt{2}$ (green triangles), 0.2 (blue circles), 0.1 (red squares). (c) Trapping timescale dependence on $\rho_p/\rho_f$ for $Re = 40$ , $a/R = 0.175$ . (d) Trapping timescale dependence on $Re$ for $\rho_p/\rho_f = 1$ , with $a/R$ varied so that $\Omega a^2/\nu$ is fixed at 1.2.	65
4.10	Inertial particle trajectories at $Re = 80$ for particle of density $\rho_p/\rho_f = 1$ and radius $a/R = 0.175$ , initially located at $(1.2R, 1.2R)$ ( $\circ$ ), $(1.8R, 1.8R)$ ( $\square$ ), $(2R, 2R)$ ( $\triangle$ ), $(2.2R, 2.2R)$ ( $\diamond$ ). Lagrangian streamlines are in light gray.	66

5.1	Schematic of two oscillating cylinders and the sequence of their oscillations. (a) Oscillating two-dimensional cylinders with amplitude $A_1$ , $A_2$ and frequency $\Omega_1$ , $\Omega_2$ . (b) Sequence of oscillating cylinders in VVPM. Streaming flow is generated by left cylinder until $t/T = t_{s1}$ (blue solid line) and one oscillating cycle is then used to integrate inertial particle trajectory until it is finally trapped at $t/T = t_{f1}$ (blue dot line). Right cylinder start to oscillate at $t/T = t_{f1}$ and generate streaming flow until $t/T = t_{s2}$ (red solid line). Every cycle during $t/T = t_{f1} \sim t_{s2}$ and then one oscillating cycle is used to compute the transport of trapped inertial particle until it is trapped in newly established streaming cell by right cylinder at $t/T = t_{f2}$ (red dot line). . . . .	69
5.2	Schematic of oscillating cylinders in triangular arrangement and the sequence of their oscillations. (a) Oscillating two-dimensional cylinders of with amplitude $A_1$ , $A_2$ , $A_3$ and frequency $\Omega_1$ , $\Omega_2$ , $\Omega_3$ . (b) Sequence of oscillating cylinders in VVPM is similar to sequence of two cylinders in figure 5.1 (b). . . . .	70
5.3	Schematic of oscillating cylinders in line arrangement and the sequence of their oscillations. (a) Oscillating two-dimensional cylinders of with amplitude $A_1$ , $A_2$ , $A_3$ and frequency $\Omega_1$ , $\Omega_2$ , $\Omega_3$ . (b) Sequence of oscillating cylinders in VVPM is similar to sequence of two cylinders in figure 5.1 (b). . . . .	71
5.4	Schematic of oscillating cylinders in zigzag arrangement and the sequence of their oscillations. (a) Oscillating two-dimensional cylinders of with amplitude $A_1$ , $A_2$ , $A_3$ , $A_4$ and frequency $\Omega_1$ , $\Omega_2$ , $\Omega_3$ , $\Omega_4$ . (b) Sequence of oscillating cylinders in VVPM is similar to sequence of two cylinders in figure 5.1 (b). . . . .	72

5.5	Contour of streamline of oscillating two cylinders from VVPM . Streaming flows are obtained from oscillation of (a) left $(-4R, 0)$ and (b) right $(4R, 0)$ cylinder, respectively. . . . .	74
5.6	Contour of streamline of oscillating cylinders in triangular arrange- ment from VVPM. Streaming flows are obtained from oscillation of (a) lower left $(-4R, 0)$ , (b) lower right $(4R, 0)$ and (c) upper $(0, 6R)$ cylinder, respectively. . . . .	77
5.7	Contour of streamline of oscillating cylinders in line arrangement from VVPM. Streaming flows are obtained from oscillation of (a) left $(-8R, 0)$ , (b) center $(0, 0)$ and (c) right $(8R, 0)$ cylinder, respec- tively. . . . .	78
5.8	Contour of streamline of oscillating cylinders in line arrangement from VVPM. Streaming flows are obtained from oscillation of (a) upper left $(-9R, -3R)$ , (b) lower left $(-3R, -3R)$ , (c) upper right $(3R, 3R)$ and (d) lower right $(9R, -3R)$ cylinder, respectively. . .	79
5.9	History of velocities, $\mathbf{U}_x$ and $\mathbf{U}_y$ at (a) $(-2R, 2R)$ , (b) $(0, 2R)$ and (c) $(2R, 2R)$ during $t/T = 0 \sim 40$ . . . . .	80
5.10	History of averaged velocities over one period oscillation, $\overline{\mathbf{U}}_x$ and $\overline{\mathbf{U}}_y$ at (a) $(-2R, 2R)$ , (b) $(0, 2R)$ and (c) $(2R, 2R)$ during $t/T =$ $0 \sim 40$ . . . . .	81
5.11	Inertial particle trajectory from complete MR (blue line) and MLV (red line) for $Re = 40$ , $A/R = 0.1$ , $a/R = 0.175$ and $\rho_p/\rho_f = 1$ . Each open circles and squares are positions of inertial particles at $t/T = 0$ and 21316, respectively. . . . .	85

5.12	Inertial particle trajectory during the cycle $t/T \in [0, 6784]$ (oscillation from left cylinder; blue line) and $t/T \in [6785, 105963]$ (oscillation from right cylinder; red line) for $Re = 40$ , $\epsilon = 0.1$ , $a/R = 0.175$ and $\rho_p/\rho_f = 1$ . Initial location depicted with blue circle. . . . .	86
5.13	Inertial particle trajectory during the cycle $t/T \in [0, 6784]$ (oscillation from lower left cylinder; blue line), $t/T \in [6785, 105109]$ (oscillation from lower right cylinder; red line) and $t/T \in [105110, 162754]$ (oscillation from upper cylinder; green line) for $Re = 40$ , $\epsilon = 0.1$ , $a/R = 0.175$ and $\rho_p/\rho_f = 1$ . Initial location depicted with blue circle. . . . .	87
5.14	Inertial particle trajectory during the cycle $t/T \in [0, 6784]$ (oscillation from left cylinder; blue line), $t/T \in [6785, 105109]$ (oscillation from center cylinder; red line) and $t/T \in [105110, 441381]$ (oscillation from right cylinder; green line) for $Re = 40$ , $\epsilon = 0.1$ , $a/R = 0.175$ and $\rho_p/\rho_f = 1$ . Initial location depicted with blue circle. . . . .	88
5.15	Inertial particle trajectory during the cycle $t/T \in [0, 5891]$ (oscillation from upper left cylinder; blue line), $t/T \in [5892, 88198]$ (oscillation from lower left cylinder; red line), $t/T \in [88199, 202499]$ (oscillation from upper right cylinder; green line) and $t/T \in [202500, 306366]$ (oscillation from lower right cylinder; magenta line) for $Re = 40$ , $\epsilon = 0.1$ , $a/R = 0.175$ and $\rho_p/\rho_f = 1$ . Initial location depicted with blue circle. . . . .	89
5.16	Contour of streamline of oscillating two cylinders from BEM . Streaming flows are obtained from oscillation of (a) left $(-4R, 0)$ and (b) right $(4R, 0)$ cylinder, respectively. . . . .	91



5.17	Contour of streamline of oscillating cylinders in triangular arrangement from BEM. Streaming flows are obtained from oscillation of (a) lower left $(-4R, 0)$ , (b) lower right $(4R, 0)$ and (c) upper $(0, 6R)$ cylinder, respectively. . . . .	92
5.18	Contour of streamline of oscillating cylinders in line arrangement from BEM. Streaming flows are obtained from oscillation of (a) left $(-8R, 0)$ , (b) center $(0, 0)$ and (c) right $(8R, 0)$ cylinder, respectively.	93
5.19	Contour of streamline of oscillating cylinders in line arrangement from BEM. Streaming flows are obtained from oscillation of (a) upper left $(-9R, -3R)$ , (b) lower left $(-3R, -3R)$ , (c) upper right $(3R, 3R)$ and (d) lower right $(9R, -3R)$ cylinder, respectively. . .	94
5.20	Inertial particle trajectory during the cycle $t/T \in [0, 15934]$ (oscillation from left cylinder; blue line) and $t/T \in [15934, 26388]$ (oscillation from right cylinder; red line) for $Re = 40$ , $\epsilon = 0.1$ , $a/R = 0.175$ and $\rho_p/\rho_f = 1$ . Particle's Initial location and transient location at $t/T = 15934$ is depicted with blue circle and red square, respectively.	95
5.21	(a) History of $\alpha$ during the cycle $t/T \in [120, 240]$ for $Re = 40$ , $a/R = 0.175$ , $\rho_p/\rho_f = 1$ . (b) Contributions to $d\alpha/dt$ from each term in equation (4.5): Stokes drag (black); convective term (cyan); Saffman lift (blue); Faxén corrections (green); $\overline{\mathbf{w}} \times d\overline{\mathbf{U}}/dt$ (yellow).	97
A.1	Geometry of boundary segment $\partial\Omega_j$ and notations for analytic solution of integration. . . . .	102

## LIST OF TABLES

4.1	Time averaged forces applied on the inertial particle during the interval $t/T \in [4200, 4700]$ for $Re = 40$ , $a/R = 0.175$ , $\rho_p/\rho_f = 1$ . . .	62
-----	--	----

## ACKNOWLEDGMENTS

I owe a great debt of gratitude to my advisor, Professor Jeff Eldredge for making my journey successful. He provided me unrestricted attention and wealth of experience and much encouragement to move forward whenever I faced unresolved difficulties. This dissertation would not have been possible without his intellectual and personnel support and guidance. I am also grateful to my colleague at UNCC, Professor Scott Kelly and Stuart Smith and Dr. Phanindra Tallapragada for their many helpful discussions.

I also thank the committee members: Professor Xiaolin Zhong, Pirouz Kavehpour and Dino Di Carlo. I also would like to thank the gracious support from NSF, CMMI for making my doctoral study possible. I also appreciate my friends and colleague at UCLA who provided me their wonderful times and shared their valuable experiences with me.

Of course, I thank my family who has given me unconditional love and support. Most importantly, I would like to thank my wife and best friend, Boyoung, who has provided me with her unlimited love, support and devotion. I could not have done this without you!!

## VITA

2006	Bachelors of Science (Mechanical Engineering), Seoul National University, South Korea.
2008	Masters of Science (Mechanical Engineering), Seoul National University, South Korea.
2006-2008	Graduate Student Researcher, Thermal Engineering in Manufacturing Process Laboratory, Seoul National University, South Korea.
2008-2013	Graduate Student Researcher, Simulations of Flow Physics and Acoustics Laboratory, University of California, Los Angeles.
2009-2010	Teaching Assistant, University of California, Los Angeles.

## PUBLICATIONS

K. Chong, S. D. Kelly, S. Smith and J. D. Eldredge [2013], “Inertial particle trapping in viscous streaming”, *Phys. Fluids*, 25, 033602

J. D. Eldredge and K. Chong [2010], “Fluid transport and coherent structures of translating and flapping wings”, *Chaos*, 20: 017509

# CHAPTER 1

## Introduction

Techniques for separating, focusing and transporting small-sized particles in an aqueous environment have matured in recent years, motivated primarily by technology needs such as drug delivery, cell processing and microfluidic devices. This techniques, so called micromanipulation, can be categorized largely into direct contact methods and non contacting methods. The direct contact methods can be classified further into aspirating type [59, 75, 64] and pressing type [60, 92, 86, 39]. Since these method directly contact with the object they may place a undesirable mechanical stress on delicate object such as living cells, which can affect the measurement of the object and even adversely affect the functionality of the object.

On the other hand the non contacting system is able to orientate, transport and manipulate the object without physical contact with the object. Some of the most notable and effective methods are based on lasers [3, 51, 13], ultrasonics [29, 27], dielectrophoresis [31, 55] and inertial hydrodynamic effects [20, 21]. Another appealing option for particle manipulation is based on the notion of steady streaming. A streaming flow is a relatively weak but large-scale steady response of a fluid to non-linear interactions – the Reynolds stresses – in a primary oscillatory flow. Such a flow can arise in both viscous and acoustic environments. The promise of such a flow for trapping and manipulating microparticles has recently been demonstrated by a number of recent studies [44, 45, 40, 47, 48, 84, 46]. These recent works demonstrate the excellent opportunities for particle manipulation using streaming flows.

In this work, we are interested in obtaining a deeper understanding of the behavior of a canonical streaming flow (the flow generated by an oscillating circular cylinder), and particularly, the interaction of small inertial particles with such a flow. Though it is known that particles can be trapped by the streaming, relatively little is known about the nature or conditions under which this trapping is possible. Here, our objective is to provide more physical intuition and to determine the dependence on various parameters, such as Reynolds number, and particle size and relative density. Based on this inertial particle trapping mechanism by streaming flow generated by oscillating object, inertial particle transport between oscillating cylinders will be investigated using high-fidelity computational simulations or approximated flows of Boundary Element Method.

## 1.1 Non-Contacting micromanipulation

The non-contacting micromanipulation can be largely categorized into laser-based system, ultrasonic system and dielectrophoresis system. The non-contacting system has a noticeable advantage over direct-contact systems in a sense that since they do not directly contact with the objects they do not place a undesirable mechanical stress on the objects which has a adverse effect on living cells and perturbs the cell behavior. This system however inherently relies on conditions far outside the physiological range for living cells resulting from a tightly focused laser beam or high-frequency ultrasonic energy and their effects on the cell behavior and viability are still disputable. Moreover this system is generally sophisticated and the control over systems can be complicated by variations in the physical properties [45].

The Laser-based micromanipulation was firstly proposed as a optical tweezer by Ashkin [3]. He showed that the Micron-sized particles was accelerated and trapped in optical potential wells using the radiation pressure force from a tightly focused laser beam. If the laser beam hits the sphere particle, the laser beam

undergoes deflection and reflection and these results in radiation pressure forces, which drive the particle in the direction of net radiation pressure force. Therefore, the sphere particle can be trapped when the laser beam hits the sphere from both direction, which results in zero net force. Although this Laser system is best-known and most widely used method, the particle can only be manipulated after the position of particle is identified and there exist limitation of particle sized since the wavelength of laser beam should be similar to the particle diameter.

However the ultrasonic system differs by two or more orders of magnitude in particle size [27]. The acoustical tweezer is a representative of a ultrasonic micromanipulation system. Wu [89] used two collimated focused ultrasonic (3.5 MHz) beams generated from transducers propagating along opposite directions, which generated force potential well. He observed that a latex particle of  $270\text{--}\mu\text{m}$  diameter or clusters of frog eggs can be trapped in the potential well. He showed that by axially or laterally moving either one of the transducers the potential well and hence the trapped objects can easily be moved. He also presented that the clusters of frog eggs can readily be maneuvered by changing the frequency of the transducer. The work of Wu [89] is based on two ultrasonic standing wave with same frequency. This method makes it difficult to localize small objects at the desired point as many nodes and anti-nodes are usually generated inside the standing wave [91]. Yamakoshi [91] used two traveling ultrasonic waves with opposite phases of 0 and  $\pi$  radian which generate an acoustic black line with zero acoustics power in front of the boundary of the two ultrasonic transducers. This acoustic black line modulates the acoustic field spatially and hence generate the acoustical radiation force which trap the particles.

Nieuwenhuis et al. [55] represented microfluidic devices that can sort particles based on dielectrophoresis that is the phenomenon which a particle in non-uniform electric field experiences a force proportional to the gradient of this electric field. In this device the particles in fluid is sent into either left or right branch based on

the dielectrophoresis. They also focused on the optimized layout of the sorters to make dielectrophoretic flow-through particle sorter suitable for higher flow speed.

## 1.2 Hydrodynamic micromanipulation

Due to the complexity of experiment and the extreme physiological conditions for living cells of the methods described above there is continuing need to develop the alternative micromanipulation. It was observed that the alternative micromanipulation is made feasible through viscous streaming. Figure 1.1 depicts a vorticella which is common to freshwater ponds and streams. The vorticella creates vortical structures around it's bell by continuously beating its cilia to introduce vortex flow and direct the food into bell. The enhancement of molecular exchange rate by a beating surface-mounted flagella [76] and the mixing property of vorticella and thereby the fabrication of micromixer in microchannel using a vorticella [?] was studied. These studies imply that transporting and mixing a particle in fluid is made possible through changing the fluid boundary.

Lutz *et al.* [44, 45] created streaming eddies around a cylinder fixed in a microchannel through which fluid was oscillated, and showed that particles both lighter and heavier than the surrounding fluid could be trapped inside the streaming eddies; Lieu *et al.* [40] recently characterized the trapping in the vicinity of other obstacles, and a cavity, as well. These studies also showed that trapping was less effective when the particle was much much smaller than the cylinder.

Marmottant and Hilgenfeldt [47] exhibited controlled vesicle deformation and lysis using a single oscillating microbubble mounted on the wall of a microchannel. The shear force on the vesicles due to the streaming flow was strong enough to deform and rupture them. They also demonstrated microparticle transport based on a controlled fluid motion created through combinations of oscillating bubbles [46, 48]. Wang *et al.* [84] have recently demonstrated the size-selective trapping



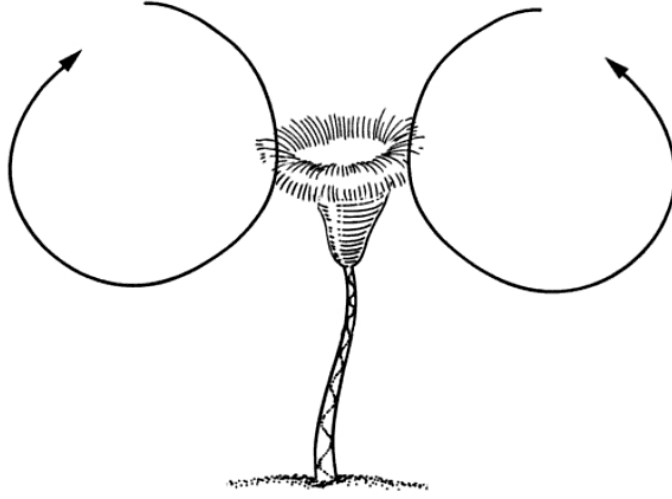


Figure 1.1: Schematic of vorticella [83].

and release of microparticles through a superposition of bubble-induced streaming and Poiseuille flow.

These studies also imply that the experiments in the researches are simple and easy to implement and experimental condition is moderate, which means that viscous streaming generated by oscillating the fluid boundary can avoid the complexity of experimental systems and create survivable physiological conditions for living cells and do not perturb the cell behavior and thereby make the micromanipulation feasible. The viscous streaming is closely reviewed in next section.

### 1.3 Viscous Streaming

The study of steady streaming dates to Lord Rayleigh, who found the existence of a steady flow in Kundt's tube [66]. Early experimental studies of viscous streaming in the vicinity of a circular cylinder (and other obstacles) were conducted by Andrade [1], who mounted the cylinder in an apparatus through which air was driven sinusoidally. Smoke was used to visualize the cloverleaf pattern of streaming cells. Schlichting [74] examined the same flow, generated in this case by an

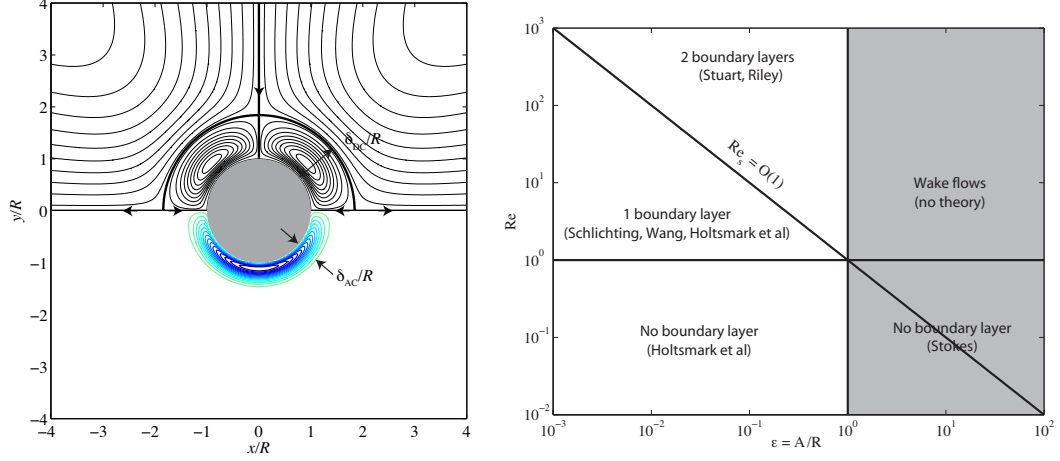


Figure 1.2: (Left) Lagrangian streamlines (top half) and instantaneous Stokes-layer vorticity (bottom half) of canonical streaming pattern for  $Re \gg 1$  and  $Re_s \ll 1$  (here,  $Re = 80$ ). (Right) Streaming regimes (adapted from Wang[85]).

oscillating cylinder in an otherwise quiescent medium. His study was notable for providing a theoretical analysis of the flow, based on an expansion in the ratio  $\epsilon$  of small oscillation amplitude  $A$  to cylinder radius  $R$ . The analysis was performed in a reference frame attached to the oscillating body, so that the fluid at infinity is in uniform oscillation. Schlichting matched the inner flow solution – in which the relevant length scale is the thickness of the oscillatory (Stokes) boundary layer,  $\delta_{AC} = (\nu/\Omega)^{1/2}$ , where  $\nu$  is kinematic viscosity and  $\Omega$  is angular frequency of oscillation – with a corresponding expansion of the outer flow. The leading-order outer potential flow drives the Stokes layer near the cylinder, which applies a second-order correction to the outer flow due to displacement, which in turn affects the boundary layer at the next order, and so on. It is useful to note that the thickness of the Stokes layer is directly related to the Reynolds number based on cylinder radius:  $\delta_{AC}/R = 1/Re^{1/2}$ , where  $Re = \Omega R^2/\nu$ .

The steady component of the flow enters at second order, driven by the mean Reynolds stress of the leading-order Stokes layer. This steady flow is divided into

four equal quadrants about the cylinder by the axis of oscillation and the axis transverse to this oscillation (see the left panel of Figure 1.2, which also depicts the vorticity in the Stokes layer). Each quadrant exhibits a streaming cell, segregated from the outer flow by a dividing streamline at distance  $\delta_{DC}$  off the surface of the cylinder. The Reynolds stresses decay exponentially with distance from the cylinder surface, so the fluid outside the boundary layer is set in steady motion indirectly, effectively dragged along by the inner flow. The composite of these inner and outer flows represents the streaming flow.

Schlichting’s analysis provided an intuitive understanding of the flow that subsequent analyses have improved upon, but not significantly altered. Wang [85] argued that body curvature, which Schlichting neglected, should have an important influence on the boundary layer behavior; however, this influence is only felt at second order and higher in the oscillatory portion, and third order and higher in the steady portions of the flow, as revealed by Wang’s matched asymptotic analysis. Holtsmark *et al.* [30] also performed an asymptotic expansion in small amplitude ratio, but did not treat the inner and outer flows separately; rather, they solved for the entire flow about the cylinder at each order of accuracy. The results of Holtsmark *et al.* [30] contain those of Schlichting [74] and Wang [85] when one carries out an expansion of these results in powers of  $Re^{-1/2}$ , assuming that  $Re \gg 1$ ; however, the Holtsmark group’s result holds equally well for moderate and small  $Re$ , for which the oscillatory boundary layer is absent. Raney, Corelli, and Westervelt [65], and later Bertelsen, Svardal, and Tjøtta [7], corrected each of these results for the Stokes drift, which accounts for the difference between the steady Lagrangian streamlines (the mean paths followed by fluid particles) and the Eulerian streamlines (which are obtained from the mean streamfunction). Since most experimental measurements of the flow are based on tracking the motion of passive tracer particles, the Stokes drift is inherent to such experimental results. As is apparent from the experiments from Holtsmark *et al.* [30], and

corroborated by the drift-corrected theory [7], the relative thickness,  $\delta_{DC}/R$ , of the inner streaming cell exhibits a complex dependence on the Reynolds number, growing progressively larger as  $Re$  gets smaller and without bound as  $Re \rightarrow 37$ . Note that  $\delta_{DC}/\delta_{AC} > 1$  at all Reynolds numbers, as the left panel of Figure 1.2 indicates at the particular case of  $Re = 80$ .

Though the Reynolds number,  $Re$ , defines the size of the driving mechanism (the Stokes layer), the streaming flow itself is characterized by a streaming Reynolds number,  $Re_s = \Omega A^2/\nu$ . Its role is clear from the fact that the characteristic velocity of the streaming flow is  $V_s = \epsilon \Omega A$ , so  $Re_s = V_s R/\nu$ . Each of the analyses above was based on the assumption that  $Re_s \ll 1$ , whereupon the steady streaming flow beyond the inner layer is essentially Stokes flow (through second order). However, when  $Re_s \gg 1$ , this outer flow exhibits its own boundary layer structure, with a characteristic thickness of order  $R/Re_s^{1/2}$ . Since  $\delta_{AC} = R/Re^{1/2}$  and  $Re_s = \epsilon^2 Re$ , then this second boundary layer is much thicker than the Stokes layer (and the inner streaming cell,  $\delta_{DC}$ ). Both Riley [68] and Stuart [77] revealed the existence of such a double boundary layer structure at large streaming Reynolds number. Riley used matched asymptotic expansions of the inner and outer regions, while Stuart adopted a generalization of a series expansion method by Fettes [24].

The various streaming regimes in the  $\epsilon-Re$  parametric space were nicely summarized in a figure by Wang [85], which is presented in somewhat modified form here in the right panel of Figure 1.2. The streaming theories all fall to the left of  $\epsilon = O(1)$ , as the right side of this line involves large-amplitude motions, which, for  $Re \gg 1$  generate wake flows that resist analytical description, and for  $Re \lesssim 1$  are governed by quasi-steady Stokes flow. The regime of small streaming Reynolds number lies below the line that diagonally transects the figure.

## 1.4 Preview of Paper

In this work, we are primarily focused on the behavior of inertial particles (particles of finite size whose density may differ from that of the surrounding fluid) in streaming flows for which  $Re_s \lesssim 1$ ,  $\epsilon \ll 1$ , and  $Re = O(10)$  – that is, the cases for which the theoretical treatment of Holtsmark *et al.* [30] is valid. We will assume that the particle is a rigid sphere, and sufficiently small such that its ‘slip’ Reynolds number,  $Re_p = a|\mathbf{w}|/\nu$  (the Reynolds number based on the velocity of the particle relative to the local undisturbed flow,  $\mathbf{w}$ , and particle radius,  $a$ ) and shear Reynolds number,  $Re_G = a^2 G/\nu$  (the Reynolds number based on the velocity gradient,  $G$ ) are both much less than unity. The translation of a rigid sphere in this regime was originally treated separately by Basset [4], Boussinesq [9] and Oseen [57] (and hence the equation governing its dynamics is sometimes called the ‘BBO’ equation). Later, Maxey and Riley [49] proposed a corrected equation of motion for a small rigid sphere in a nonuniform flow. We will make use of the equation derived in this latter work, including the Saffman lift force term [73] (and refer to it from hereon as the Maxey–Riley, or simply ‘MR’ equation) in order to calculate trajectories of inertial particles in the flows predicted by the Holtsmark solution, and in the flows obtained from high-fidelity or approximated simulations.

The problem statement of this study as well as basic solutions of governing equation (Holtsmark solution) will be presented in chapter 2. Also the change of reference frame to an oscillating circular cylinder in a quiescent flow (This frame, in contrast to the one in which the cylinder is fixed in an oscillating flow, will enable opportunities for studying particle transport between multiple oscillators of possibly different frequencies.) and Lagrangian system correcting the Eulerian system with Stokes drift will be described in chapter 2. Streaming flow generated by multiple cylinder from high-fidelity simulation and approximated simulation is

described and validated in chapter 3. The Maxey–Riley equation for integrating inertial particle trajectory is also described in the same chapter.

Inertial particle trapping will be examined in chapter 4. The transient behavior of the inertial particle in the streaming cell, and the trapping speed and equilibrium trajectory will be examined in this section. Inertial particle transport inside and outside of Stokes layer with modified Maxey–Riley equation will be described in chapter 5. The conclusion and future works will be followed in chapter 6.

Most works of chapter 2 and 4 are based on the paper by Chong *et al.* [35].

## CHAPTER 2

### Problem Statement

In this chapter, I first consider the motion of inertial particles in a flow generated by a single two-dimensional circular cylinder of radius  $R$  that undergoes rectilinear sinusoidal oscillations along the  $x$  axis with amplitude  $A$  and angular frequency  $\Omega$  as shown in figure 2.1,

$$\mathbf{X}(t) = \mathbf{e}_x A \sin \Omega t, \quad (2.1)$$

in a quiescent incompressible medium of uniform density  $\rho_f$  and kinematic viscosity  $\nu$ . The  $y$  axis represents the transverse direction in the plane of the cylinder cross-section, and the  $z$  axis is parallel to the cylinder axis. A particle has radius  $a$  and density  $\rho_p$ , where it is assumed that  $a$  is much smaller than the radius of the oscillating cylinder. However, for the purpose of mathematical simplicity and robustness, this solution will be derived by modifying the flow generated by a circular cylinder in an oscillatory free stream.

It is important to consider the wide range of time scales of this problem. Inertial particles are transported approximately at the characteristic (drift-corrected) speed of the streaming flow,  $V_s = \epsilon \Omega A$ , around a cell of characteristic size  $\delta_{DC}$ . Though this size varies with Reynolds number, as described above, it remains  $O(R)$  over a wide range of  $Re$ . Thus, the convective time for a particle to orbit the streaming cell is of order  $\delta_{DC}/V_s \sim R/(\epsilon \Omega A) = 1/(\epsilon^2 \Omega)$ , or  $\epsilon^{-2}$  periods of oscillation, and to discern long-term behavior of the particle, many such orbits must be captured. So in practice, particle trajectories must be computed over hundreds to thousands of oscillation cycles.

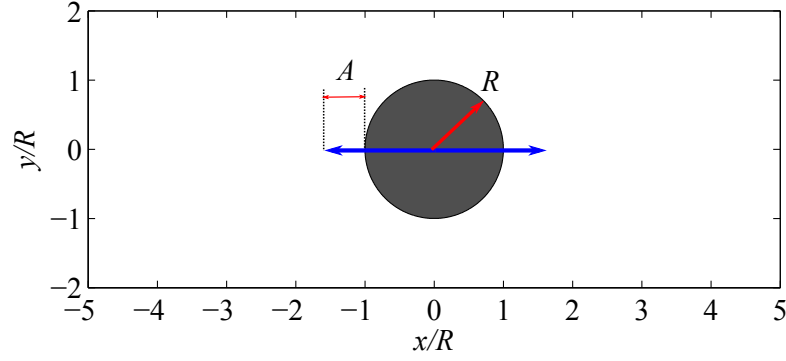


Figure 2.1: Oscillating two-dimensional cylinder of radius  $R$  with amplitude  $A$ .

It is also important to note the wide range of length scales of this problem. Vorticities are generated in thin Stokes layer of size  $\delta_{AC} = R/Re^{1/2}$  and diffused throughout the inner streaming cell of size  $O(R)$ . Inertial particles are transported inside inner streaming cell and over distance between oscillating cylinders of size  $O(R/\epsilon)$ . Hence, it is difficult but also important to consider wide range of time scales as well as length scales in order to correctly solve this problem.

The solution for the flow generated about a circular cylinder in an oscillatory free stream is derived in the following sections, and follows the derivation presented by Holtsmark *et al.* [30]. However, this earlier work contains errors in the second-order oscillatory part of the solution, and I correct these errors here. I also include a derivation of the Stokes drift of fluid particles in this flow. Then, in the last section, I discuss how this solution is modified when the reference frame is changed to one in which the cylinder is in motion and the fluid at rest at infinity. This reference frame is ultimate one in which inertial particles are manipulated in a flow field generated by oscillating object.



## 2.1 Governing Equation and Boundary Condition

As mentioned above, the flow field is obtained in a reference frame in which the cylinder is at rest and the fluid at infinity is in uniform oscillatory motion in the  $x$  direction, with velocity  $U(t) = -A\Omega \cos(\Omega t)$ . Then this solution is modified to the reference frame in which the cylinder is oscillating in a quiescent fluid in the following section. We seek the solution of the two-dimensional vorticity transport equation,

$$\frac{\partial}{\partial t}(\nabla^2 \psi) + \mathbf{u} \cdot \nabla(\nabla^2 \psi) = \nu \nabla^4 \psi \quad (2.2)$$

subject to the conditions

$$\psi = 0, \quad \frac{\partial \psi}{\partial r} = 0 \text{ at } r = R, \quad \psi \rightarrow -A\Omega r \sin \theta \cos \Omega t \text{ as } r \rightarrow \infty, \quad (2.3)$$

where the polar velocity components are defined as

$$u_r = \frac{1}{r} \frac{\partial \psi}{\partial \theta}, \quad u_\theta = -\frac{\partial \psi}{\partial r}. \quad (2.4)$$

From hereon, the variables are scaled by  $R$  and  $\Omega$ . We thereby arrive at the dimensionless form of the problem

$$\nabla^2 \left( \nabla^2 - Re \frac{\partial}{\partial t} \right) \psi = Re \mathbf{u} \cdot \nabla (\nabla^2 \psi), \quad (2.5)$$

and

$$\psi = 0, \quad \frac{\partial \psi}{\partial r} = 0 \text{ at } r = 1, \quad \psi \rightarrow -\epsilon r \sin \theta \cos t \text{ as } r \rightarrow \infty. \quad (2.6)$$

We introduce an asymptotic expansion in  $\epsilon$  for the streamfunction,

$$\psi = \epsilon \psi_1 + \epsilon^2 \psi_2 + O(\epsilon^3), \quad (2.7)$$

and thereby develop a hierarchy of problems for  $\psi_1$ ,  $\psi_2$ , etc. We will restrict our attention here to the first two,

$$\begin{aligned} \nabla^2 \left( \nabla^2 - Re \frac{\partial}{\partial t} \right) \psi_1 &= 0, \\ \psi_1 = 0, \quad \frac{\partial \psi_1}{\partial r} &= 0 \quad \text{at } r = 1, \quad \psi_1 \rightarrow -r \sin \theta \cos t \text{ as } r \rightarrow \infty \end{aligned} \quad (2.8)$$

and

$$\begin{aligned} \nabla^2 \left( \nabla^2 - Re \frac{\partial}{\partial t} \right) \psi_2 &= Re \mathbf{u}_1 \cdot \nabla (\nabla^2 \psi_1), \\ \psi_2 = 0, \quad \frac{\partial \psi_2}{\partial r} &= 0 \text{ at } r = 1, \quad \psi_2 \rightarrow 0 \text{ as } r \rightarrow \infty. \end{aligned} \quad (2.9)$$

### 2.1.1 First-order solution

The equation (2.8) for the first-order streamfunction is linear and homogeneous, and consists of a superposition of solutions of the two-dimensional Laplace equation and heat equation. This first-order solution comprises the forcing – via Reynolds stresses – for the second-order equation (2.9). It is interesting to note that, if the oscillatory motion of the cylinder were changed in sign (i.e. phase-shifted by  $\pi$ ), the second-order motion would be unaffected.

The solution of (2.8) can be written as

$$\psi_1(r, \theta, t) = \text{Re} \left( \Psi_1(r) e^{-it} \right) \sin \theta. \quad (2.10)$$

where the radial dependence can be split into two parts

$$\Psi_1(r) = \Psi_1^{(1)}(r) + \Psi_1^{(2)}(r), \quad (2.11)$$

each of which represents the homogeneous solution of one of the two differential operators in (2.8);  $\Psi_1^{(1)}$  is the radial dependence of the solution of the Laplace equation and  $\Psi_1^{(2)}$  of the heat equation. After applying boundary conditions, these solutions are, respectively,

$$\Psi_1^{(1)}(r) = -r - \frac{C}{r}, \quad (2.12)$$

$$\Psi_1^{(2)}(r) = \frac{2H_1^{(1)}(\gamma r)}{\gamma H_0^{(1)}(\gamma)} = r \left[ \frac{H_0^{(1)}(\gamma r)}{H_0^{(1)}(\gamma)} + \frac{H_2^{(1)}(\gamma r)}{H_0^{(1)}(\gamma)} \right], \quad (2.13)$$

where  $C = H_2^{(1)}(\gamma)/H_0^{(1)}(\gamma)$ . Note that  $H_1^{(1)}$  and  $H_1^{(2)}$  are the first-order Hankel functions of the first and second kind, respectively, and  $\gamma = (iRe)^{1/2}$ . When

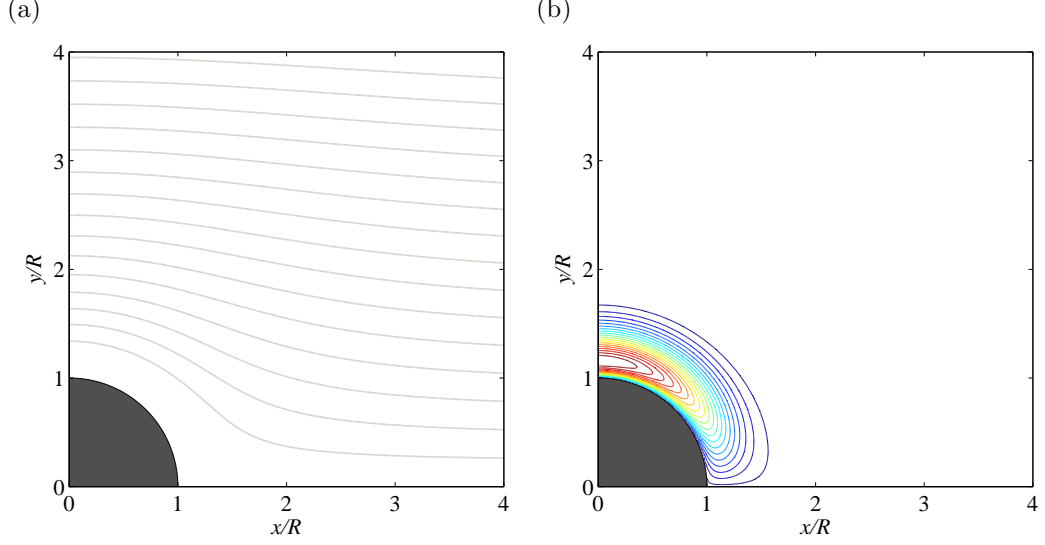


Figure 2.2: Instantaneous contour of (a) streamline (b) vorticity for First-order solution at  $t\Omega = \pi/4$

streamfunction is expressed in the inertial reference frame (in which the cylinder is in motion and the fluid at rest at infinity), the first term in (2.12) is cancelled by the first-order modification in the change of reference frame equation (2.31).

The velocity components associated with this first-order streamfunction are

$$u_{r,1} = \text{Re} \left( U_{r,1}(r) e^{-it} \right) \cos \theta \quad (2.14)$$

and

$$u_{\theta,1} = \text{Re} \left( U_{\theta,1}(r) e^{-it} \right) \sin \theta, \quad (2.15)$$

where  $U_{r,1} = \Psi_1/r$  and  $U_{\theta,1} = -d\Psi_1/dr$ . It is straightforward to show (using recurrence relations for Hankel functions) that

$$U_{r,1}(r) = -1 - \frac{C}{r^2} + \frac{H_0^{(1)}(\gamma r)}{H_0^{(1)}(\gamma)} + \frac{H_2^{(1)}(\gamma r)}{H_0^{(1)}(\gamma)}, \quad (2.16)$$

$$U_{\theta,1}(r) = 1 - \frac{C}{r^2} - \frac{H_0^{(1)}(\gamma r)}{H_0^{(1)}(\gamma)} + \frac{H_2^{(1)}(\gamma r)}{H_0^{(1)}(\gamma)}. \quad (2.17)$$

Figure 2.2 is a instantaneous contour of streamline and vorticity at  $t\Omega = \pi/4$  for first-order solution in (2.11) and depicts primary oscillatory flow corresponding

to the boundary conditions, which is oscillatory at infinity and no flow through at the surface of cylinder. This primary oscillating flow is combination of potential flow around circular cylinder ( $\Psi_1^{(1)}$  of Laplace equation) and rotational flow diffused by vorticity generated on the surface of cylinder ( $\Psi_1^{(2)}$  of the heat equation).

### 2.1.2 Second-order solution

The first-order solution can now be used to evaluate the forcing term in RHS of equation (2.9) for  $\psi_2$ .

$$Re \mathbf{u}_1 \cdot \nabla (\nabla^2 \psi_1) = \text{Re} (f_0(r) + g_0(r)e^{-i2t}) \sin 2\theta \quad (2.18)$$

where

$$f_0(r) = \frac{iRe^2}{4} \frac{1}{r} \left( \Psi_1 \frac{d\Psi_1^{(2)*}}{dr} - \Psi_1^{(2)*} \frac{d\Psi_1}{dr} \right), \quad (2.19)$$

and

$$g_0(r) = -\frac{iRe^2}{4r} \left( \Psi_1^{(1)} \frac{d\Psi_1^{(2)}}{dr} - \Psi_1^{(2)} \frac{d\Psi_1^{(1)}}{dr} \right). \quad (2.20)$$

It can be verified that this leads to a second-order solution of the form

$$\psi_2(r, \theta, t) = \text{Re} (\Psi_2^s(r) + \Psi_2(r)e^{-i2t}) \sin 2\theta, \quad (2.21)$$

where the radial dependence of the steady solution is

$$\begin{aligned} \Psi_2^s(r) = & -\frac{r^4}{48} \int_r^\infty \frac{f_0(\tau)}{\tau} d\tau + \frac{r^2}{16} \int_r^\infty \tau f_0(\tau) d\tau \\ & + \frac{1}{16} \left( \int_1^r \tau^3 f_0(\tau) d\tau + \int_1^\infty \frac{f_0(\tau)}{\tau} d\tau - 2 \int_1^\infty \tau f_0(\tau) d\tau \right) \\ & + \frac{1}{r^2} \left( -\frac{1}{48} \int_1^r \tau^5 f_0(\tau) d\tau - \frac{1}{24} \int_1^\infty \frac{f_0(\tau)}{\tau} d\tau + \frac{1}{16} \int_1^\infty \tau f_0(\tau) d\tau \right). \end{aligned} \quad (2.22)$$

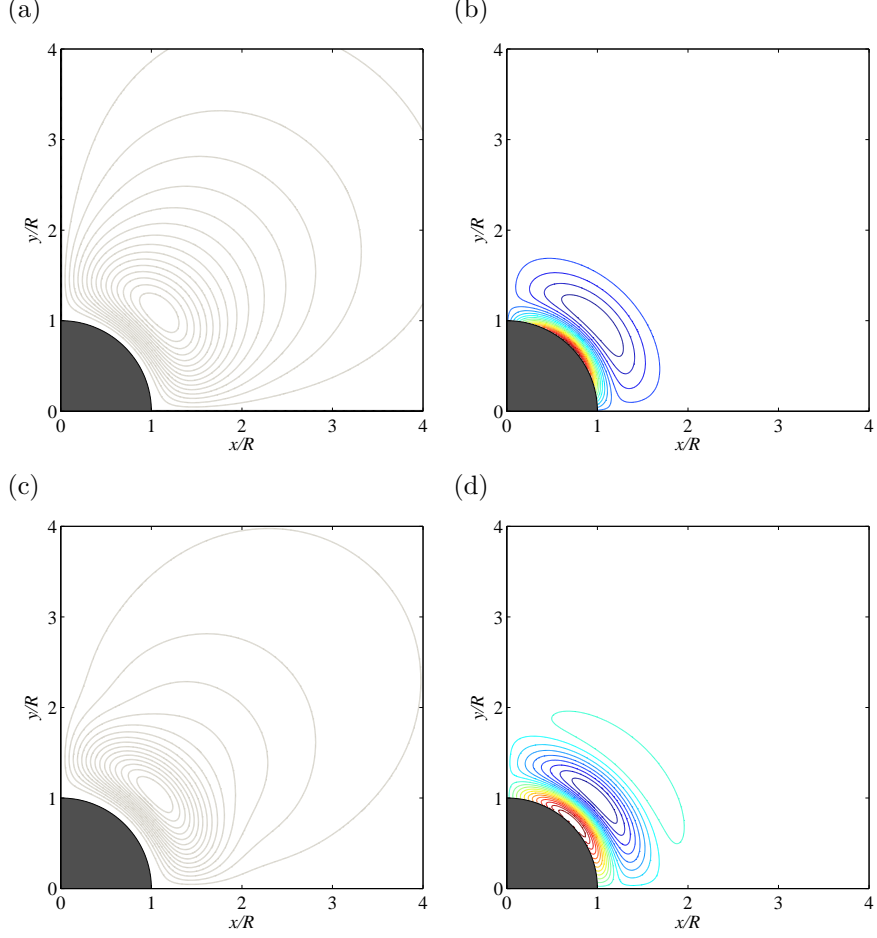


Figure 2.3: Contour of (a) streamline (b) vorticity for second-order steady solution and instantaneous contour of (c) streamline (d) vorticity for second-order oscillatory solution at  $t\Omega = \pi/4$

The radial dependence of the oscillatory portion is

$$\begin{aligned}
 \Psi_2(r) = & \frac{i\pi}{4\lambda^2 H_1^{(1)}(\lambda)} \left( H_2^{(1)}(\lambda r) \int_1^r \tau K_2(\lambda \tau) g_0(\tau) d\tau \right. \\
 & \left. + K_2(\lambda r) \int_r^\infty \tau H_2^{(1)}(\lambda \tau) g_0(\tau) d\tau \right) \\
 & + \frac{1}{\lambda^3 H_1^{(1)}(\lambda)} \left[ \left( H_2^{(1)}(\lambda r) - r^{-2} H_2^{(1)}(\lambda) \right) \int_1^\infty \frac{g_0(\tau)}{\tau} d\tau \right. \\
 & \left. + r^{-2} \int_1^\infty \tau H_2^{(1)}(\lambda \tau) g_0(\tau) d\tau \right] \\
 & - \frac{1}{4\lambda^2} \left( r^2 \int_r^\infty \frac{g_0(\tau)}{\tau} d\tau - r^{-2} \int_1^\infty \frac{g_0(\tau)}{\tau} d\tau + r^{-2} \int_1^r \tau^3 g_0(\tau) d\tau \right),
 \end{aligned} \tag{2.23}$$

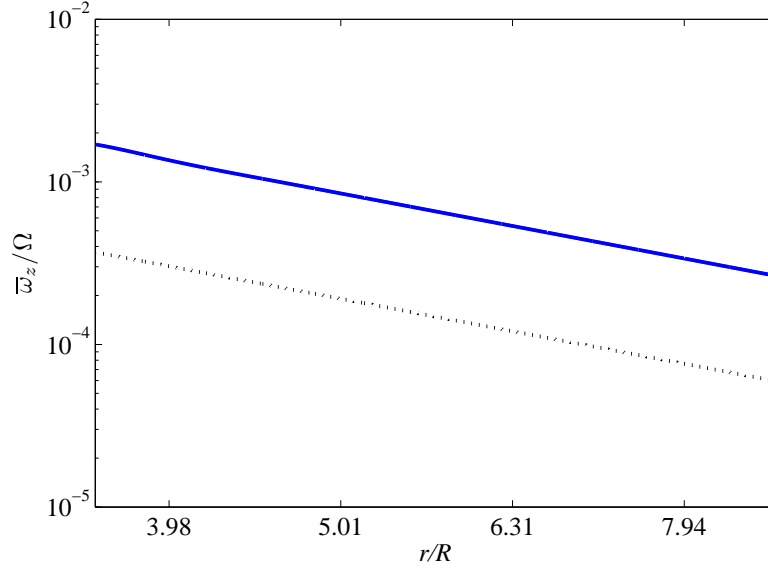


Figure 2.4: Mean vorticity along 45 degree line from 2nd order steady solution (blue solid line) and matched asymptotic analysis of Schlichting (black dot).

where  $\lambda = \sqrt{2}\gamma$ ,  $K_2(\lambda\tau) = H_1^{(1)}(\lambda)H_2^{(2)}(\lambda\tau) - H_1^{(2)}(\lambda)H_2^{(1)}(\lambda\tau)$ . We note that (2.24) corrects errors in the solution presented by Holtmark *et al.* [30].

The velocity components of the second-order solution are, correspondingly,

$$u_{r,2} = \text{Re} \left( \frac{2\Psi_2^s}{r} + \frac{2\Psi_2}{r} e^{-i2t} \right) \cos 2\theta \quad (2.24)$$

and

$$u_{\theta,2} = -\text{Re} \left( \frac{d\Psi_2^s}{dr} + \frac{d\Psi_2}{dr} e^{-i2t} \right) \sin 2\theta. \quad (2.25)$$

Figure 2.3(a) is a second-order steady solution describing and clearly portraits one of the clover shape streaming cells circulating around the center of streaming cell in each quadrant. This streamline as a Eulerian solution is not a mean path of fluid particle which is a Lagrangian solution in section 2.3. Second-order oscillatory solution depicts instantaneous streamline at  $t\Omega = \pi/4$  in figure 2.3(c) and each vorticity contour is shown in figure 2.3(b) and (d) respectively.

It is interesting to note that this steady portion of the flow has an associated

vorticity field that decays algebraically with distance, in contrast to the exponential decay of the oscillatory part of the flow. Though it is difficult to show this with the solution (2.23) presented here, the matched asymptotic analysis of Schlichting[74] reveals that the mean vorticity is  $\bar{\omega}_z \sim 3\epsilon^2 r^{-2} \sin 2\theta$  as  $r \rightarrow \infty$ . This reflects the fact that the dominant steady streaming in the outer region is Stokes flow, and therefore a solution of  $\nabla^2 \bar{\omega}_z = 0$ . Vorticity of 2nd order steady solution (blue solid line) exhibits decaying in order of  $O(r^{-2})$  as matched asymptotic analysis of Schlichting (black dot line) in figure 2.4.

## 2.2 Change of Reference Frame

Ultimately, I seek the flowfield in a reference frame in which the cylinder is in oscillatory motion and the fluid is at rest at infinity, which I term the ‘inertial’ reference frame in this paper. It is important to note that a fixed position in this frame appears to be in motion in the cylinder-fixed reference frame used to obtain the solution of Holtsmark *et al.* [30]. However, it is more natural to evaluate the solution at a fixed position in this latter frame. I need to account for this discrepancy, and as I will see, this leads to both a first- and second-order correction when reconciling the two frames. It is important that I carry out this analysis, because the motion of a particle with different density from the surrounding fluid will, in general, undergo a slightly different motion relative to the cylinder in the two different scenarios.

Let us denote the position of a fixed point in the inertial reference frame by  $\mathbf{x} = (x, y)$  and the same point mapped to the cylinder-fixed reference frame by  $\boldsymbol{\xi}(t) = (\xi(t), \eta(t))$ . They are simply related by

$$\boldsymbol{\xi}(t) = \mathbf{x} - \mathbf{X}(t), \quad (2.26)$$

where here, in dimensionless form,  $\mathbf{X}(t) = \mathbf{e}_x \epsilon \sin t$ . It is straightforward to show that, in a non-inertial frame in purely translational motion, the Navier–Stokes

equations are unmodified (except for an addition to the pressure field) [58]. The streamfunction, when evaluated at  $\boldsymbol{\xi}(t)$ , is related to its counterpart in the inertial reference frame (denoted by  $\tilde{\psi}$ ) by

$$\psi(\boldsymbol{\xi}(t), t) = \tilde{\psi}(\boldsymbol{x}, t) - \left( \frac{d}{dt} \boldsymbol{X}(t) \times \boldsymbol{x} \right) \cdot \boldsymbol{e}_z = \tilde{\psi}(\boldsymbol{x}, t) - \epsilon y \cos t \quad (2.27)$$

Equation (2.27) can be used directly to transform the solution of Holtsmark *et al.* [30] to the inertial reference frame. However, it is enlightening to consider the effect of this change of frame in the context of the asymptotic expansion. Because the oscillations are assumed to be small, the streamfunction in the cylinder-fixed frame – when evaluated sufficiently far from the cylinder so that the modulated point remains outside the perimeter – can be expanded about the mean position,  $\bar{\boldsymbol{\xi}}$ , of the moving evaluation point,

$$\psi(\boldsymbol{\xi}(t), t) = \psi(\bar{\boldsymbol{\xi}}, t) + (\boldsymbol{\xi}(t) - \bar{\boldsymbol{\xi}}) \cdot \nabla \psi(\bar{\boldsymbol{\xi}}, t) + O(|\boldsymbol{\xi}(t) - \bar{\boldsymbol{\xi}}|^2). \quad (2.28)$$

However, by (2.26),  $\bar{\boldsymbol{\xi}} = \boldsymbol{x}$ . That is, the mean location of the mapped point in the cylinder-fixed frame has the same nominal coordinates as the point in the inertial frame. Thus, I simply have

$$\psi(\boldsymbol{\xi}(t), t) = \psi(\boldsymbol{x}, t) - \epsilon \sin t \frac{\partial}{\partial x} \psi(\boldsymbol{x}, t) + O(\epsilon^3). \quad (2.29)$$

(The leading order of the omitted terms reflects that these terms are linearly related to  $\psi$ , which itself has leading order  $\epsilon$ .) Thus, the relationship between streamfunction in the two frames – evaluated at the same nominal (fixed) location in each frame – can be written as

$$\tilde{\psi}(\boldsymbol{x}, t) = \psi(\boldsymbol{x}, t) + \epsilon y \cos t - \epsilon \sin t \frac{\partial}{\partial x} \psi(\boldsymbol{x}, t) + O(\epsilon^3). \quad (2.30)$$

Introducing the asymptotic expansion for  $\psi$ ,

$$\tilde{\psi}(\boldsymbol{x}, t) = \epsilon (\psi_1(\boldsymbol{x}, t) + y \cos t) + \epsilon^2 \left( \psi_2(\boldsymbol{x}, t) - \sin t \frac{\partial}{\partial x} \psi_1(\boldsymbol{x}, t) \right) + O(\epsilon^3). \quad (2.31)$$



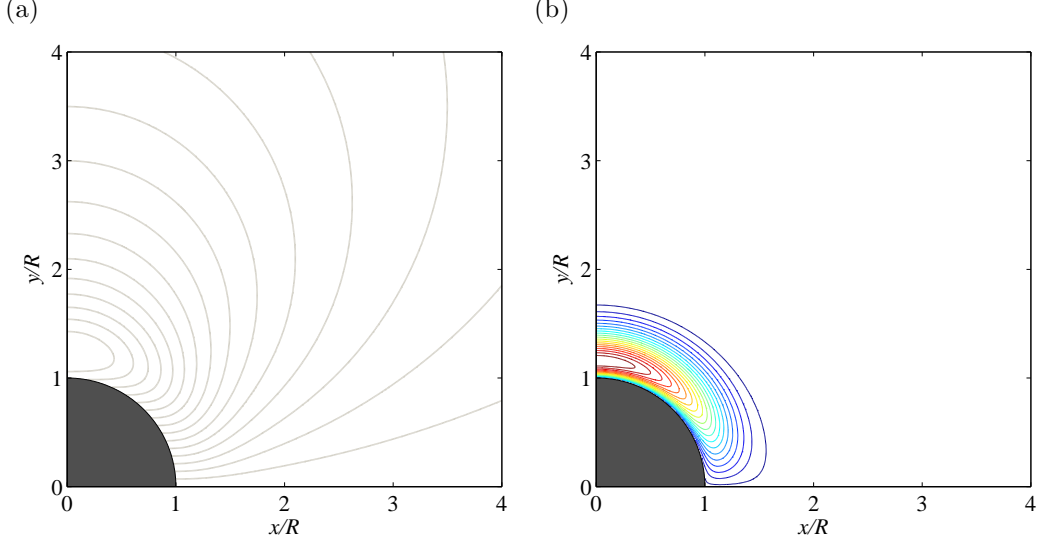


Figure 2.5: Instantaneous contour of (a) streamline (b) vorticity for First-order solution at  $t\Omega = \pi/4$  in a inertial reference frame

Thus, in order to compute the streamfunction in the inertial frame, the first-order streamfunction obtained by Holtsmark *et al.* [30] is modified by a term removing the velocity at infinity, and the second-order streamfunction is effectively corrected by the leading-order effect of the modulated field sampled by the moving evaluation point. The resulting streamfunction and velocity field for first-order solution is

$$\Psi_1^{(1)}(r) = -\frac{C}{r}, \quad (2.32)$$

$$\Psi_1^{(2)}(r) = \frac{2H_1^{(1)}(\gamma r)}{\gamma H_0^{(1)}(\gamma)} = r \left[ \frac{H_0^{(1)}(\gamma r)}{H_0^{(1)}(\gamma)} + \frac{H_2^{(1)}(\gamma r)}{H_0^{(1)}(\gamma)} \right], \quad (2.33)$$

and

$$U_{r,1}(r) = -\frac{C}{r^2} + \frac{H_0^{(1)}(\gamma r)}{H_0^{(1)}(\gamma)} + \frac{H_2^{(1)}(\gamma r)}{H_0^{(1)}(\gamma)}, \quad (2.34)$$

$$(2.35)$$

$$U_{\theta,1}(r) = -\frac{C}{r^2} - \frac{H_0^{(1)}(\gamma r)}{H_0^{(1)}(\gamma)} + \frac{H_2^{(1)}(\gamma r)}{H_0^{(1)}(\gamma)}. \quad (2.36)$$

While the first-order vorticity field in figure 2.5(b) is similar to the one without inertial reference frame modification in figure 2.2(b) first-order streamline in in-

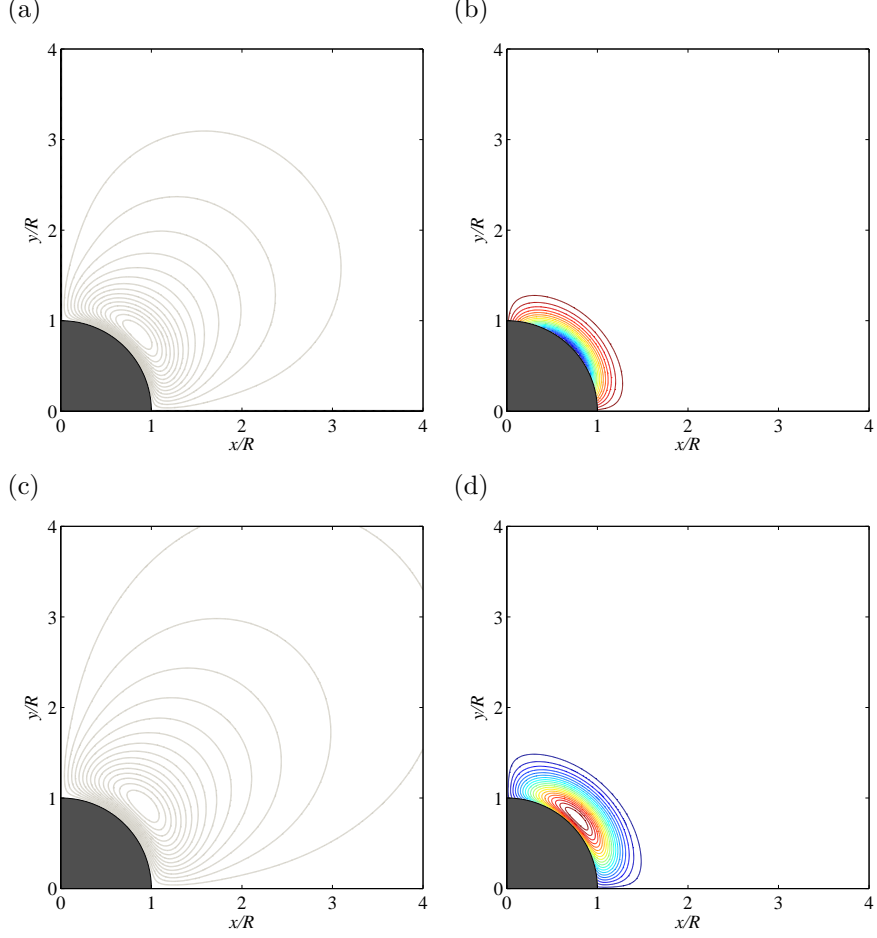


Figure 2.6: Contour of (a) streamline (b) vorticity for second-order steady solution and instantaneous contour of (c) streamline (d) vorticity for second-order oscillatory solution at  $t\Omega = \pi/4$  in inertial reference frame

ertial reference frame as shown in figure 2.5(a) is different from the one in figure 2.2(a) in that the velocity at infinity is removed.

The second-order reference frame correction in (2.31) can be expressed in a complex form similar to the expressions for  $\psi_1$  and  $\psi_2$ . We can show, using the decomposition (2.10) and rotating the  $x$ -derivative to polar coordinates, that the correction is

$$-\sin t \frac{\partial \psi_1}{\partial x} = -\text{Re} \left[ \frac{i}{4} \left( \frac{\Psi_1}{r} - \frac{d\Psi_1}{dr} \right) (1 - e^{-i2t}) \right] \sin 2\theta. \quad (2.37)$$

This correction has the same azimuthal dependence as the second-order stream-

function (2.21), and contributes both a mean and an oscillatory part (at twice the forcing frequency). In other words, the corrected form of the second-order streamfunction in the inertial reference frame can be obtained by making the replacements

$$\Psi_2^s \rightarrow \Psi_2^s - \frac{i}{4} (U_{r,1} + U_{\theta,1}), \quad \Psi_2 \rightarrow \Psi_2 + \frac{i}{4} (U_{r,1} + U_{\theta,1}). \quad (2.38)$$

The second-order velocity components are correspondingly corrected. Figure 2.6 represent second-order oscillatory solutions in inertial reference frame for (a) steady streamline, (b) steady vorticity, (c) oscillatory streamline and (d) oscillatory vorticity at  $t\Omega = \pi/4$ .

### 2.3 Lagrangian and Eulerian System

The steady portion of the streamfunction solved for in the previous section represents the mean Eulerian streamlines of the flow, as depicted in Figure 2.3(a). Fluid particles do not follow these streamlines in the mean, however. The velocity  $\mathbf{U}$  of a fluid particle can be expressed in terms of the fluid velocity as

$$\mathbf{U}(t) = \mathbf{u}(\mathbf{x}_0 + \int_0^t \mathbf{U} d\tau, t) \quad (2.39)$$

where  $\mathbf{x}_0$  is the location of the fluid particle at  $t = 0$ . Over one cycle, the excursion of the fluid particle from  $\mathbf{x}_0$  is small, and it is therefore possible to expand about this point:

$$\mathbf{U}(t) \approx \mathbf{u}(\mathbf{x}_0, t) + \int_0^t \mathbf{U} d\tau \cdot \nabla \mathbf{u}(\mathbf{x}_0, t) \quad (2.40)$$

Then, we can one again write the asymptotic expansions in  $\epsilon$  for the fluid velocities,

$$\mathbf{u} = \epsilon \mathbf{u}_1 + \epsilon^2 \mathbf{u}_2, \quad (2.41)$$

$$\mathbf{U} = \epsilon \mathbf{U}_1 + \epsilon^2 \mathbf{U}_2, \quad (2.42)$$

and substitute them into equation (2.40) and order in powers of  $\epsilon$ . As a result, we obtain

$$\mathbf{U}_1 = \mathbf{u}_1 \quad (2.43)$$

$$\mathbf{U}_2 = \mathbf{u}_2 + \int_0^t \mathbf{u}_1 \, d\tau \cdot \nabla \mathbf{u}_1 \quad (2.44)$$

We define the temporal mean,  $\overline{(\cdot)}$ , in this work over one period of oscillation as

$$\overline{f}(t) = \frac{1}{T} \int_t^{t+T} f(\tau) \, d\tau. \quad (2.45)$$

Note that  $\mathbf{u}_1$ , and thus  $\mathbf{U}_1$ , has zero mean. However, the mean of (2.44) is

$$\overline{\mathbf{U}}_2 = \overline{\mathbf{u}}_2 + \overline{\int_0^t \mathbf{u}_1 \, d\tau \cdot \nabla \mathbf{u}_1}. \quad (2.46)$$

Thus, the mean second-order motion of the fluid particle (that is, the leading-order mean motion) requires a correction: the Stokes drift. One can show, using the incompressibility of  $\mathbf{u}_1$  and the relation  $\overline{g \int^t f \, d\tau} = \overline{-f \int^t g \, d\tau}$  for periodic functions  $f$  and  $g$ , that this correction can be written as

$$\overline{\int_0^t \mathbf{u}_1 \, d\tau \cdot \nabla \mathbf{u}_1} = \frac{1}{2} \nabla \times \left( \overline{\mathbf{u}_1 \times \int_0^t \mathbf{u}_1 \, d\tau} \right). \quad (2.47)$$

Thus, the correction to streamfunction is readily available, and one can define the Lagrangian streamfunction – which defines the mean integral curves of fluid particles – as

$$\psi^L = \psi_2^s + \frac{1}{2} \left( \overline{\mathbf{u}_1 \times \int_0^t \mathbf{u}_1 \, d\tau} \right) \cdot \mathbf{e}_z. \quad (2.48)$$

This streamfunction has the same  $\theta$  dependence as  $\psi_2^s$ . After the reference frame transformation in Section 2.2 is made to the first and second order velocities, the radial dependence of the Lagrangian stream function can be expressed as

$$\Psi^L(r) = \Psi_2^s(r) + \frac{1}{2} \text{Im} \left[ -\frac{C}{r^2} + \frac{H_2^{(1)}(\gamma r)}{H_0^{(1)}(\gamma)} \right] + \frac{1}{2} \text{Im} \left[ \left( \frac{C}{r^2} - \frac{H_2^{(1)}(\gamma r)}{H_0^{(1)}(\gamma)} \right) \left( \frac{H_0^{(1)}(\gamma r)}{H_0^{(1)}(\gamma)} \right)^* \right]. \quad (2.49)$$

The third term of equation (2.49) represents the Stokes drift, the difference between mean Eulerian streamlines and Lagrangian (fluid particle) streaming. The

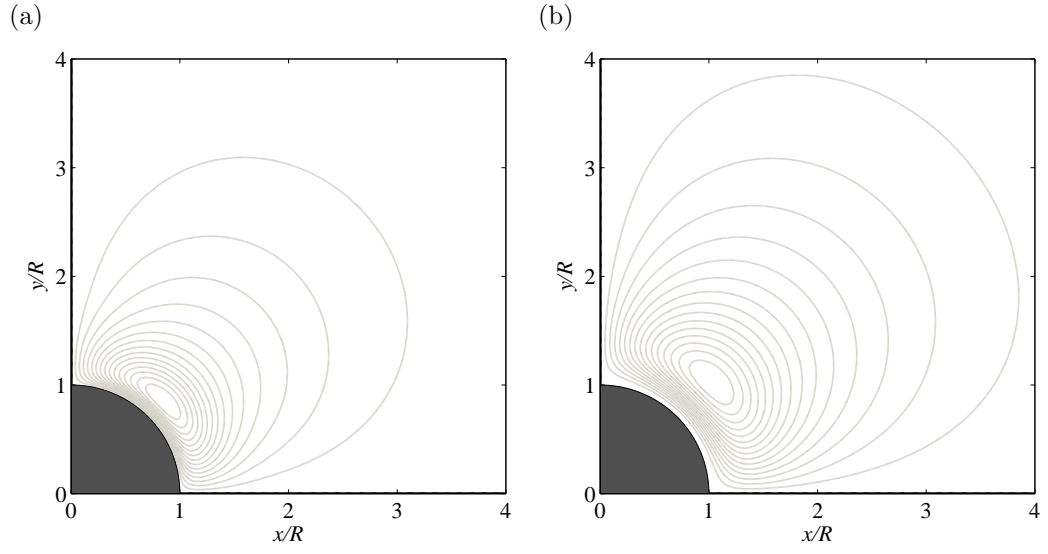


Figure 2.7: (a) Mean Eulerian streamlines and (b) mean Lagrangian streamline for  $Re = 40$ .

Lagrangian stream function is exhibited in Figure 2.7(b), which reveals the fluid particle's trajectory.

## CHAPTER 3

### Methodology

To manipulate a inertial particle the viscous streaming flow is first need to obtained and then using this flow field the motion of inertial particle is considered by integrating Maxey-Riely equation (MR equation) with Saffman lift force and wall effect. In chap 2, the streaming flow is analytically obtained for single cylinder in inertial reference frame. However it is mathematically difficult to solve flow field generated by multiple oscillating cylinder with analytical approach and this mathematical difficulty increases as the number of cylinders increases. Therefore it is natural and proper choice to seek a computational method to obtain a flow field created by multiple oscillating cylinders in various arrangement.

Viscous vortex particle method (VVPM) is a grid-free method which solves a Lagrangian form of Navier-Stokes equations using a vorticity-carrying particle as a computational elements. The crucial feature that sets the VVPM apart from a traditional grid-based method are that vorticity particles are convected with the flow and are only present where vorticity is nonzero. For instance, the vorticity is generated at the boundary and remains within the flow adjacent to the solid boundary. Thus the vortex method gains a natural efficiency. There are another significant features that give this vortex method a distinct advantage for streaming problems over traditional grid-based method. First, the velocity of any point including computational element in the flow is ‘induced’ from vortex particles through the Bio-Savart integral. For this reason, there is no need for artificial boundary conditions that is arisen when an infinite region is represented

with a grid. Second, the outer streaming motion can be largely ignored in simulation since the outer region is nearly vorticity-free [69]. Rather, the simulation focuses on the thin Stokes layer surrounding each body and the streaming motion is then computed during post-processing, which results in a much cheaper decoupled simulation. Third, no additional challenges such as grid re-generation are presented by multiple bodies that are moving and deforming since the vorticity particle moves with bodies. Last, Because the efficiency of velocity computation from vorticity particles does not rely on the distance between particles, the flow for two widely-separated bodies is computed as efficient as two nearby bodies. In fact, with the help of an acceleration technique such as fast multipole method, distant bodies are simulated faster than close probes because their mutual interaction is weaker. Grid-based methods, in contrast, need a much larger grid when bodies are located farther apart. Therefore, the VVPM will be adapted in this study due to its accuracy as well as its efficiency.

Although VVPM has a noticeable advantage for streaming problems VVPM has also a intrinsic limitation that is unable to keep low intensity level of vorticity particles due to computational efficiency, i.e, it needs to cut low intensity of vorticity particles in order to enhance computational efficiency. In VVPM, vorticities created on the surface of oscillating cylinder inside Stokes layer are supposed to spread out due to viscous diffusion and this vorticity diffusion should cover the other cylinders and even further region to correctly capture the outer region. However it is not computationally efficient and feasible to keep the low intensity of vorticity particles and thus some of them below certain strength need to be throw out. However this may cause a problem to artificially cut the low strength of vorticity particles and keep vorticity from diffusing outward although vorticities created on the surface of oscillating cylinder inside Stokes layer and are supposed to diffuse outward and naturally consist the outer region flow outside the Stokes layer. This forced vorticity blocking ultimately affect the overall streaming field

and leads to capture physically incorrect streaming of outer region.

As mentioned in chap 1, schlichting revealed by a matched asymptotic analysis that the streaming in outer region is dominated by Stokes flow. The governing equation of Stokes flow is a Laplace equation which can be readily solved by utilizing numerical method such as Boundary Element Method (BEM). BEM is a numerical method for solving boundary value or initial value problem formulated by boundary integral equation with fundamental solution to the problem. It discretizes the boundary into a collection of straight lines (2D problem) or planar segments (3D problem) and solves the system of linear equations to obtain the distributed singularities on the boundary. Using this singular values on the boundary it can generate approximate values of the required interior or exterior point. This method has a superior advantage of fast convergence, accurate estimation in infinite domain and efficient modeling due to dimension reduction in formulation.

Therefore, it may also be a natural and proper choice for multiple oscillating cylinder to adapt BEM to simulate streaming flow in outer region and VVPM to compute streaming flow in inner region in which moderate number of vorticity particle can correctly captures the streaming flow. After the streaming flow field is obtained for single cylinder by analytic approach by Holtsmark *et al.* [30] and for multiple cylinder by VVPM or BEM, using this flow field, the motion of inertial particle is considered by integrating MR equation assuming the inertial particle is a small rigid sphere particle and does not interact with surrounding fluid due to its finite and small size.

### 3.1 Viscous Vortex Particle Method (VVPM)

A viscous vortex particle method is a high-fidelity Navier-Stokes computational method that captures the fluid motion with vorticity-carrying computational particles. The Lagrangian form of Navier-Stokes equations are solved in fraction step



procedure. In the first-half time step, the vorticity particles exchange vorticity strength to explain particle convection and stretching and viscous diffusion as in unbounded flow. In the next-half time step, the vortex sheet is computed to cancel out the spurious slip resulting from the first-half step and is diffused into the neighbor flow so that the no-slip boundary condition is satisfied. In order to maintain spatial regularity which is crucial for accuracy and stability, the vorticity particles are redistributed through symmetric interpolation kernel every few steps.

The vortex particle method has been used and developed for last few decades for its computational advantage over the classic grid base method. Since this method solves the Lagrangian form of Navier-Stokes equation using vorticity-bearing particle as a computational element, it does not introduce aliasing errors which is a problematic issue in grid-based method. As a grid free method, vortex method has a lot of freedom in choosing body motion and body deformation. The vortex method also has a great computational efficiency over grid-based method when solving the multibody problem since the vorticity existing regions are only considered for computation regardless of their distance.

In the last few decades, researchers have developed rigid and thorough mathematical background for understanding the accuracy and stability of the method. The first historical numerical simulation with vortex method dates back to the 1930s by Rosehead [70, 71]. Since then, the vortex particle method have been developed significantly and accomplished notable achievements. Chorin designed the random-walk method by creating new vorticity particles to simulate the viscous effect [15]. Leonard [36, 37] and Rehbach [67] developed the three-dimensional computation of vortex method. Koumoutsakos *et al.* [34] developed scheme to enforce the no-slip boundary condition. A fast algorithm were established to enhance the computational speed [12, 26]. The Particle Strength Exchange (PSE) scheme was developed to accurately treat the viscous term [19]. The vortex method was

even extended to compressible flows by Eldredge *et al.* [23].

### 3.1.1 Basic Equations

The evolution of vorticity field for three-dimensional, incompressible, viscous flow is described by vorticity-velocity form of the Navier-Stokes equation

$$\frac{D\mathbf{w}}{Dt} = \mathbf{w} \cdot \nabla \mathbf{u} + \nu \nabla^2 \mathbf{w} \quad (3.1)$$

The term in left hand side is rate of change of vorticity  $\mathbf{w}$ , the first term in right hand side is vortex stretching and the last term is viscous diffusion term.  $\nu$  denotes kinematic viscosity and  $\mathbf{u}$  denotes velocity field. Since this equation is expressed in Lagrangian frame, this provide grid adaptivity and is free of numerical dissipation. For two-dimensional flow, since vorticity field is orthogonal to velocity field the stretching term disappear. As a result, the governing equation is simplified to convection-diffusion equation

$$\frac{D\mathbf{w}}{Dt} = \nu \nabla^2 \mathbf{w} \quad (3.2)$$

### 3.1.2 Vortex Method

Vortex methods simulate flow by solving a Lagrangian form of Navier-Stokes equation and using vorticity-carrying particles as computational elements. The Lagrangian form of Navier-Stokes equation is given below

$$\begin{aligned} \frac{d\mathbf{w}_p}{dt} &= \nu \nabla^2 \mathbf{w}(\mathbf{x}_p) \\ \frac{d\mathbf{x}_p}{dt} &= \mathbf{u}(\mathbf{x}_p) \end{aligned} \quad (3.3)$$

$\mathbf{x}_p$  and  $\mathbf{w}_p$  denotes the location and vorticity, respectively, carried by a fluid particle and particle velocity is  $\mathbf{u}_p$ . The velocity can be expressed as

$$\mathbf{u} = \nabla \times \boldsymbol{\psi} + \mathbf{U}_\infty \quad (3.4)$$

with the free stream  $\mathbf{U}_\infty$  and stream function  $\psi$ . By applying curl of (3.4), we obtain the poisson equation

$$\nabla^2 \psi = -\mathbf{w} \quad (3.5)$$

By solving the poisson equation, velocity field  $\mathbf{u}$  is recovered from (3.4). As a result, after solving these equations with initial and boundary conditions, flow field quantities can be obtained.

In vortex methods, vorticity particles are real fluid particles carrying vorticity contrast to Eulerian methods which use fixed grid point to compute flow field quantities. There are two ways to construct vorticity-carrying particle field. The first method is to assume singular vortex particles and the second method is regularized vortex particles. In this study, the regularized vortex particle is represented as a set of  $N$  Lagrangian vector-valued particles

$$\mathbf{w}(\mathbf{x}, t) = \sum_p^N S_p \mathbf{w}_p \zeta_\sigma(\mathbf{x} - \mathbf{x}_p) \quad (3.6)$$

$S_p$ ,  $\mathbf{w}_p$ ,  $\mathbf{x}_p$  represent the area, vorticity strength and position of particle  $\mathbf{p}$  respectively.  $\zeta_\sigma$  denotes the regularization function which is usually taken as radially symmetric Gaussian function and  $\sigma$  is a smoothing radius or cutoff length or core size.

$$\zeta_\sigma(\mathbf{x}) = \frac{1}{\sigma^2} \zeta\left(\frac{|\mathbf{x}|}{\sigma}\right) \quad (3.7)$$

where,

$$\zeta(\rho) = \frac{1}{2\pi} \exp\left(-\frac{\rho^2}{2}\right) \quad (3.8)$$

It is important to choose appropriate smoothing radius value so that the vortex particle core touch its very next particle's core and to choose appropriate regularization functions, which guarantee good representation of vorticity field [87]. In this study, the smoothing radius is chosen as a particle redistribution grid size.

It is also noted that the  $N$  Lagrangian particle representation of vorticity field (3.6) is not generally divergence free and also the stream function although the

divergence of vorticity is zero by a vector identity  $\nabla \cdot \mathbf{w} = \nabla \cdot \nabla \times \mathbf{u}$ . This can lead to vorticity intensification mechanism that is associated with a rapid stretching of Lagrangian particle, which make long-time computation difficult. However, maintaining the regularity of the particle distribution (in 3.1.6) can relieve this non-divergence problem [17].

### 3.1.3 Particle Convection and Stretching

The particle velocity or any velocity of specific point in flow field can be calculated from Biot-Savart integral. By defining  $G(\rho)$  such that

$$\nabla^2 G(\rho) = -\zeta(\rho) \quad (3.9)$$

one obtains

$$\psi(\mathbf{x}, t) = \sum_p G(\mathbf{x} - \mathbf{x}_p) \mathbf{w}_p S_p \quad (3.10)$$

Then, the velocity field is obtained as

$$\begin{aligned} \mathbf{u}(\mathbf{x}, t) &= \nabla \times \psi(\mathbf{x}, t) \\ &= \sum_p \nabla G(\mathbf{x} - \mathbf{x}_p) \times \mathbf{w}_p S_p \\ &= \sum_p \frac{q(\mathbf{x} - \mathbf{x}_p)}{|\mathbf{x} - \mathbf{x}_p|^2} (\mathbf{x} - \mathbf{x}_p) \times \mathbf{w}_p S_p \end{aligned} \quad (3.11)$$

where  $q(\rho) = \int_0^\rho \zeta(s) ds$ . It is important to note that by computing the velocity from (3.11), its correct value at infinity is automatically satisfied.

The vortex method employs  $N$  Lagrangian particle, the computation cost of velocity is approximately  $O(N^2)$ , where  $N$  is a number of particles in computation, which is very expensive in three-dimensional problem. Several researchers proposed Fast Multipole Method (FMM) which utilize clustering of particles and use expansions of the potentials around the cluster centers to compute their far-field influence onto other particles. A tree code is used to define a hierarchy of particle clusters so that the computational cost reduce to  $O(N)$  [26].

The noticeable difference between three-dimensional and two-dimensional simulation is the stretching term in governing equation. This term fundamentally affects the dynamics of flow by transferring the energy from large scale to small scale and is responsible for vorticity intensification which make long time simulation difficult [34].

#### 3.1.4 Particle Strength Exchange

The computation of viscous diffusion term is based on the technique of Particle Strength Exchange (PSE) [19]. In this algorithm, the Laplacian operator is approximated by an integral operator,

$$\nabla^2 \mathbf{w}(\mathbf{x}) \approx \frac{2}{\sigma^2} \int \eta_\sigma(\mathbf{x} - \mathbf{y}) (\mathbf{w}(\mathbf{y}) - \mathbf{w}(\mathbf{x})) d\mathbf{y} \quad (3.12)$$

For Gaussian smoothing,  $\eta_\sigma = \zeta_\sigma$ . The integral operator in (3.12) is discretized using particles. Therefore, the resulting discretized viscous diffusion term is

$$\left. \frac{d\mathbf{w}_i}{dt} \right|_{PSE} = \frac{2\nu}{\sigma^2} \sum_{j \in P_i} (S_i \mathbf{w}_j - S_j \mathbf{w}_i) \eta_\sigma(\mathbf{x}_i - \mathbf{x}_j) \quad (3.13)$$

$S_i$  is a area of particle i.  $P_i$  denotes the subset of particles close to particle i. Therefore, the strength exchange between particles are only done for the neighborhood particles. In this study,  $P_i$  consists of particles less than  $5\sigma$  from the particle  $\mathbf{x}_i$ . With this PSE scheme, the global circulation is conserved.

#### 3.1.5 Vortex Sheet and Diffusion

The algorithms described above can simulate for the unbounded viscous flow. In order to account for the existence of impenetrable solid surface for bounded viscous flow, we need more treatment. In vorticity-based method, such task is not straightforward since no-slip boundary condition expressed in terms of velocity at wall do not involve vorticity term explicitly. Physically the no-slip condition forces the fluid element to adhere to the wall surface, which may generate a net torque

to the fluid element adjacent to the wall that may convey the rotation motion to the flow. Therefore imposing a no-slip boundary condition at wall boundary is an important vorticity creation mechanism in flow.

Most of techniques to account for the no-slip conditions in vortex methods are based on Lighthill's vorticity creation mechanism who introduce the fractional step algorithm in which successively handle the inviscid and the viscous processes [41]. The first successful attempt to introduce no-slip boundary condition in vortex method was made by Chorin [15]. Cottet presented the algorithm which is extension to general geometries of Chorin's algorithm [16]. In this study, the algorithm proposed by Koumoutsakos et al. [34] was used to enforce the no-slip boundary condition.

In the first half-step, the vorticity particle move and exchange their particle strength according to unbounded flow algorithm, which produces spurious slip velocity which represents the difference between the tangential component of the Biot-Savart velocity evaluated on the body side of each panel sheet and the local body velocity on the same panel sheet. In the next half-step, the vortex sheet,  $\Delta\gamma$ , is created at wall to cancel the spurious slip velocity with a strength distribution that is determined by kinematic boundary condition in inviscid flow, i.e, no-flow through condition. By diffusing the vortex sheet into the flow near the solid body, the spurious slip is canceled so that the no-slip boundary condition is enforced.

Zhang and Eldredge presented the formulation of vortex sheet strength identification for deforming bodies [32]. This work is different from previous researches [22, 34, 61] in that they used volume integral over the interior of the body. The body surface is discretized by  $M$  triangular panels whose strength is uniform over the panel. The vortex sheet,  $\Delta\gamma$ , is calculated from boundary integral equation

as in vortex panel method of aerodynamics.

$$\begin{aligned} & \frac{1}{2} \Delta \boldsymbol{\gamma}(\mathbf{x}_s) - \mathbf{n} \times \int_{S_b} \nabla G(\mathbf{x}_s, \mathbf{x}') \times \Delta \boldsymbol{\gamma}(\mathbf{x}') dS(\mathbf{x}') \\ &= \left( \frac{1}{2} \mathbf{u}_b(\mathbf{x}_s) - \mathbf{u}_s(\mathbf{x}_s) - \int_{V_f} \nabla G(\mathbf{x}_s, \mathbf{x}') \times \mathbf{w}(\mathbf{x}') dV(\mathbf{x}') \right) \times \mathbf{n} \end{aligned} \quad (3.14)$$

where,

$$\begin{aligned} & \mathbf{u}_s(\mathbf{x}) \\ &= \int_{S_b} \left[ \nabla G(\mathbf{x}, \mathbf{x}') \times (\mathbf{n}' \times \mathbf{u}_b(\mathbf{x}')) - \nabla G(\mathbf{x}, \mathbf{x}') (\mathbf{n}' \cdot \mathbf{u}_b(\mathbf{x}')) \right] dS(\mathbf{x}') \end{aligned} \quad (3.15)$$

$\mathbf{u}_b$  denotes the local velocity of the deforming surface. The right hand side of (3.14) represent the spurious slip originated from the first half-step, the unbounded flow solution. It was shown that the total vorticity in the infinite unlimited space occupied by fluid and solid body is always zero [5, 88].

$$\int_{V_f} \mathbf{w}_f^{n+1} dV + \int_{V_b} \mathbf{w}_b^{n+1} dV = 0 \quad (3.16)$$

$\mathbf{w}_f$ ,  $\mathbf{w}_b$  denote the vorticity in the fluid region  $V_f$  and body region  $V_b$  respectively. By applying the relation  $\int_{V_b} \mathbf{w}_b dV = \int_{S_b} \mathbf{n} \times \mathbf{u}_b dS$  and considering the vorticity leakage,  $\mathbf{w}_f^{leak}$ , from fluid into body region during particle redistribution, we obtain following constraint for linear system of vortex sheet.

$$\int_{S_b} \Delta \boldsymbol{\gamma} dS = - \int_{V_b} \mathbf{n} \times \mathbf{u}_b^{n+1} dV + \int_{V_b} \mathbf{n} \times \mathbf{u}_b^n dV + \int_{V_f} \mathbf{w}_f^{leak} dV \quad (3.17)$$

The vortex sheet is then obtained by iteratively solving (3.14) with a constraint (3.17) in a form of Lagrangian Multiplier through a Generalized Minimal Residual Algorithm (GMRES) that has the property of minimizing the norm of residual vector at every step [72].

By diffusing the vortex sheet, the spurious slip velocity is removed so that the no-slip boundary condition is enforced. The strength of vortex sheet to be fluxed into neighboring flow is diffused with Neumann boundary condition [34].

$$-\nu \frac{\partial \mathbf{w}}{\partial \mathbf{n}} = \frac{\Delta \boldsymbol{\gamma}}{\Delta t} \quad (3.18)$$

with  $\mathbf{n}$  is pointing toward the fluid and  $\Delta t$  is the vortex sheet emitting time increment equal to time increment for advancing time step. In effect, the vortex sheet  $\Delta\gamma$  must be distributed to neighbor particles by discretizing the Green's integral for the inhomogeneous Neumann problem corresponding the diffusion equation (3.18). Leonard *et al.* [38], Ploumhans and Winckelmans [61] have proposed a more accurate panel diffusion scheme. Ploumhans and Winckelmans have extended this scheme to three-dimensional [63].

The uniform strength  $\Delta\gamma$  of a straight panel of size  $b$  is diffused into its neighbor particles. The amount of “vorticity  $\times$  area” received by particle located at  $(x_i, y_i)$  from panel is given by

$$\Delta\alpha_i = \int_0^{\Delta t} \frac{d\alpha_i}{dt} dt \quad (3.19)$$

where,

$$\frac{d\alpha_i}{dt} = \int_{x_i-h_i/2}^{x_i+h_i/2} \int_{y_i-h_i/2}^{y_i+h_i/2} \frac{d\mathbf{w}_i}{dt} dx dy \quad (3.20)$$

(3.20) is integrated exactly, giving

$$\begin{aligned} \frac{d\alpha_i}{dt} = & \frac{\Delta\gamma}{\Delta t} \left( [\text{erfc}(u)]_{(x_i-h_i/2)/\sqrt{4\nu t}}^{(x_i+h_i/2)/\sqrt{4\nu t}} \right) \\ & \times \left( \sqrt{4\nu t} \frac{1}{2} [\text{ierfc}(u)]_{(y_i-b/2-h_i/2)/\sqrt{4\nu t}}^{(y_i-b/2-h_i/2)/\sqrt{4\nu t}} - [\text{ierfc}(u)]_{(y_i+b/2-h_i/2)/\sqrt{4\nu t}}^{(y_i+b/2-h_i/2)/\sqrt{4\nu t}} \right) \end{aligned} \quad (3.21)$$

This scheme is conservative if particles are on a regular lattice aligned with the panel. However the spatial distribution of particles is not well aligned with panel. In order to make the scheme conservative the correction is added [62].

### 3.1.6 Particle Redistribution

The essential feature of vortex methods is a “good communication” between particles which stems from overlapping of particle core. If particles do not overlap with their neighbor particles, they are not able to diffuse their vorticity. In the case of excessive overlapping, the local Reynolds number diminishes, which can



lead to numerical instabilities [17]. The overlapping of particle core is a required criterion for the convergence of the vortex method [6, 28]. However, the flow map often contain local stagnation points that will cause the particles to cluster or others to spread, which prevent the particles from good communicating and thus eventually degrade the long-term accuracy and stability.

In order to maintain regularity of particle distribution, we reinitialize the particle strength onto a grid every few time steps by interpolating the strength of old particles onto a Cartesian grid and regenerating new particles from the grid whose strength is greater than some tolerance. The circulation leakage into the solid body was accounted in vortex sheet identification and diffusion so that the Kelvin's circulation theorem remains enforce. With this remeshing procedure, the distorted particle distribution is corrected so that the uniform particle distribution is maintained.

In this study the interpolation is carried out by  $M'_4$  interpolation kernel developed by Monaghan [52]. Specifically, the  $i^{th}$  old vortex with circulation  $\alpha_i$  and location  $(x_i, y_i)$  contributes circulation  $\widetilde{\alpha}_i$  to new mesh point  $(\widetilde{x}_i, \widetilde{y}_i)$  according to

$$\widetilde{\alpha}_i = \alpha_i \Lambda\left(\frac{\widetilde{x}_j - x_i}{h_i}\right) \Lambda\left(\frac{\widetilde{y}_j - y_i}{h_i}\right), \quad (3.22)$$

and

$$\Lambda(u) = M'_4(u) = \begin{cases} 0, & \text{if } |u| > 2; \\ \frac{1}{2}(2 - |u|)^2(1 + |u|), & \text{if } 1 \leq |u| \leq 2; \\ 1 - \frac{5u^2}{2} + \frac{3|u|^3}{2}, & \text{if } 0 \leq |u| < 1. \end{cases} \quad (3.23)$$

In above formula,  $u = (\widetilde{x}_j - x_i)/h_i$ , or  $u = (\widetilde{y}_j - y_i)/h_i$ .

### 3.2 Boundary Element Method (BEM)

The outer region of streaming flow is governed by Stokes flow, which is governed by biharmonic equation

$$\nabla^4 \psi = 0 \quad (3.24)$$

In order to solve the biharmonic equation for the stream function  $\psi$  and vorticity  $\phi$  in a domain  $\Omega$  surrounded by boundary  $\partial\Omega$  this biharmonic equation is split into coupled form [25]

$$\nabla^2 \psi = \phi \quad (3.25)$$

$$\nabla^2 \phi = 0, \quad (3.26)$$

where  $\phi$  is the fluid vorticity. The boundary integral form of equation (3.25) and (3.26) at the general field point  $p$  is readily derived by applying Green's Theorem and fundamental solution  $G$  [33], giving

$$\begin{aligned} \eta(p)\psi(p) = & \int_{\partial\Omega} \left\{ \psi(q) \log' |p - q| - \psi'(q) \log |p - q| \right\} d\omega(q) \\ & + \frac{1}{4} \int_{\partial\Omega} \left\{ \phi(q) G'(p, q) - \phi'(q) G(p, q) \right\} d\omega(q), \end{aligned} \quad (3.27)$$

$$\eta(p)\phi(p) = \int_{\partial\Omega} \left\{ \phi(q) \log' |p, q| - \phi'(q) \log |p - q| \right\} d\omega(q), \quad (3.28)$$

where  $p \in \Omega + \partial\Omega$ ,  $q \in \partial\Omega$  and  $d\omega(q)$  denotes the differential increment of  $\partial\Omega$  at  $q$ . The primes denotes differentiation with respect to the outward normal to  $\partial\Omega$  at  $q$ . The fundamental solution  $G$  is given by

$$G(p, q) = |p - q|^2 \{ \log |p - q| - 1 \} \quad (3.29)$$

and coefficient  $\eta(p)$  is defined with respect to the position of  $p$

$$\begin{aligned} \eta(p) = & 0 \quad \text{if } p \notin \Omega + \partial\Omega \\ = & \theta \quad \text{if } p \in \partial\Omega \\ = & 2\pi \quad \text{if } p \in \Omega \end{aligned} \quad (3.30)$$

where  $\theta$  denotes internal angle included between the tangents to  $\partial\Omega$  on either side of  $p$  if  $p \in \partial\Omega$  [33]. Integral equation (3.27) and (3.28) are numerically approximated by discretizing the boundary  $\partial\Omega$  into  $N$  smooth straight-line segment  $\partial\Omega_j$ ,  $j = 1, \dots, N$  with midpoint of segment,  $q_j$ ,  $j = 1, \dots, N$ . The unknown values of  $\psi$ ,  $\psi'$ ,  $\phi$  and  $\phi'$  on the boundary  $\partial\Omega$  is approximated as piecewise constant values  $\psi_j$ ,  $\psi_j'$ ,  $\phi_j$  and  $\phi_j'$  on each boundary segment  $\partial\Omega_j$ . The resulting discretized approximation of equation (3.27) and (3.28) at the midpoint  $p \equiv q_i$ ,  $i = 1, \dots, N$ , of each segments are given,

$$\begin{aligned} \eta_i \psi(q_i) = & \sum_{j=1}^N \left[ \psi_j \int_{\partial\Omega_j} \log' |q_i - q| d\omega(q) - \psi_j' \int_{\partial\Omega_j} \log |q_i - q| d\omega(q) \right. \\ & \left. + \frac{1}{4} \phi_j \int_{\partial\Omega_j} G'(q_i, q) d\omega(q) - \frac{1}{4} \phi_j' \int_{\partial\Omega_j} G(q_i, q) d\omega(q) \right], \end{aligned} \quad (3.31)$$

$$\eta_i \phi(q_i) = \sum_{j=1}^N \left[ \phi_j \int_{\partial\Omega_j} \log' |q_i - q| d\omega(q) - \phi_j' \int_{\partial\Omega_j} \log |q_i - q| d\omega(q) \right] \quad (3.32)$$

where  $q_i \in \partial\Omega$  and  $q \in \partial\Omega$ . Then equation (3.31) and (3.32) are now reduced to coupled system of linear equations of  $\psi$ ,  $\psi'$ ,  $\phi$  and  $\phi'$  by introducing coefficient matrix  $A, B, C$  and  $D$  [33].

$$A\psi + B\psi' + C\phi + D\phi' = 0 \quad (3.33)$$

$$A\phi + B\phi' = 0, \quad (3.34)$$

where,

$$A_{ij} = \int_{q \in \partial\Omega_j} \log' |q_i - q| d\omega(q) - \eta_j \delta_{ij} \quad (3.35)$$

$$B_{ij} = - \int_{q \in \partial\Omega_j} \log |q_i - q| d\omega(q) \quad (3.36)$$

$$C_{ij} = \frac{1}{4} \int_{q \in \partial\Omega_j} \left\{ |q_i - q|^2 \log |q_i - q| - |q_i - q|^2 \right\}' d\omega(q) \quad (3.37)$$

$$D_{ij} = - \frac{1}{4} \int_{q \in \partial\Omega_j} \left\{ |q_i - q|^2 \log |q_i - q| - |q_i - q|^2 \right\} d\omega(q) \quad (3.38)$$

In order to solve this system of linear equations (3.31) and (3.32), the coefficient matrix on each segment  $\partial\Omega_j$  need to be calculated. The evaluation using gaussian

quadrature could introduce errors, and become computationally expensive when the evaluation point  $q_i$  is located near the neighborhood of boundary  $\partial\Omega$  [33]. Thus I adapted analytical evaluation of coefficient matrix (3.35), (3.36), (3.37) and (3.38) by Kelmanson [33] presented in appendix A.

Since this problem is biharmonic any two equivalent boundary condition is needed on boundary segment  $\partial\Omega_j$ . Then using this boundary conditions the coupled system of linear equation (3.33) and (3.34) can readily solved with analytical solution of coefficient matrix from appendix A by employing direct matrix inversion scheme such as Gaussian elimination with pivoting. Direct matrix inversion scheme is favored over iterative scheme since the coefficient matrix are dense [33].

At this point boundary values of  $\psi_j$ ,  $\psi_j'$ ,  $\phi_j$  and  $\phi_j'$  on each boundary segment  $\partial\Omega_j$ ,  $j = 1, \dots, N$ , are known. Therefore substituting these values into discrete version of equation (3.27) and (3.28) can readily produce fluid stream function  $\psi$  and vorticity  $\phi$  at general point  $p \in \Omega + \partial\Omega$

### 3.3 Validation of VVPM and BEM

It is necessary to validate the viscous streaming fields obtained from either VVPM or BEM by comparing its velocity with analytical solution obtained from chapter 2. For this comparison, single cylinder undergoing rectilinear sinusoidal oscillation with amplitude  $A/R = 0.1$  and Reynolds number  $Re = 40$  is considered. Figure 3.1 (a) is a velocity history of analytical solution and VVPM simulations at  $(\sqrt{2}R, \sqrt{2}R)$  and indicates that VVPM simulation captures accurately the oscillatory flows. Since streaming flow is steady second order interactions of primary oscillatory flow it is necessary to average the velocity over one cycle to obtain second order steady solution. Figure 3.1 (b) denotes that the second order steady flow of VVPM simulations agrees well with the analytical solution and thus VVPM simulations captures well the streaming motion. The accuracy of VVPM

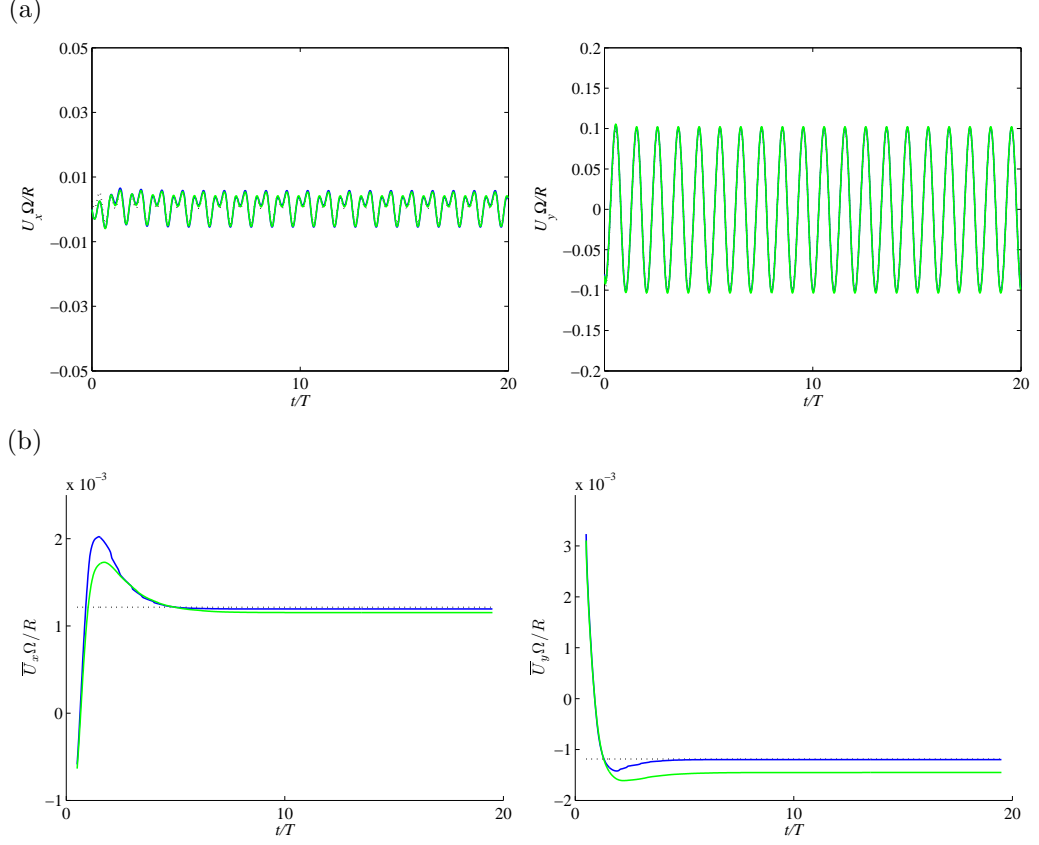


Figure 3.1: Velocity history (a) and time averaged velocity history (b) of VVPM for  $A/R = 0.1$  and  $Re = 40$  at  $(\sqrt{2}R, \sqrt{2}R)$  during  $t/T \in [0, 20]$ . Black dashed line denotes the Holtsmark's analytical solution. Blue and green indicates the VVPM simulation for  $dx = 0.01$  and  $dx = 0.02$ , respectively.

simulations increases as resolution increases.

In addition to this velocity comparison, it is also necessary to investigate steady Eulerian streamline to identify the streaming motion. For this validation, single cylinder undergoing rectilinear sinusoidal oscillation with amplitude  $A/R = 0.04$  and Reynolds number  $Re = 49$  is considered. In VVPM, the circulation of computational element, vorticity times area of computational element, is used for strength of computational element. Thus this circulation has minimum value (tolerance) to be kept during computation and some vorticity particles as computational elements below this tolerance need to be thrown out in order to reduce the

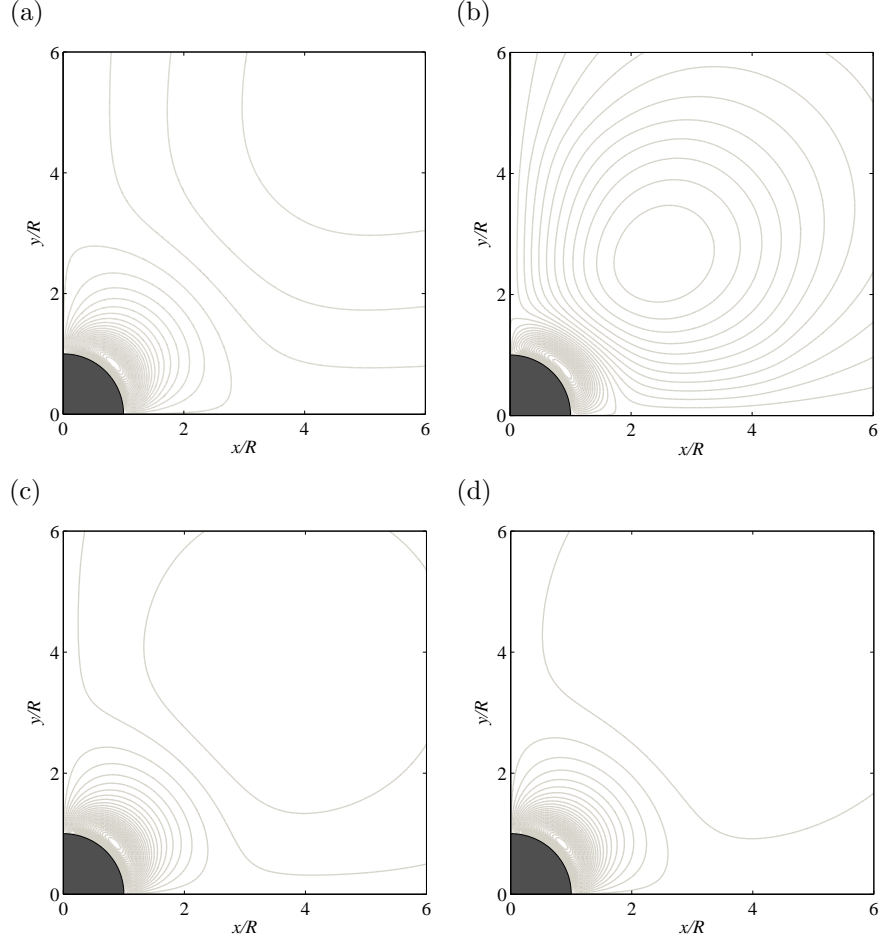


Figure 3.2: Contour of steady Eulerian streamlines from (a) analytical solution and VVPM of (b)  $dx = 0.02$ ,  $tol = 10^{-7}$ ,  $\omega_{tol} = 2.5 \times 10^{-4}$ , (c)  $dx = 0.01$ ,  $tol = 10^{-9}$ ,  $\omega_{tol} = 1.0 \times 10^{-5}$ , (d)  $dx = 0.01$ ,  $tol = 10^{-10}$ ,  $\omega_{tol} = 1.0 \times 10^{-6}$

number of computational element and increase the computation efficiency. In this simulation, the area of computational element is square of grid size of remeshing step. Therefore different simulation result could be obtained by varying grid size since it affects the tolerance and thus vorticity field. Several different simulations for  $Re = 49$  with varying grid size and tolerance from VVPM, which ultimately affects the minimum vorticity ( $\omega_{tol}$ ), are compared with analytical solution.

In figure 3.2(a), steady Eulerian streamline depicts one of four quadrants with inner streaming cell circulating clock-wise and non-closed form of outer streaming

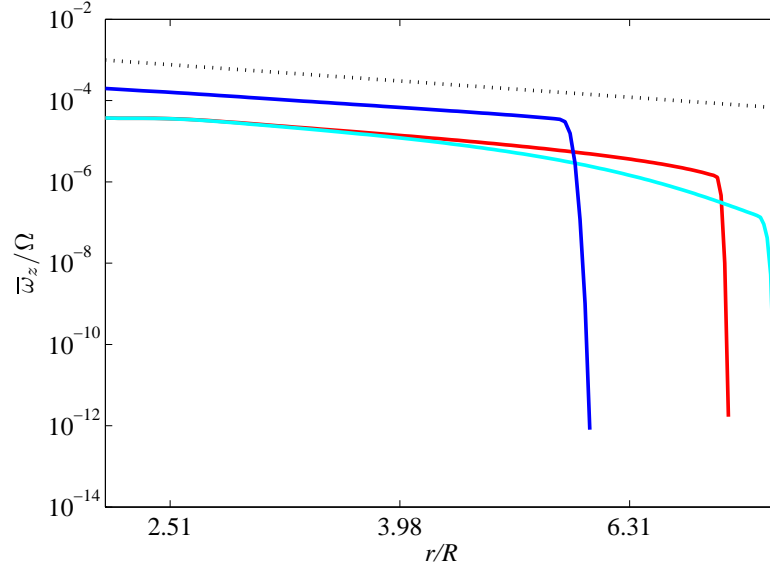


Figure 3.3: Mean vorticity along 45 degree line from matched asymptotic analysis of Schlichting (black dot) and VVP M of  $dx = 0.02$ ,  $tol = 10^{-7}$ ,  $\omega_{tol} = 2.5 \times 10^{-4}$  (blue),  $dx = 0.01$ ,  $tol = 10^{-9}$ ,  $\omega_{tol} = 1.0 \times 10^{-5}$  (red) and  $dx = 0.01$ ,  $tol = 10^{-10}$ ,  $\omega_{tol} = 1.0 \times 10^{-6}$  (cyan). Matched asymptotic analysis and initial portion of VVP M simulations indicate decaying in order of  $O(r^{-2})$ .

region in which flows are directed from positive y-axis to positive x-direction. The dividing streaming line between inner and outer streaming region,  $\delta_{DC}/R$ , is 2.9404. The rests are numerical simulations from VVP M and denote similar inner streaming cell but closed form of outer streaming region. As tolerance values are decreased, the degree of closed form in outer streaming is mitigated and dividing streaming line,  $\delta_{DC}/R$ , approaches to the one of analytical solution (  $\delta_{DC}/R = 1.6405$ (b), 2.7719(c), and 2.8850 (d) ). We can deduce that the closed form of outer streaming is originated by throwing out the vorticities below tolerance at the periphery and this throwing out caused the equivalent imaginary wall effect at the vorticity diffusion periphery. Therefore streamlines formed closed loop to satisfied no flow through condition at this equivalent imaginary wall.

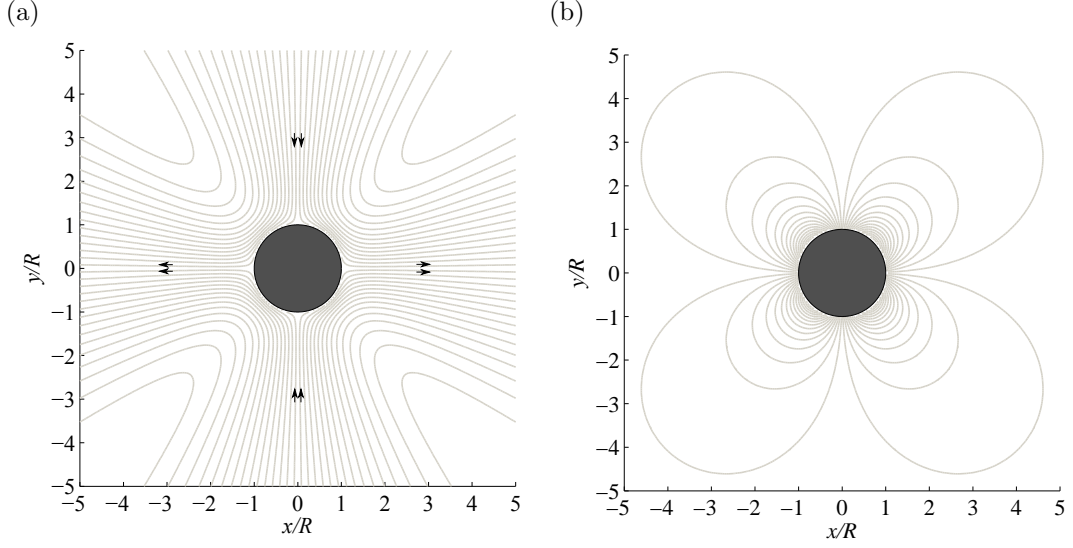


Figure 3.4: Contour of (a) streamline and (b) vorticity from Boundary Element Methods

This effect easily identified by investigating mean vorticity values, as depicted in figure 3.3, along the 45 degree lines from the origin, where vorticity is maximum. As indicated in chapter 2 matched asymptotic analysis of Schlichting (black dot line) revealed the mean vorticity decrease slowly in order of  $O(r^{-2})$ . Numerical simulations from VVPM also exhibit similar decaying behaviors except at the periphery in which weak vorticities are thrown out. This caused vorticities to build up and make equivalent imaginary wall at this periphery. As tolerance is lowered or minimum vorticity value is increased by decreasing grid size this imaginary wall effect is alleviated and dividing streamline position became closed to the one of analytical solution. However, vorticities below tolerance will be thrown out eventually and thus have a closed loop form of outer streaming. It is very expensive and inefficient to keep every level of vorticities to capture the correct behavior in outer streaming region. We can reduce this computational efforts by employing BEM to solve Stokes equation with boundary condition obtained by matching with the inner Stokes layer solution in the asymptotic expansion for small amplitude.



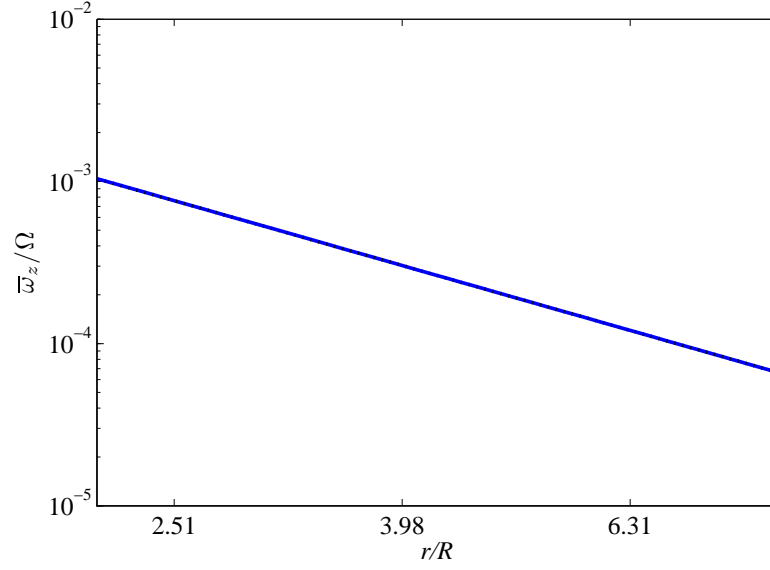


Figure 3.5: Mean vorticity along 45 degree line from matched asymptotic analysis of Schlichting (black dot) and BEM (blue).

Figure 3.4 denote contour of streamline and vorticity from BEM respectively. Streamline contour exhibit well the outer streaming region but cannot capture inner streaming cell whose thickness is decreased to zero since the matched inner Stokes layer solution is applied on boundary. This BEM solution for outer region exhibits well the predicted vorticity decaying in order of  $O(r^{-2})$  as shown in figure 3.5.

From these validation of VVPM and BEM it is shown that VVPM captures well the behavior of inner streaming cell except outer streaming region due to the cut of vorticity below tolerance, and BEM cannot explore the inner streaming cell. Therefore VVPM and BEM will be used to simulate the inertial particle transport between oscillating cylinders inside inner streaming cell, and outside inner streaming cell respectively.

### 3.4 Computation of Inertial Particle Trajectory

At this point we obtained streaming flow field for single oscillating cylinder using analytic approach by Holtsmark *et al.* [30] and for multiple oscillating cylinder by either VVPM or BEM. We are primarily interested in this work in computing the trajectory,  $\mathbf{X}_p(t)$ , of an inertial particle. These trajectories will be computed by integrating the Maxey–Riley (MR) equation with Saffman lift force [49, 81], which is based on the assumption of a rigid spherical particle with small slip Reynolds number,  $Re_p$ . We are therefore implicitly assuming that the motion of the particle does not significantly affect the flow generated by the oscillating cylinder. Use of the Saffman lift force is restricted by the condition of small slip Reynolds number ( $Re_p \ll 1$ ) and shear Reynolds number ( $Re_G \ll 1$ ), as well as  $Re_p \ll Re_G^{1/2}$ . That these conditions are satisfied in the present simulations can be demonstrated by examining a typical particle traversing the Stokes layer, where it experiences the largest slip velocity and shear. For the typical case of this study, particle size, Reynolds number and oscillation amplitude are  $a/R = 0.175$ ,  $Re = 40$  and  $\epsilon = 0.2$ , respectively. At time  $t/T = 325.5$ , when it is closest to the cylinder,  $|\mathbf{w}| = 0.0268$  and  $G = 0.695$  and thus  $Re_p = 0.184 \ll 1$ ,  $Re_G = 0.836 < 1$  and  $Re_p \ll Re_G^{1/2}$ . The Faxén correction terms cannot be ignored in our study, as their contribution is notable in the regions of significant vorticity, where the particle remains for most of its trajectory. We ignore the gravity terms, and are therefore left with

$$\begin{aligned} \frac{d\mathbf{X}_p}{dt} &= \mathbf{V}_p \\ m_p \frac{d\mathbf{V}_p}{dt} &= -6\pi\rho_f\nu a \left[ \mathbf{V}_p(t) - \mathbf{u}(\mathbf{X}_p(t), t) - \frac{1}{6}a^2\nabla^2\mathbf{u}(\mathbf{X}_p(t), t) \right] + m_f \frac{D\mathbf{u}}{Dt} \Big|_{\mathbf{X}_p(t)} \\ &\quad - \frac{1}{2}m_f \left( \frac{d\mathbf{V}_p}{dt} - \frac{D\mathbf{u}}{Dt} \Big|_{\mathbf{X}_p(t)} - \frac{d}{dt} \left[ \frac{1}{10}a^2\nabla^2\mathbf{u}(\mathbf{X}_p(t), t) \right] \right) \\ &\quad - 6\pi^{1/2}\nu^{1/2}a^2\rho_f \int_{-\infty}^t \frac{d/d\tau [\mathbf{V}_p(\tau) - \mathbf{u}(\mathbf{X}_p(\tau), \tau) - \frac{1}{6}a^2\nabla^2\mathbf{u}(\mathbf{X}_p(\tau), \tau)]}{\sqrt{t-\tau}} d\tau \\ &\quad + 4K\rho_f a^2 (\nu |G|)^{1/2} \text{sgn}(G) |\mathbf{u} - \mathbf{V}_p| \mathbf{n}, \end{aligned} \tag{3.39}$$

$$\tag{3.40}$$

where

$$G = |\mathbf{u} - \mathbf{V}_p|^{-2} \left[ (u_x - V_{p,x})^2 \frac{\partial u_x}{\partial y} - (u_y - V_{p,y})^2 \frac{\partial u_y}{\partial x} - (u_x - V_{p,x})(u_y - V_{p,y}) \left( \frac{\partial u_x}{\partial x} - \frac{\partial u_y}{\partial y} \right) \right] \quad (3.41)$$

and

$$\mathbf{n} = |\mathbf{u} - \mathbf{V}_p|^{-1} [-(u_y - V_{p,y}) \mathbf{e}_x + (u_x - V_{p,x}) \mathbf{e}_y] \quad (3.42)$$

The symbols  $m_p$  and  $m_f$  denote, respectively, the mass of the inertial particle and the displaced fluid. The vectors  $\mathbf{V}_p$  and  $\mathbf{u}$  are, respectively, the velocity of the inertial particle and the fluid velocity. The Saffman constant,  $K$ , is 1.615. It should be noted that  $G$  represents the coordinate-independent shear rate – the  $\mathbf{n}$ -directed gradient of the component of fluid velocity in the direction of relative particle motion – as used by Tio *et al.* [81]. The operators  $d/dt$  and  $D/Dt$  denote the time derivatives along their respective sets of characteristics,

$$\frac{d\mathbf{u}}{dt} = \frac{\partial \mathbf{u}}{\partial t} + \mathbf{V}_p \cdot \nabla \mathbf{u}, \quad \frac{D\mathbf{u}}{Dt} = \frac{\partial \mathbf{u}}{\partial t} + \mathbf{u} \cdot \nabla \mathbf{u}. \quad (3.43)$$

The terms on the right hand side of (3.40) represent, respectively, the viscous Stokes drag, the fluid acceleration force, the added mass, the Basset history force and the Saffman lift force. The terms involving the Laplacian of the fluid velocity are the Faxén corrections, which represent the effect of non-uniform fluid velocity incident upon the inertial particle.

The Basset history force (sometimes described as the ‘memory term’) represents the cumulative influence of the diffusion of vorticity from the particle during its total traveling history. The computation of this term is extremely time consuming and memory intensive, and many studies neglect it for simplicity. However, it may lead to a physically incorrect result to omit the history term for a non-neutrally buoyant particle. Studies by Daitche and Tél [18], Candelier, Angilella, and Souhar [10, 11] and Mordant and Pinton [53] have shown that the history

term can have a significant effect on the motion of an inertial particle and cannot generally be neglected. An efficient technique for computing the history force term was recently proposed by van Hinsberg, ten Thijs Boonkamp, and Clercx [82]. The integration interval is divided into two sub-intervals. The sub-interval involving more recent history is computed by trapezoidal integration; in the more distant sub-interval, the Basset kernel  $t^{-1/2}$  is replaced with an exponential approximant, and a recursive algorithm is constructed to minimize expense. We adopt this approach in the present work.

Since the MR equation (3.40) evaluates the terms at the center of the inertial particle, it makes sense to define the relative velocity,  $\mathbf{w} = \mathbf{V}_p - \mathbf{u}(\mathbf{X}_p)$ , so that the relationship between time derivatives is simply

$$\frac{D\mathbf{u}}{Dt} = \frac{d\mathbf{u}}{dt} - \mathbf{w} \cdot \nabla \mathbf{u}. \quad (3.44)$$

Furthermore, we can non-dimensionalize the variables using  $\Omega$  and  $R$ , as for the flowfield itself in the Appendix. Thus, the dimensionless version of the MR equation (3.40) can be written as

$$\begin{aligned} \left( \frac{\rho_p}{\rho_f} + \frac{1}{2} \right) \frac{d\mathbf{w}}{dt} = & -\frac{9}{2} Re_a^{-1} \mathbf{w} + (1 - \rho_p/\rho_f) \left. \frac{d\mathbf{u}}{dt} \right|_{\mathbf{X}_p(t)} - \frac{3}{2} \mathbf{w} \cdot \nabla \mathbf{u} \Big|_{\mathbf{X}_p(t)} \\ & - \frac{9}{2} \pi^{-1/2} Re_a^{-1/2} \int_{-\infty}^t \frac{d/d\tau [\mathbf{w} - \frac{1}{6}(a/R)^2 \nabla^2 \mathbf{u}(\mathbf{X}_p(\tau), \tau)]}{\sqrt{t - \tau}} d\tau \\ & + 3K Re_a^{-1/2} |G|^{1/2} \text{sgn}(G) |\mathbf{w}| \mathbf{n} \\ & + \frac{3}{4} Re_a^{-1} (a/R)^2 \nabla^2 \mathbf{u}(\mathbf{X}_p(t), t) + \frac{1}{20} (a/R)^2 \frac{d}{dt} [\nabla^2 \mathbf{u}(\mathbf{X}_p(t), t)]. \end{aligned} \quad (3.45)$$

where  $Re_a = \Omega a^2/\nu = Re(a/R)^2$  is a particle-based Reynolds number. In terms of the direction,  $\hat{\mathbf{w}} = \mathbf{w}/|\mathbf{w}|$ , of the relative velocity, the direction of Saffman lift is

$$\mathbf{n} = \hat{\mathbf{w}} \times \mathbf{e}_z \quad (3.46)$$

and the generalized shear rate is represented compactly as

$$G = \mathbf{n} \cdot \nabla \mathbf{u} \cdot \hat{\mathbf{w}}. \quad (3.47)$$

The inertial particle initially has the same velocity as the surrounding fluid, so that the initial condition of this integro-differential equation is  $\mathbf{w}(0) = 0$ . The Stokes drag and the Basset history act as penalty terms, tending to drive  $\mathbf{w}$  to zero when the particle’s velocity deviates from that of the fluid; these terms, along with the Saffman lift, are only active when  $\mathbf{w}$  is non-zero. The unsteady term (the second term on the right-hand side) and Faxén corrections are the only inhomogeneous terms in this equation, and we note that the first of these is absent for neutrally buoyant particles. The third term on the right-hand side, due to the differences in the advection between a fluid and inertial particle, is only significant when the particle traverses regions of steep change in fluid velocity. The equation is integrated with a 4th-order Adams-Bashforth method with time step size 0.02. At each time step, the fluid velocity, its gradient, and its time derivative are computed from the Holtsmark solution (with a correction for change of reference frame, described above) at the instantaneous location of the particle. Convergence of the time marching was tested by doubling and halving the step size, and verifying that the results were insensitive.

The relevant dimensionless parameters of this problem, in addition to the oscillatory Reynolds number  $Re$  and amplitude ratio  $\epsilon$ , are the density ratio  $\rho_p/\rho_f$  and particle size ratio  $a/R$ . In this work, we will keep  $\epsilon$  fixed between 0.1 and 0.2; this is a compromise between a sufficiently small amplitude for the asymptotic solution to hold and practical integration times for computing particle trajectories.

Finally, we note that we do not add an additional force to account for the hydrodynamic influence of the rigid cylinder on the particle here. That is, the effect of the cylinder on the particle’s motion is felt solely through the velocity field generated by the oscillating cylinder. However, the hydrodynamic influence such as lubrication force from the cylinder need to be considered when inertial particles are transported from one cylinder to other, and thus they follow the outmost streaming lines and approach close enough toward the other cylinder.

Then influence from the cylinder cannot be ignored anymore. The influence force will be treated in chapter 5.

## CHAPTER 4

### Inertial Particle Trapping

In this chapter, the inertial particle motion in streaming flow generated by single oscillating cylinder is considered. Relevant streaming flow information will be used from analytical solution in chapter 2. Particle size, oscillation amplitude and Reynolds number are set as  $a/R = 0.175$ ,  $Re = 40$  and  $\epsilon = 0.2$ , respectively for the typical parameters of this inertial particle trapping of single oscillating cylinder. In this chapter, general trapping observation will be discussed. Then I will discuss what mechanism makes the inertial particle trapped inside streaming cell. Trapping speed depending on physical parameter such as particle size, density and flow Reynolds number and inner and outer streaming behavior will be followed.

#### 4.1 Inertial Particle Trapping

The trajectory,  $\mathbf{X}_p(t)$ , of an inertial particle is computed by integrating equation (3.45) for the inertial particle velocity,  $\mathbf{V}_p$ , based on the parameters of relative particle density  $\rho_p/\rho_f$ , relative size  $a/R$  and Reynolds number  $Re$ . Figure 4.1 depicts a visual comparison of the continuous inertial particle trajectory and the trajectory sampled once per oscillation cycle, in this case for a neutrally buoyant particle. The particle oscillates at the forcing frequency with an amplitude of approximately  $0.03R$ . As expected due to the small streaming velocity of order  $\epsilon^2$ , the overall migration speed is very slow.

Figure 4.2 depicts representative trajectories for a heavy, a neutrally buoyant,

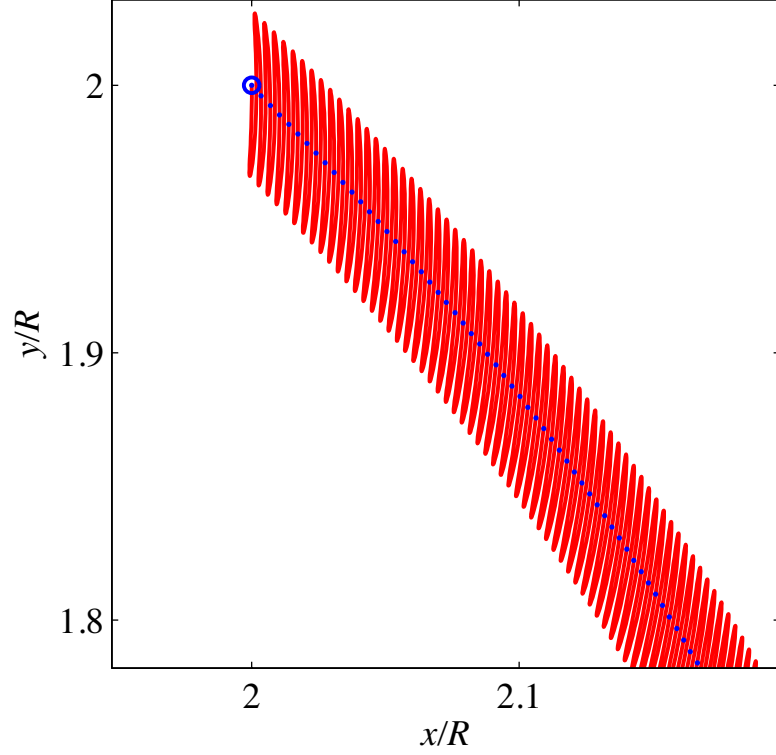


Figure 4.1: Inertial particle trajectory (in red) based on trajectory sampled once per cycle (blue dots) for  $Re = 40$ ,  $a/R = 0.175$  and  $\rho_p/\rho_f = 1$ .

and a light particle at  $Re = 40$  for a particle of radius  $a = 0.175R$ . Each trajectory is sampled only once per cycle for clarity purposes, and thus is actually a set of discrete points representing the Poincaré section of the particle motion. Open blue circles denote the initial location, in this case at  $(x, y) = (2R, 2R)$ , and the mean Lagrangian streamlines are depicted for reference. Note that, at this Reynolds number, the inner streaming cell has size  $\delta_{DC} \approx 4.6R$ .

The plots in Figure 4.2 indicate that particles undergo an inward spiral toward the center of the streaming cell, regardless of their density relative to the fluid. Figure 4.2(d) shows that the trajectories of an inertial particle and fluid particle starting from the same initial location deviate over one oscillation cycle, with the inertial particle ultimately closer to the center of the streaming cell at the end



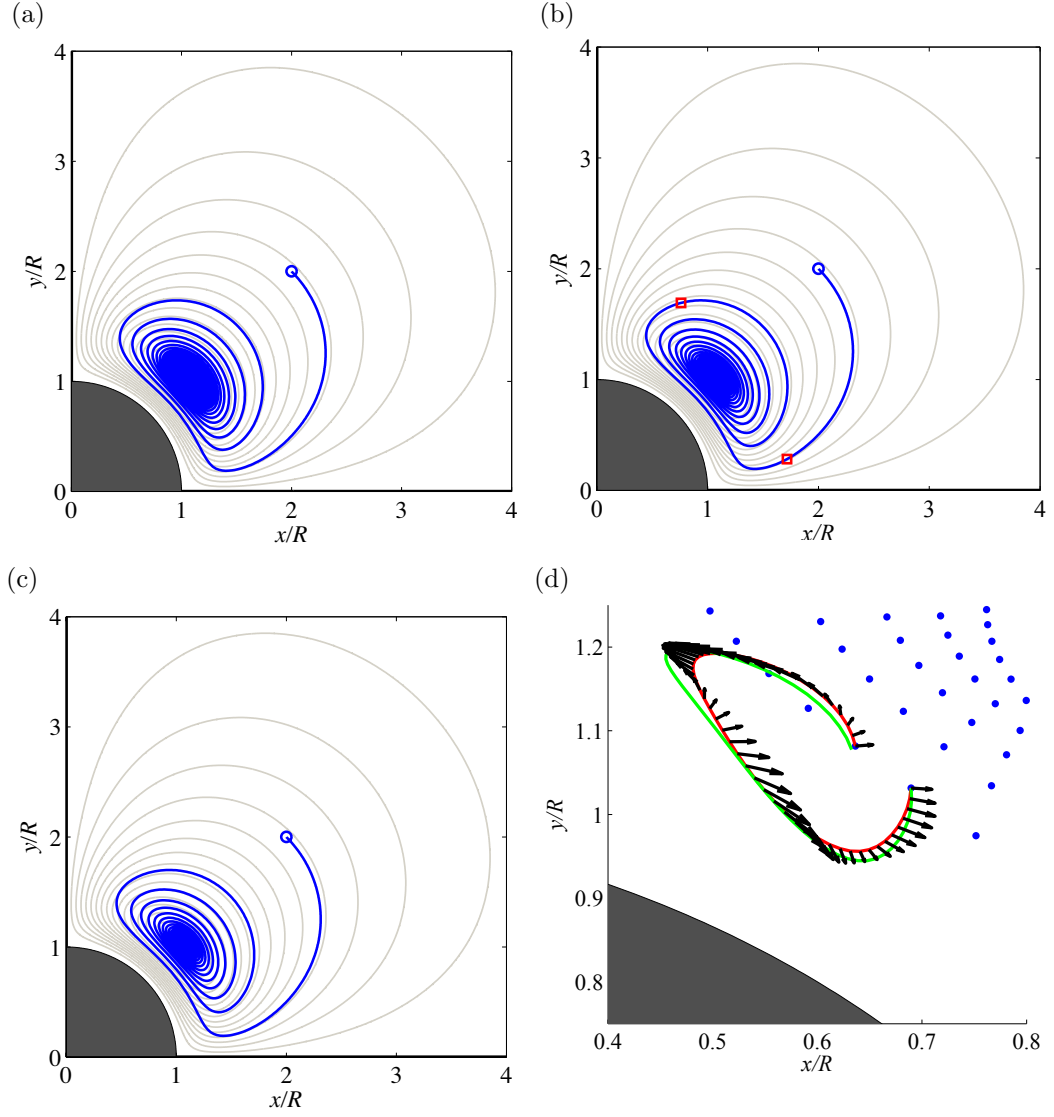


Figure 4.2: Inertial particles trajectories (in blue), sampled once per cycle, for  $Re = 40$ ,  $a/R = 0.175$ . Initial locations depicted with blue circles. (a)  $\rho_p/\rho_f = 1.05$ , (b) 1, (c) 0.95. In (b), red squares denote the instants  $t/T = 290$  and 350. Lagrangian streamlines are depicted in light gray. (d) Inertial (red) and fluid (green) particle trajectories over one oscillation cycle,  $t/T \in [317, 318]$  for  $\rho_p/\rho_f = 1$ . Black arrows depict the total hydrodynamic force vectors in equation (3.45). Blue dots denote inertial particle trajectory sampled once per cycle.

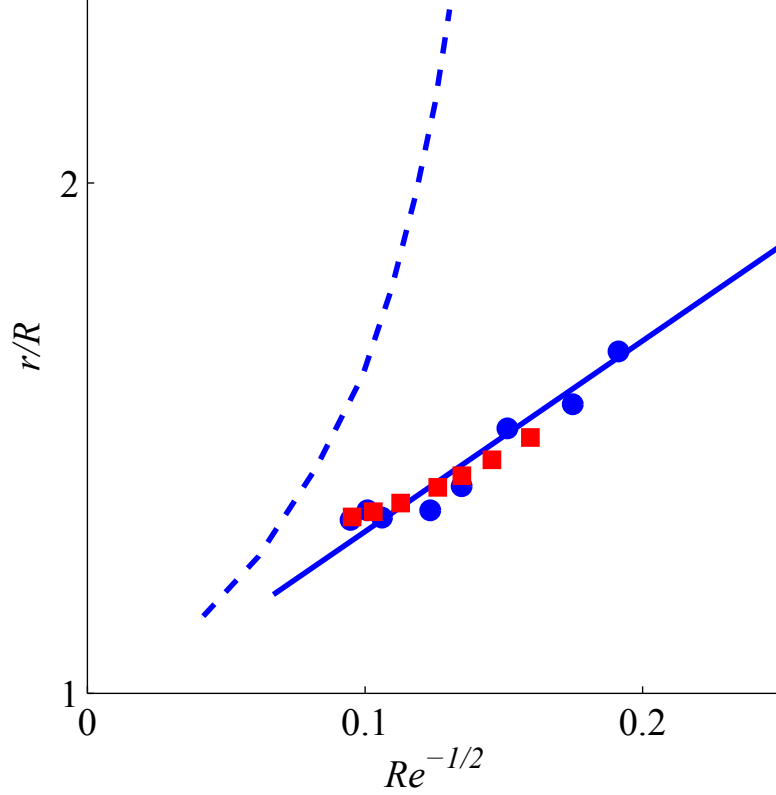


Figure 4.3: Comparison of trapping position from current results (red squares) and experiments (blue circles) of Lutz *et al.* [45]. Dashed and solid lines depict, respectively, inner streaming cell size  $\delta_{DC}/R$  and inner streaming cell center location.

of the cycle. The hydrodynamic force vectors shown here are computed from the right-hand side of (3.45), and thus are proportional to the rate of change of the relative velocity between the inertial and fluid particles. They are generally directed away from the cylinder, consistent with the deviation of the trajectories.

This spiral trajectory is qualitatively similar to the trajectory of a microsphere in a micro-channel reported in the experiments of Lutz *et al.* [45]. Figure 4.3 depicts a comparison of the final trapping position predicted in the present study with the experimental results of Lutz *et al.* [45], at different Reynolds numbers. The size  $\delta_{DC}/R$  of the inner streaming cell is also shown, and exhibits the depen-

dence on Reynolds number reported above, increasing without bound as  $Re \rightarrow 37$ . The position of trapping predicted by the model agrees well with the experiments.

## 4.2 Inertial particle Trapping Mechanism

In order to determine whether the motion of an inertial particle shows a tendency to spiral inward or outward, it is helpful to consider the instantaneous cross product of the local tangents to the mean inertial and fluid particle trajectories, which we denote as  $\alpha$ . If we assume that at some recent instant the inertial particle moved at the same velocity as the fluid, then the tangent of the mean inertial particle trajectory is approximately  $\overline{\mathbf{V}}_p/|\overline{\mathbf{U}}_0|$ , where  $\overline{\mathbf{U}}_0$  is a constant, representative of the mean fluid particle velocity,  $\overline{\mathbf{U}}$ , during a certain interval. Then, we can define

$$\alpha(t)\mathbf{e}_z = |\overline{\mathbf{U}}_0|^{-2} (\overline{\mathbf{V}}_p(t) \times \overline{\mathbf{U}}(t)). \quad (4.1)$$

By the definition (2.45) of temporal mean, it is easy to verify that these mean velocities,  $\overline{\mathbf{V}}_p$  and  $\overline{\mathbf{U}}$ , represent Poincaré maps of inertial and fluid particle position, respectively, from one period to the next, e.g.  $\mathbf{X}_p(t+T) = \mathbf{X}_p(t) + T\overline{\mathbf{V}}_p(t)$ . Since all particles undergo clockwise orbits in the streaming cell in the first quadrant, then  $\alpha > 0$  implies a tendency of the inertial particle to spiral inward,  $\alpha < 0$  a tendency to spiral outward, and  $\alpha = 0$  a tendency to stay on the mean Lagrangian streamline. Thus, the particle's motion at a given instant can be explained by examining this quantity, as Figure 4.4 illustrates. It is instructive to consider this expression at some instant  $t_0$  such that the inertial and fluid particles have been constrained to follow the same trajectory for  $t \leq t_0$ , so  $\alpha(t_0) = 0$ , and  $d\alpha/dt$  expresses the tendency for these trajectories to deviate in the next instant.

First, it is straightforward to show that the temporal mean and derivative

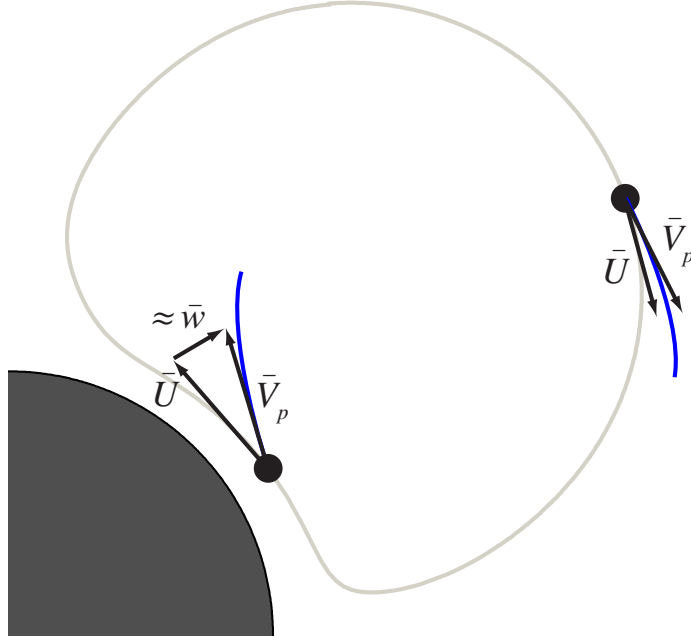


Figure 4.4: Illustration of the tendency of an inertial particle to deviate from a Lagrangian streamline. Note that  $\alpha < 0$  in the upper right portion of the streamline, and  $\alpha > 0$  in the lower left portion.

operations commute with one another. Thus, at  $t_0$ , we can write

$$\frac{d\alpha}{dt} \mathbf{e}_z = |\bar{\mathbf{U}}_0|^{-2} \left( \frac{d\bar{\mathbf{V}}_p}{dt} \times \bar{\mathbf{U}} + \bar{\mathbf{V}}_p \times \frac{d\bar{\mathbf{U}}}{dt} \right). \quad (4.2)$$

Using a Taylor expansion about a reference position similar to that used in the Appendix for the mean fluid particle velocity, it can be shown that the mean of the relative velocity is

$$\bar{\mathbf{w}}(t) = \bar{\mathbf{V}}_p(t) - \bar{\mathbf{U}}(t) - \mathbf{w}_{sd}, \quad (4.3)$$

where the final term,  $\mathbf{w}_{sd} = \overline{\int^t \mathbf{w} d\tau \cdot \nabla \mathbf{u}}$ , represents the difference in Stokes drift between the inertial and fluid particles. This term is smaller than the Stokes drift itself, and is therefore not expected to serve a role in determining the inward or outward motion of the inertial particle, so we neglect it in this discussion. Thus,

we can equally well define  $d\alpha/dt$  at  $t_0$  as

$$\frac{d\alpha}{dt}\mathbf{e}_z = |\bar{\mathbf{U}}_0|^{-2} \left( \frac{d\bar{\mathbf{w}}}{dt} \times \bar{\mathbf{U}} + \bar{\mathbf{w}} \times \frac{d\bar{\mathbf{U}}}{dt} \right). \quad (4.4)$$

In the first term, we can replace  $d\mathbf{w}/dt$  with the MR equation (3.45), and we note that the temporal mean also commutes with the convolution operator in the Basset term. Thus, we end up with

$$\begin{aligned} \frac{d\alpha}{dt}\mathbf{e}_z = & |\bar{\mathbf{U}}_0|^{-2} \left[ C_u \frac{d\bar{\mathbf{U}}}{dt} \times \bar{\mathbf{U}} - C_s \bar{\mathbf{w}} \times \bar{\mathbf{U}} - C_c \bar{\mathbf{w}} \cdot \nabla \bar{\mathbf{U}} \times \bar{\mathbf{U}} \right. \\ & - C_b \int_{-\infty}^t \frac{d/d\tau [\bar{\mathbf{w}} - \frac{1}{6}(a/R)^2 \nabla^2 \bar{\mathbf{U}}(\mathbf{X}_p(\tau), \tau)]}{\sqrt{t-\tau}} d\tau \times \bar{\mathbf{U}} \\ & + C_l \text{sgn}(G) |\bar{G}|^{1/2} |\bar{\mathbf{w}}| \bar{\mathbf{n}} \times \bar{\mathbf{U}} \\ & \left. \left( C_{f1} \nabla^2 \bar{\mathbf{U}} + C_{f2} \frac{d}{dt} \nabla^2 \bar{\mathbf{U}} \right) \times \bar{\mathbf{U}} + \bar{\mathbf{w}} \times \frac{d\bar{\mathbf{U}}}{dt} \right]. \quad (4.5) \end{aligned}$$

where

$$\begin{aligned} C_u = & \frac{1 - \rho_p/\rho_f}{\rho_p/\rho_f + 1/2}, \quad C_s = \frac{(9/2)Re_a^{-1}}{\rho_p/\rho_f + 1/2}, \quad C_c = \frac{3/2}{\rho_p/\rho_f + 1/2}, \\ C_b = & \frac{(9/2)\pi^{-1/2} Re_a^{-1/2}}{\rho_p/\rho_f + 1/2}, \quad C_l = \frac{3K Re_a^{-1/2}}{\rho_p/\rho_f + 1/2}, \\ C_{f1} = & \frac{(3/4)Re_a^{-1}(a/R)^2}{\rho_p/\rho_f + 1/2}, \quad C_{f2} = \frac{(1/20)(a/R)^2}{\rho_p/\rho_f + 1/2}. \end{aligned} \quad (4.6)$$

Here, we examine the quantities  $\alpha$  and  $d\alpha/dt$  during the interval between  $t/T = 290$  and  $350$  (between two red squares in Figure 4.2(b)), when the inertial particle experiences the greatest tendency toward the center of the streaming cell. As Figure 4.5(a) shows, the value of  $\alpha$  remains essentially zero, except for a short interval during which the particle is nearest to the cylinder. During this short interval,  $\alpha$  has a positive peak between  $t/T = 310$  and  $320$ , followed by a slightly negative value. This behavior is evident in the particle trajectory in Figure 4.2(b). At the start of the interval, indicated by the first red square, the inertial particle essentially follows the fluid particle trajectory until it reaches the region in which the streamlines of the cell change curvature, from convex (bowed outward) to concave (bowed inward). Here, the inertial particle moves significantly toward

the center of the streaming cell, consistent with the positive peak in  $\alpha$ . When the particle has traversed this region of concave streamlines, it undergoes a slight outward motion, associated with a slightly negative value of  $\alpha$ . Therefore, the inertial particle experiences the most inward motion toward the center of the streaming cell in the portion of trajectory nearest to the cylinder, while it stays on the fluid streamline on the portion farthest from the cylinder. This is evident in Figure 4.6, which depicts the mean inertial particle trajectory superposed on the mean fluid trajectories, along with the total force on the particle (that is, the right-hand side of equation (3.45) sampled at various instants). This force is largest, and consistently directed toward the center of the streaming cell, when the particle is nearest the cylinder, but its magnitude decreases dramatically when the particle is furthest from the cylinder. With each successive orbit, this process is repeated, until finally the particle becomes trapped at the center of the streaming cell.

Each contribution to  $d\alpha/dt$  from equation (4.5) is depicted in Figure 4.5(b). The Faxén terms are the earliest to contribute to positive  $\alpha$ , and are countered by the Stokes drag, the convective term, and the Basset history term, which all tend to resist this deviation from the fluid particle trajectory. The Saffman lift initiates its role somewhat later, but ultimately contributes the most positive  $d\alpha/dt$ , and is therefore most responsible for the motion toward the center of the cell. Note that all terms are significant, and none – including the Basset term – can be reliably ignored in the analysis.

The Saffman lift clearly plays an important role in the trapping of inertial particles, so we examine it further. Figure 4.7 graphically depicts the instantaneous relationships between local fluid velocity gradient, relative velocity  $\mathbf{w}$ , and lift component. Two different instants within a single oscillation cycle are shown. Generically, the Saffman lift is oriented in the gradient direction of increasing velocity when the relative velocity is opposite that of the fluid velocity (i.e. when

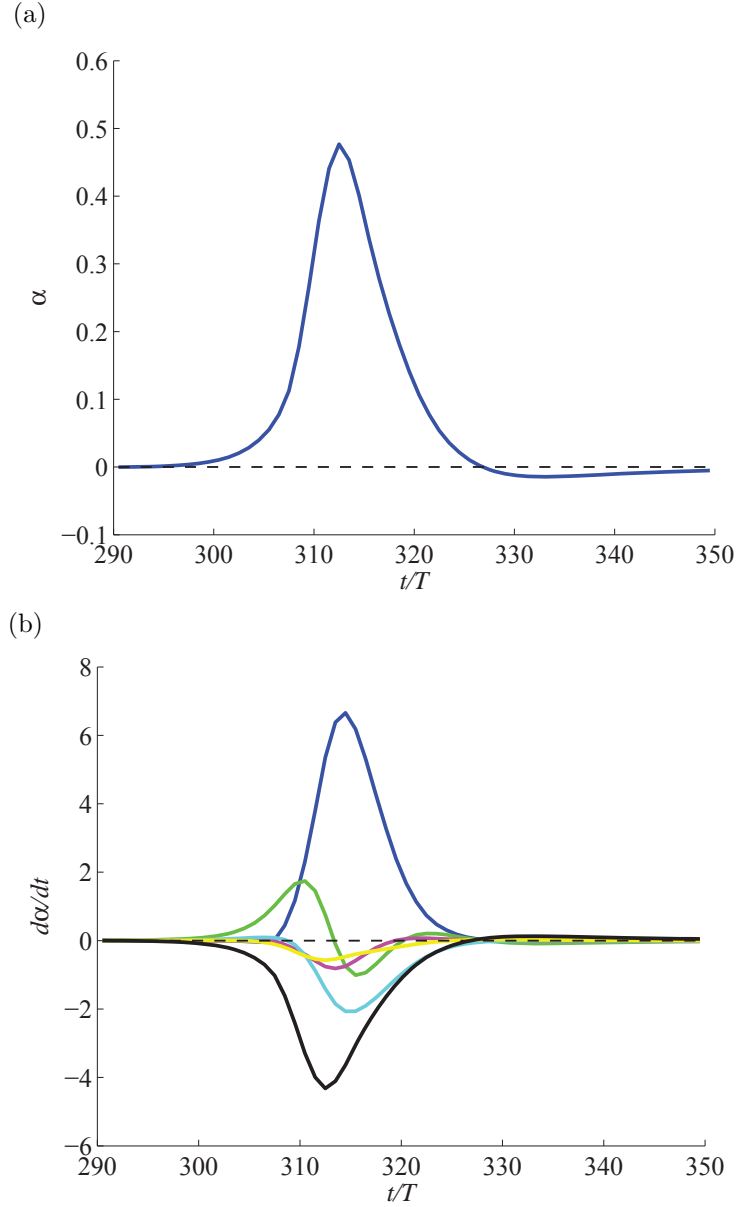


Figure 4.5: (a) History of  $\alpha$  during the cycle  $t/T \in [290, 350]$  for  $Re = 40$ ,  $a/R = 0.175$ ,  $\rho_p/\rho_f = 1$ . (b) Contributions to  $d\alpha/dt$  from each term in equation (4.5): Stokes drag (black); convective term (cyan); Basset history (magenta); Saffman lift (blue); Faxén corrections (green);  $\overline{\mathbf{w}} \times d\overline{\mathbf{U}}/dt$  (yellow).

the particle moves slower than the fluid). This is confirmed in each of the instants shown in Figure 4.7. Indeed, the component maintains the same direction at both instants shown, since the components of both  $\mathbf{w}$  and shear rate change sign during

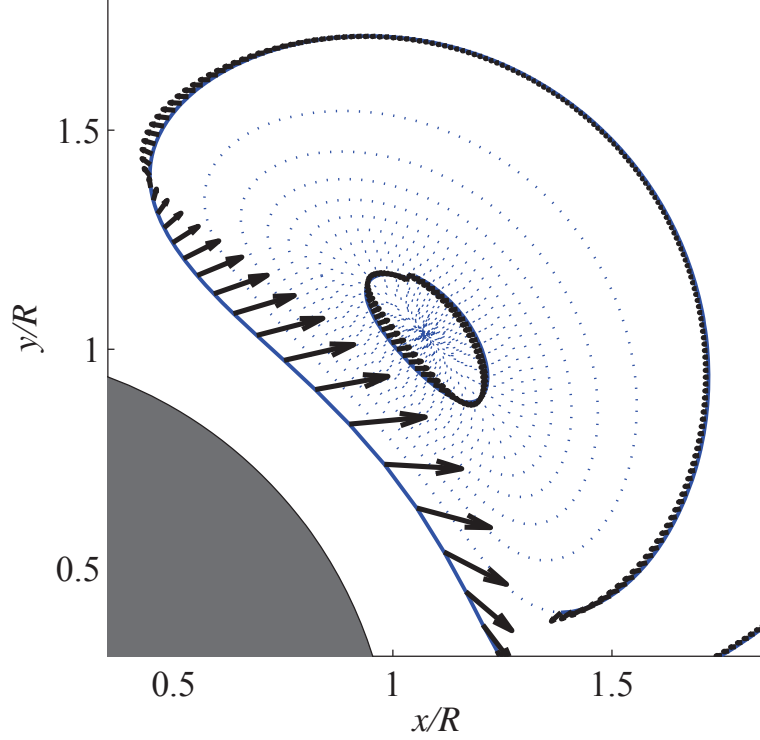


Figure 4.6: Hydrodynamic force (black arrows) at sampled times along the inertial particle trajectory (blue solid line) during the intervals  $t/T \in [0, 485]$  and  $t/T \in [1300, 1370]$  for  $Re = 40$ ,  $a/R = 0.175$  and  $\rho_p/\rho_f = 1$ . All portions of the inertial particle trajectory not in these intervals are shown as a blue dotted line.

the cycle. This ensures that there is a significant mean in the Saffman lift.

It is also important to note that the Saffman lift is only operative when the relative particle velocity,  $\mathbf{w}$ , is non-zero. By (3.45), there are only two possible mechanisms by which  $\mathbf{w}$  can become non-zero when it starts at zero: the fluid acceleration term and the Faxén corrections. For a neutrally buoyant particle, the unsteady term vanishes, and thus only the Faxén correction can cause an inertial particle to initially deviate from its fluid trajectory. This is clearly the case here, as indicated by the breakdown of contributions in Figure 4.5(b): the Faxén term is the earliest to divert the particle from the trajectory of the fluid, as the particle enters the region of significant vorticity gradient. However, once the particle has



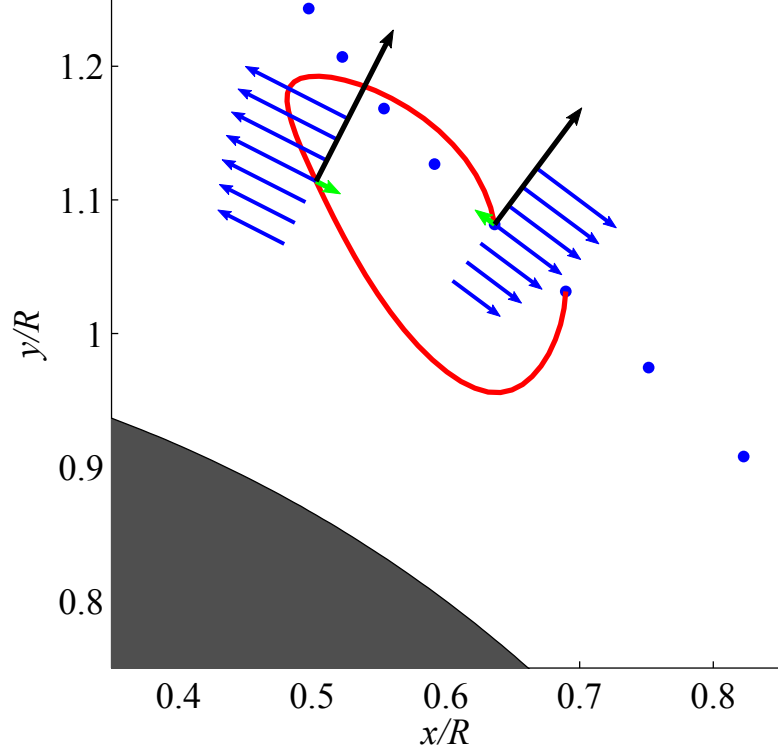


Figure 4.7: Saffman lift force (black arrow), relative particle velocity,  $\mathbf{w}$  (green arrow), and local profile of fluid velocity,  $\mathbf{u}$ , perpendicular to  $\mathbf{w}$  (blue arrows) at  $t/T = 317.5$  and  $t/T = 318$ . Velocity vectors are plotted with the same scale. Red line denotes the inertial particle trajectory during the oscillation cycle  $t/T \in [317, 318]$ . Local fluid particle trajectories, sampled once per period, shown with blue dots.

deviated, the role of the Faxén terms is secondary to that of the Saffman lift.

The final trapping point of the inertial particle is at the center of the Lagrangian streaming cell, and is not dependent on the initial location. Indeed, inertial particles travel toward nearly the same point, regardless of their size, density and initial position. We can understand this better by inspecting the mean version of the MR equation (3.45). The mean fluid particle velocity,  $\overline{\mathbf{U}}$ , vanishes at the center of this cell, and so too does  $d\overline{\mathbf{U}}/dt$  once an inertial particle reaches

	$F_x/\rho_f R^4 \Omega^2$	$F_y/\rho_f R^4 \Omega^2$
Lift	$5.65 \times 10^{-3}$	$3.61 \times 10^{-3}$
Faxén	$-3.00 \times 10^{-4}$	$1.12 \times 10^{-2}$
Basset	$3.43 \times 10^{-5}$	$-2.41 \times 10^{-4}$
Convective	$-3.98 \times 10^{-3}$	$2.59 \times 10^{-4}$
Stokes	$-1.40 \times 10^{-3}$	$-1.48 \times 10^{-2}$
Total	$-4.49 \times 10^{-7}$	$1.08 \times 10^{-6}$

Table 4.1: Time averaged forces applied on the inertial particle during the interval  $t/T \in [4200, 4700]$  for  $Re = 40$ ,  $a/R = 0.175$ ,  $\rho_p/\rho_f = 1$ .

this center. However,  $\nabla \overline{\mathbf{U}}$  and  $\nabla^2 \overline{\mathbf{U}}$  do not vanish, and thus several of the forces remain active at the center of the streaming cell, due to continuous motion from the oscillating cylinder. As Table 4.1 shows, all forces are small in magnitude in this region, and the Saffman lift and Faxén corrections remain in balance with the Stokes drag and convective term. Thus, the cell center is a fixed point of these mean equations. The continuous trajectory actually converges to a limit cycle, traversed once per oscillation cycle. This is evident in Figure 4.8, which depicts the limit cycle for neutrally buoyant inertial particles of various size (or particle Reynolds number) and fixed  $Re$ . The limit cycle is approximately the same size for all particles, and is nearly concentric with the streaming cell. The orbits have a nearly elliptical shape with a major axis of length  $0.25R$  and minor axis of length  $0.05R$  (which are likely controlled by  $\epsilon$ ) and are oriented nearly vertically.

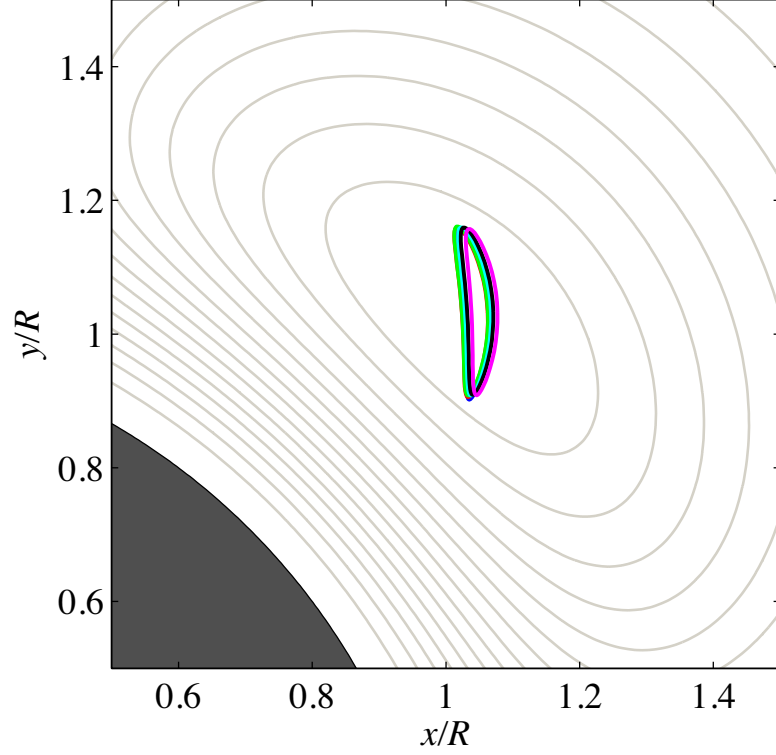


Figure 4.8: The final limit cycle for inertial particles of various sizes:  $a/R = 0.1$  (blue);  $a/R = 0.115$  (red);  $a/R = 0.13$  (green);  $a/R = 0.145$  (cyan);  $a/R = 0.16$  (black);  $a/R = 0.175$  (magenta), each plotted over one cycle for  $Re = 40$ ,  $\rho_p/\rho_f = 1$ . Mean Lagrangian streamlines shown in gray for reference.

### 4.3 Inertial particle trapping speed

It was revealed above that an inertial particle spirals inward due to the hydrodynamic forces (primarily the Saffman lift), and eventually gets trapped near the center of the Lagrangian streaming cell in a continuous limit cycle. In the trajectory sampled once per period, this particle converges to a fixed point, and the speed with which it converges is of interest.

The complex mix of forces during the trapping is dependent upon all of the parameters of the problem. Furthermore, the velocity of the particle during this trajectory is similar to that of the fluid particle,  $V_s \sim \epsilon\Omega A = \epsilon^2\Omega R$ . However, the

forces on the particle during trapping, notably the Stokes drag and Saffman lift, have a mix of linear and non-linear dependence on velocity. Thus, one expects that  $\tau/T$  – the timescale of trapping, scaled by period  $T = 2\pi/\Omega$  – depends inversely on  $\epsilon$  to some power, but all parameters –  $\epsilon$ ,  $Re$ ,  $a/R$ , and  $\rho_p/\rho_f$  – determine the shape of the spiral trajectory. Thus, the trapping timescale obeys

$$\frac{\tau}{T} = f(\epsilon, Re, a/R, \rho_p/\rho_f) \quad (4.7)$$

The dashed line in Figure 4.9(a) is the history of the  $x$  component of position of the inertial particle (sampled once per period) and exhibits an asymptotic decay toward a steady position. A criterion to establish convergence is that the difference between two consecutive peaks in this sampled history falls below a threshold value ( $10^{-4}$ ). Once the inertial particle is determined to be converged, the trapping timescale can be determined by fitting an exponential curve  $K \exp(-t/\tau)$  to the envelope of the history, as depicted by the solid line in Figure 4.9(a).

Three cases are investigated by varying one of the parameters (density, particle size and Reynolds number), while fixing the remaining parameters. Figure 4.9(b) indicates that, as the size of the particle (and thus, the particle Reynolds number,  $Re_a = \Omega a^2/\nu$ ) increases, so too does the speed of convergence toward the trapping point. This is due to the decreased resistance from the Stokes drag in the MR equation. This term is proportional to the inverse of the particle Reynolds number, whereas the Saffman lift is proportional to the inverse root, and is thus less affected by the increase. This result is consistent with the experimental results of Lutz *et al.* [43], who found that very small particles are not trapped effectively. Note that Figure 4.9(b) also exhibits the dependence on  $\epsilon$ . As expected, the trapping speed is higher as  $\epsilon$  increases.

Figure 4.9(c) shows that, as particle density increases, the convergence speed decreases. Inspection of (4.5) shows that all terms contributing to  $d\alpha/dt$ , except for the unsteady term (with factor  $C_u$ ), are weakened by an increase in particle

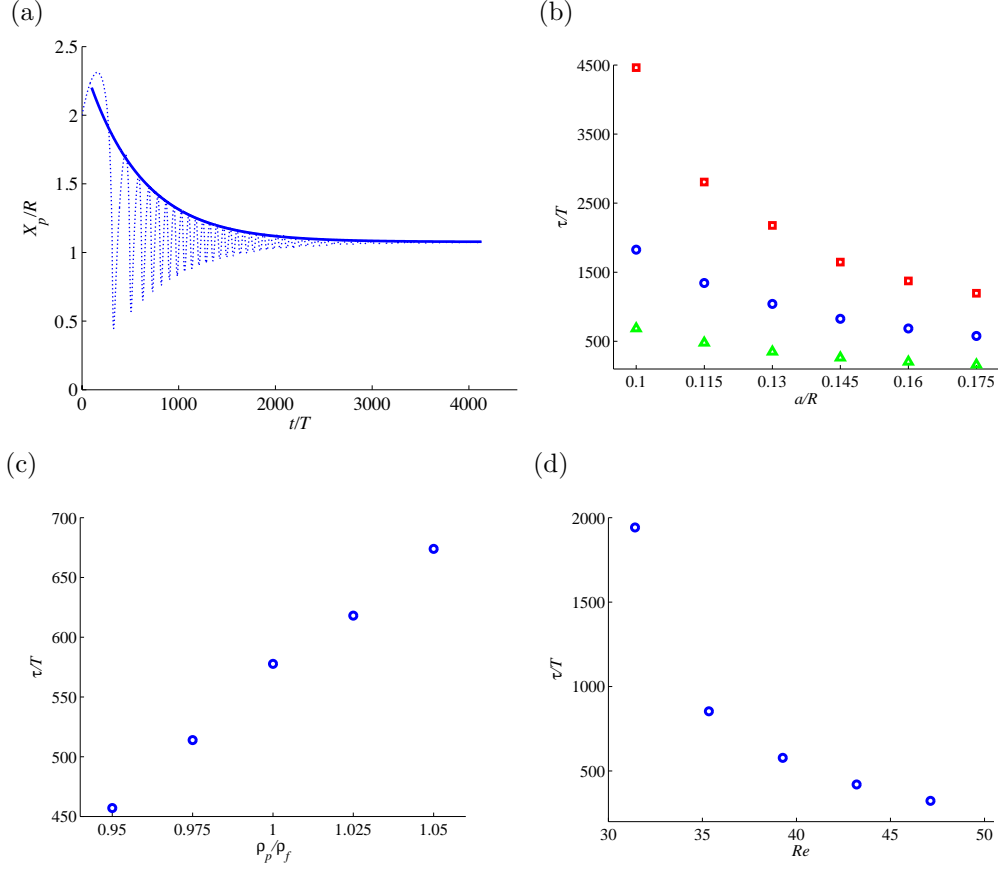


Figure 4.9: (a) The sampled history of the  $x$  position of an inertial particle (---) and an exponential fit to the envelope (—), for  $Re = 40$ ,  $\rho_p/\rho_f = 1$  and  $a/R = 0.175$ . (b) Trapping timescale dependence on  $a/R$ , for  $Re = 40$ ,  $\rho_p/\rho_f = 1$ . This figure contains results for  $\epsilon = 0.2\sqrt{2}$  (green triangles), 0.2 (blue circles), 0.1 (red squares). (c) Trapping timescale dependence on  $\rho_p/\rho_f$  for  $Re = 40$ ,  $a/R = 0.175$ . (d) Trapping timescale dependence on  $Re$  for  $\rho_p/\rho_f = 1$ , with  $a/R$  varied so that  $\Omega a^2/\nu$  is fixed at 1.2.

inertia. Though this unsteady term can enhance trapping as density ratio increases (by virtue of centripetal acceleration), its effect for density ratios near unity is more than compensated for by the decreased effectiveness of the Saffman lift and Faxén correction terms, which are dominant in this regime.

Finally, Figure 4.9(d) shows that trapping speed also increases with increasing

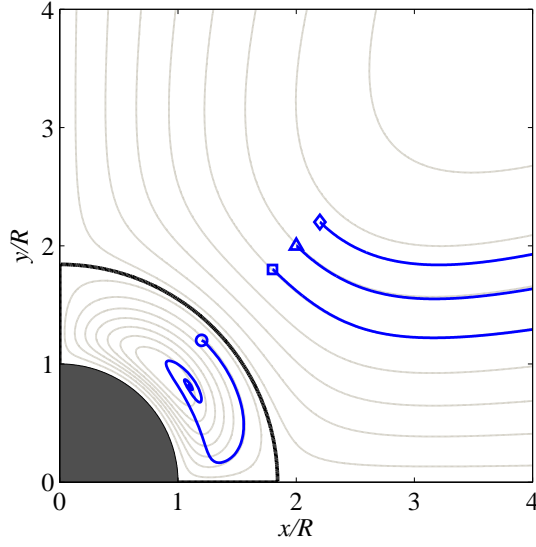


Figure 4.10: Inertial particle trajectories at  $Re = 80$  for particle of density  $\rho_p/\rho_f = 1$  and radius  $a/R = 0.175$ , initially located at  $(1.2R, 1.2R)$  ( $\circ$ ),  $(1.8R, 1.8R)$  ( $\square$ ),  $(2R, 2R)$  ( $\triangle$ ),  $(2.2R, 2.2R)$  ( $\diamond$ ). Lagrangian streamlines are in light gray.

Reynolds number when the particle Reynolds number is fixed. Since the particle Reynolds number is fixed, the viscous resistance does not change. However, the underlying flow field has been altered by an increase in  $Re$ , and particularly, the strengths of the vorticity and velocity gradients have increased. Thus, the Faxén terms and the Saffman lift are enhanced by the stronger gradients, increasing the tendency toward trapping.

#### 4.4 Inner and outer streaming

The results thus far have focused on the behavior of inertial particles in the inner streaming cell. At Reynolds number  $Re = 40$ , this cell has a thickness  $\delta_{DC} \approx 4.6R$ , so that the boundary of the cell is on the periphery of the viewing window in Figure 4.2. However, this thickness shrinks to  $0.82R$  at  $Re = 80$ , so that the

cell is more compact, as shown in Figure 4.10. It is natural, then, to explore the behavior of inertial particles released from points outside the boundary of the streaming cell. This region is characterized by mean Lagrangian streamlines that do not form closed loops, but rather, direct fluid particles toward the cylinder in the 90 degree sectors centered on the  $y$  axis, and away from the cylinder in the sectors centered on the  $x$  axis. Figure 4.10 depicts the trajectories of a neutrally buoyant inertial particle of radius  $a/R = 0.175$  released from various points. The particle released from a point well inside the inner streaming cell remains inside the cell and spirals toward a fixed point. Particles released well outside the cell remain outside, and travel approximately along fluid particle trajectories (expected due to the small velocity and vorticity gradients in this region).

## CHAPTER 5

### Inertial Particle Transport

In this chapter, inertial particle transport between multiple cylinders in streaming flow generated by oscillating cylinders is considered. First, background streaming flow is obtained from VVPM and BEM for inertial particle transport inside and outside inner streaming cell, respectively. In VVPM simulations, the sequence of starting and stopping the oscillation of individual cylinder is controlled to transport the inertial particle in predictable manner. In BEM simulations, appropriate boundary conditions are applied on each cylinders to generate streaming flow according to the sequence of starting and stopping the oscillation of cylinders. Then these background flow will be used to integrate the modified Maxey-Riley equation including wall effect. Several arrangement of oscillating cylinders such as two cylinders, three cylinders in triangular arrangement and four cylinders in zigzag arrangement are considered and their inertial particle trapping and transport behaviors are explored.

#### 5.1 Problem Statement

As is revealed in chapter 4, inertial particles inside inner streaming cell follow the swirling trajectory and finally becomes trapped in the center of inner streaming cell. Therefore streaming flow generated by another oscillating cylinder would drag the trapped particle into the streaming cell and finally it will be trapped inside the center of newly established streaming cell. A simple inertial particle transport between two oscillating cylinders is considered first.



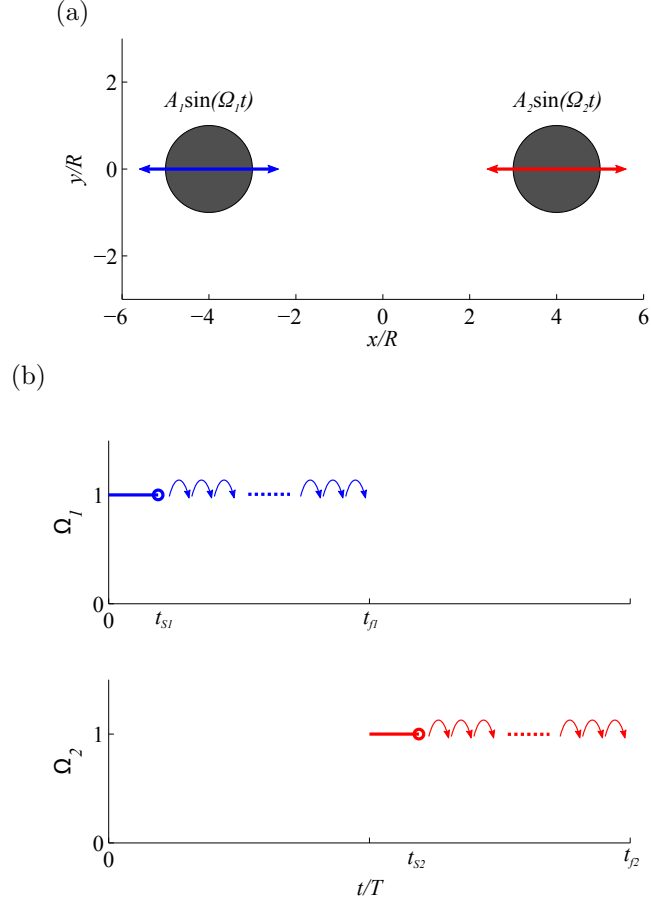
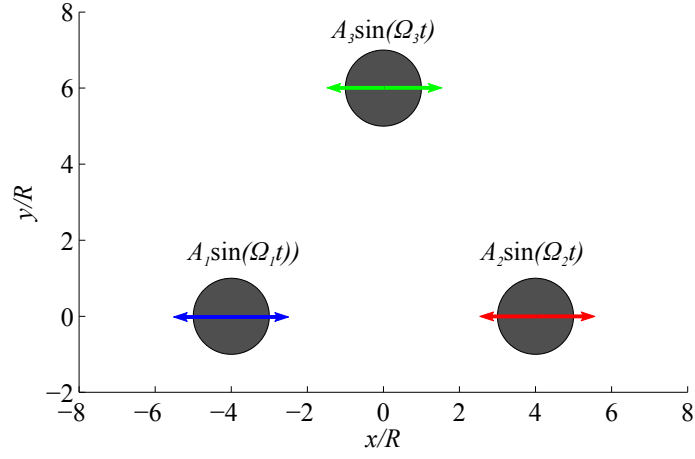


Figure 5.1: Schematic of two oscillating cylinders and the sequence of their oscillations. (a) Oscillating two-dimensional cylinders with amplitude  $A_1$ ,  $A_2$  and frequency  $\Omega_1$ ,  $\Omega_2$ . (b) Sequence of oscillating cylinders in VVPM. Streaming flow is generated by left cylinder until  $t/T = t_{s1}$  (blue solid line) and one oscillating cycle is then used to integrate inertial particle trajectory until it is finally trapped at  $t/T = t_{f1}$  (blue dot line). Right cylinder start to oscillate at  $t/T = t_{f1}$  and generate streaming flow until  $t/T = t_{s2}$  (red solid line). Every cycle during  $t/T = t_{f1} \sim t_{s2}$  and then one oscillating cycle is used to compute the transport of trapped inertial particle until it is trapped in newly established streaming cell by right cylinder at  $t/T = t_{f2}$  (red dot line).

(a)



(b)

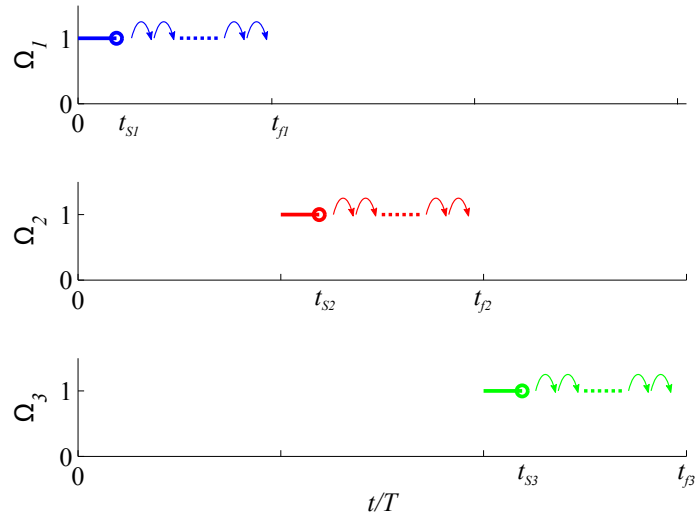
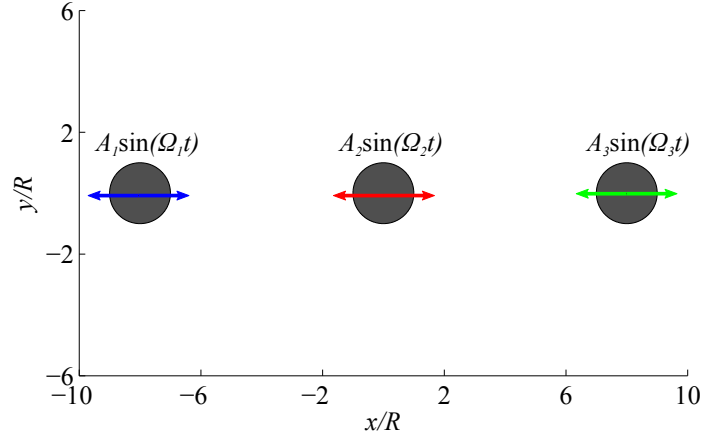


Figure 5.2: Schematic of oscillating cylinders in triangular arrangement and the sequence of their oscillations. (a) Oscillating two-dimensional cylinders of with amplitude  $A_1$ ,  $A_2$ ,  $A_3$  and frequency  $\Omega_1$ ,  $\Omega_2$ ,  $\Omega_3$ . (b) Sequence of oscillating cylinders in VVPM is similar to sequence of two cylinders in figure 5.1 (b).

(a)



(b)

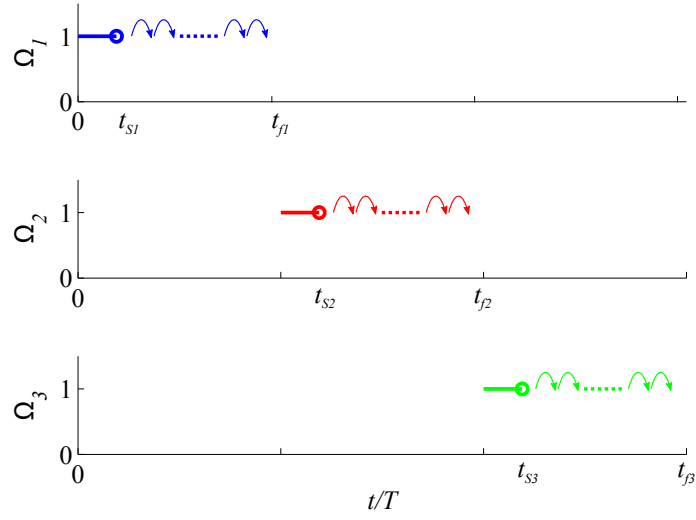
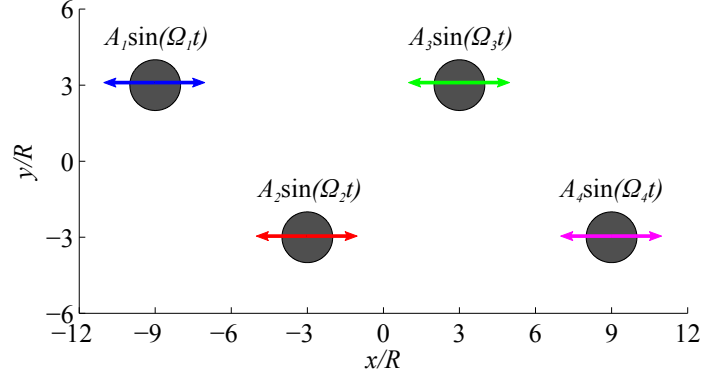


Figure 5.3: Schematic of oscillating cylinders in line arrangement and the sequence of their oscillations. (a) Oscillating two-dimensional cylinders of with amplitude  $A_1$ ,  $A_2$ ,  $A_3$  and frequency  $\Omega_1$ ,  $\Omega_2$ ,  $\Omega_3$ . (b) Sequence of oscillating cylinders in VVPM is similar to sequence of two cylinders in figure 5.1 (b).

(a)



(b)

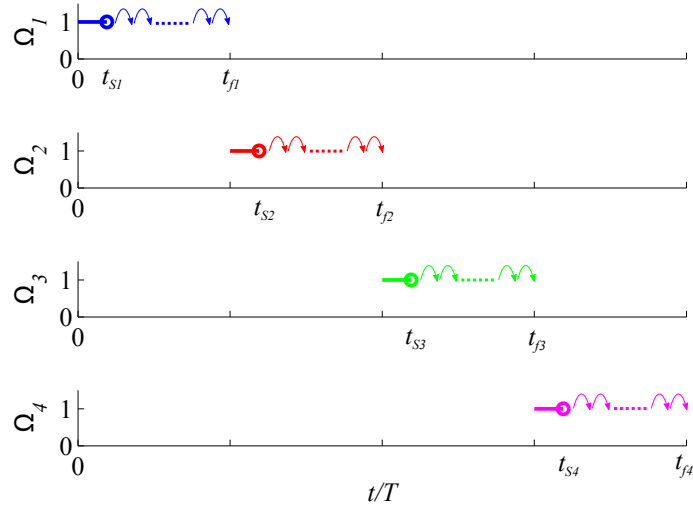


Figure 5.4: Schematic of oscillating cylinders in zigzag arrangement and the sequence of their oscillations. (a) Oscillating two-dimensional cylinders of with amplitude  $A_1$ ,  $A_2$ ,  $A_3$ ,  $A_4$  and frequency  $\Omega_1$ ,  $\Omega_2$ ,  $\Omega_3$ ,  $\Omega_4$ . (b) Sequence of oscillating cylinders in VVPM is similar to sequence of two cylinders in figure 5.1 (b).

Left cylinder located at  $(-4R, 0)$  is initially oscillated with rectilinear sinusoidal motion with amplitude  $A_1$  and frequency  $\Omega_1$  in figure 5.1 (a). After inertial particle is trapped inside the inner streaming cell generated by left oscillating cylinder, stop the oscillation of left cylinder and start the oscillation of right cylinder located at  $(4R, 0)$  with amplitude  $A_2$  and frequency  $\Omega_2$  to initiate the motion of trapped inertial particle and transport the particle inside the newly established streaming cell by right oscillating cylinder. This is basic particle transport strategy when employing either VVPM or BEM to generate streaming flow. VVPM, however, cannot generate streaming flow until inertial particle is trapped and transported toward another designated points, which needs more than several tens of thousand oscillations. This is computationally expensive and inefficient. Instead, VVPM stop generating flow field after the streaming flow field does not evolve anymore and thus it can be regarded as some steady state, and one oscillating cycle after steady state is used repeatedly to calculate inertial particle trajectory.

Figure 5.1 (b) describes oscillation sequences. In VVPM, streaming flow is generated by oscillating left cylinder until  $t/T = t_{s1}$  ( $T$  is representative time scale, i.e.  $1/\Omega$ ) when the streaming flow field is reached to steady state. Then one oscillating cycle after  $t/T = t_{s1}$  is repeatedly used to integrate inertial particle trajectory until it is finally trapped inside the center of streaming cell generated by left cylinder at  $t/T = t_{f1}$ . Right cylinder then start to oscillate at  $t/T = t_{f1}$  and starts to generate streaming flow until  $t/T = t_{s2}$  when the streaming flow by right cylinder reaches to steady state. Meanwhile, the trapped inertial particle initiate its motion due to the streaming flow generated by right cylinder during  $t/T = t_{f1} \sim t_{s2}$ , in which every cycle needs to be integrated to take account the transient streaming effect between two cylinders. Then, one oscillating cycle after  $t/T = t_{s2}$  is again used to compute the inertial particle transport motion until it is finally trapped inside the center of newly established streaming cell by right

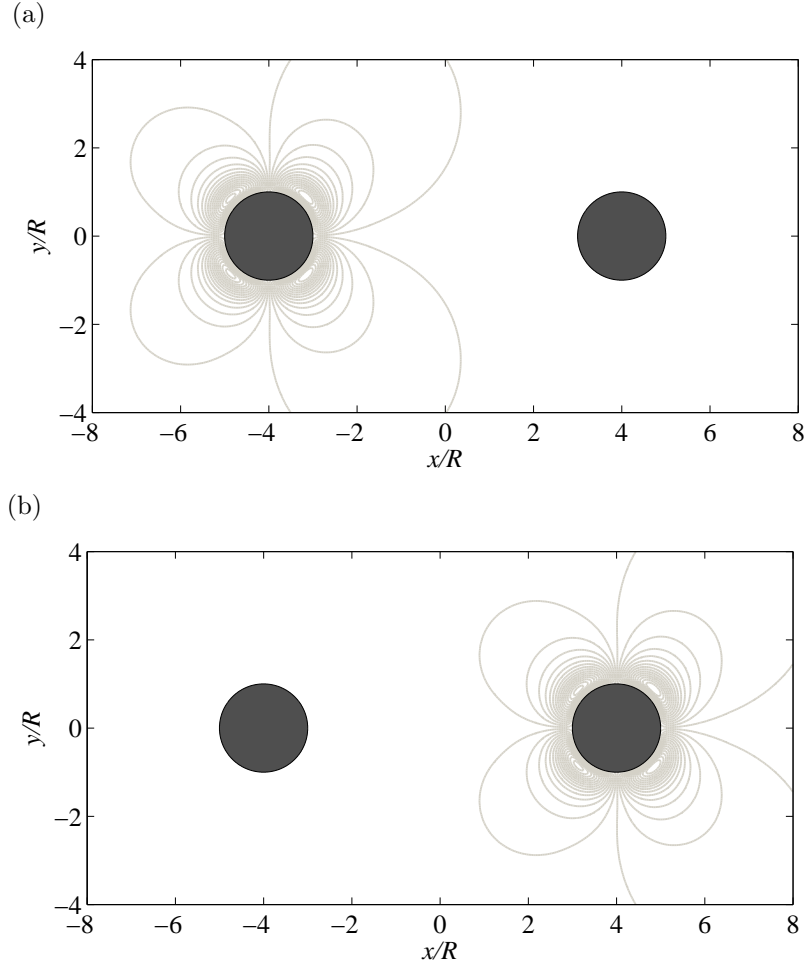


Figure 5.5: Contour of streamline of oscillating two cylinders from VVPM . Streaming flows are obtained from oscillation of (a) left  $(-4R, 0)$  and (b) right  $(4R, 0)$  cylinder, respectively.

cylinder at  $t/T = t_{f2}$ .

Similarly, inertial particle transport in triangular arrangement (figure 5.2) , line arrangement (figure 5.3) and zigzag arrangement (figure 5.4), respectively, is considered.

Streaming flow generated by oscillating two cylinder is depicted in figure 5.5 (a). Left cylinder oscillates until  $t_{s1} = 20$  and stop oscillating left cylinder and start to oscillate right cylinder until  $t_{s1} = 40$ . Each plot is steady 2nd-order streamlines,  $\Psi_2^s$  in equation 2.23, by averaging the instantaneous streamfunctions

over one oscillating period during  $t_{s1} = t/T = 19 \sim 20$  and  $t_{s2} = t/T = 39 \sim 40$ , respectively. Streaming flow pattern describes well the behavior of inner streaming cell and the other stationary cylinder is located inside this inner streaming cell. Thus inertial particle transport between oscillating cylinder is occurred inside inner streaming cell. Unequal streamlines from the center of oscillating axis still remains in flows and this asymmetric effect is expected to diminish as simulation period increases ( increase  $t_{s1}$  and  $t_{s2}$  ) and resolution of simulation increases ( decrease grid size  $dx$  ). In these simulations of multiple oscillating cylinders, oscillation amplitude and grid size are  $\epsilon = 0.1$  and  $dx = 0.02$ , respectively.

Likewise, streaming flows generated by oscillating cylinders in triangular arrangement, line arrangement and zigzag arrangement from VVPM are shown in figure 5.6, 5.7 and 5.8, respectively. Similar inner streaming cell is generated and other fixed cylinders is located inside inner streaming cell.

Before using this streaming flow to integrate the inertial particle trajectory, it is important to explore characteristics of streaming flow at several points. Figure 5.9 depicts the history of velocities,  $\mathbf{U}_x$  and  $\mathbf{U}_y$  at (a)  $(-2R, 2R)$ , (b)  $(0, 2R)$  and (c)  $(2R, 2R)$  during  $t/T = 0 \sim 40$  and describes well the oscillatory flow field as cylinders oscillate. One thing to note is that the magnitude of velocity,  $\mathbf{U}_x$  at  $(-2R, 2R)$ , which is close to the left cylinder, increases when the oscillating cylinder is changed from left cylinder to right cylinder although the distance from the oscillating cylinder is increased. This is because the point located near the center of streaming cell, where flow is stationary, is located further from the newly established center by changing oscillating cylinder. However the magnitude of  $\mathbf{U}_y$  at  $(-2R, 2R)$  has reversal result, (i.e., the magnitude of velocity decreased as the oscillating cylinder is changed from left to right). Similar behavior is observed at  $(2R, 2R)$ .

It is important to note that the velocity field reflects instantaneous oscillating motion from the cylinders. Velocity field instantaneously captures the onset of

oscillation of left cylinder and transition of oscillation from left cylinder to right cylinder as shown in figure 5.9. This is because the dominant, 1st order streaming flow in eq. (2.10) is pressure driven flow and thus the oscillating motion from the cylinder is instantaneously conveyed. However this 1st order streaming flow cannot discern whether flow approaches to steady state or not since streaming motion is 2nd order steady flow generated by interaction of this 1st order, oscillatory flow.

History of averaged velocities over one period oscillation,  $\overline{U}_x$  and  $\overline{U}_y$  during  $t/T = 0 \sim 40$  at these points is also explored in figure 5.10: (a) at  $(-2R, 2R)$ , (b) at  $(0, 2R)$  and (c) at  $(2R, 2R)$ . Averaging the velocities over one cycle removes the oscillatory part of 1st and 2nd order solution and thus 2nd order steady solution is left. Sudden impulsive velocity peaks at the beginning of oscillation of cylinders ( $t/T = 0$  from left cylinder and  $t/T = 20$  from right cylinder) subside after several oscillations. Distinct from the history of velocities in figure 5.9 averaged velocities exhibits steady portion with several oscillation after new streaming flow is generated from oscillating cylinders. This steady portion obtained after several oscillations ( $t_{s1}, t_{s2}, \dots$ ) enable us to employ one oscillating cycle repeatedly to compute inertial particle trajectory, and thus it saves a lot of computational effort without losing a significant accuracy. The value of steady portion depends of computational tolerance and tolerance of current VVPM simulation ( $10^{-6}$ ) is reasonably small enough to capture streaming flow between oscillating cylinders inside inner streaming cell.



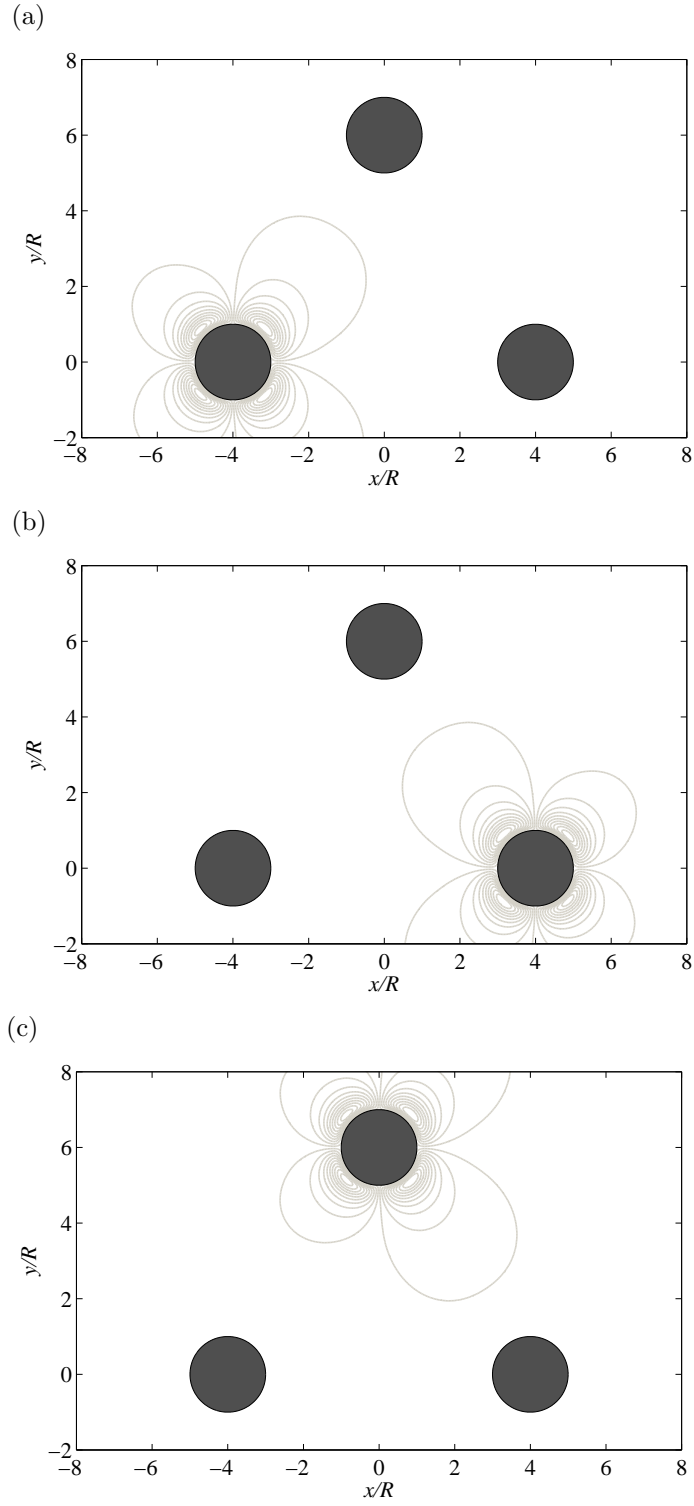


Figure 5.6: Contour of streamline of oscillating cylinders in triangular arrangement from VVPM. Streaming flows are obtained from oscillation of (a) lower left  $(-4R, 0)$ , (b) lower right  $(4R, 0)$  and (c) upper  $(0, 6R)$  cylinder, respectively.

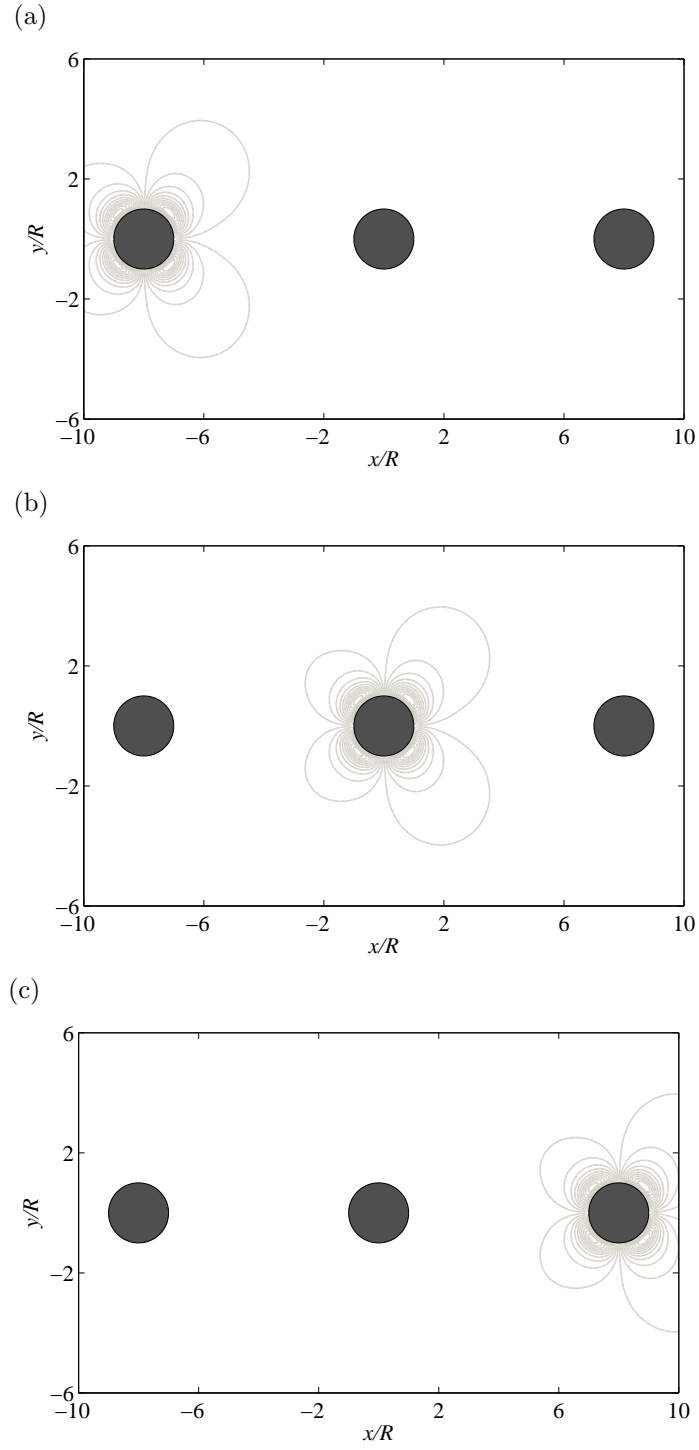


Figure 5.7: Contour of streamline of oscillating cylinders in line arrangement from VVPM. Streaming flows are obtained from oscillation of (a) left  $(-8R, 0)$ , (b) center  $(0, 0)$  and (c) right  $(8R, 0)$  cylinder, respectively.

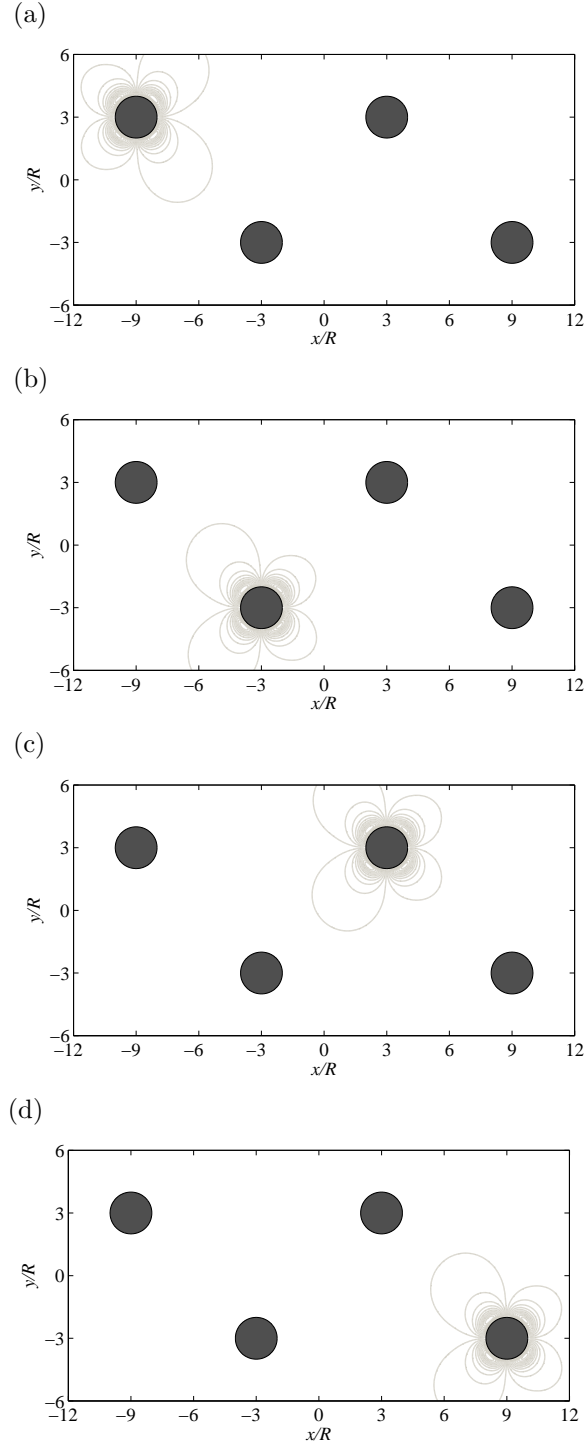


Figure 5.8: Contour of streamline of oscillating cylinders in line arrangement from VVPM. Streaming flows are obtained from oscillation of (a) upper left  $(-9R, -3R)$ , (b) lower left  $(-3R, -3R)$ , (c) upper right  $(3R, 3R)$  and (d) lower right  $(9R, -3R)$  cylinder, respectively.

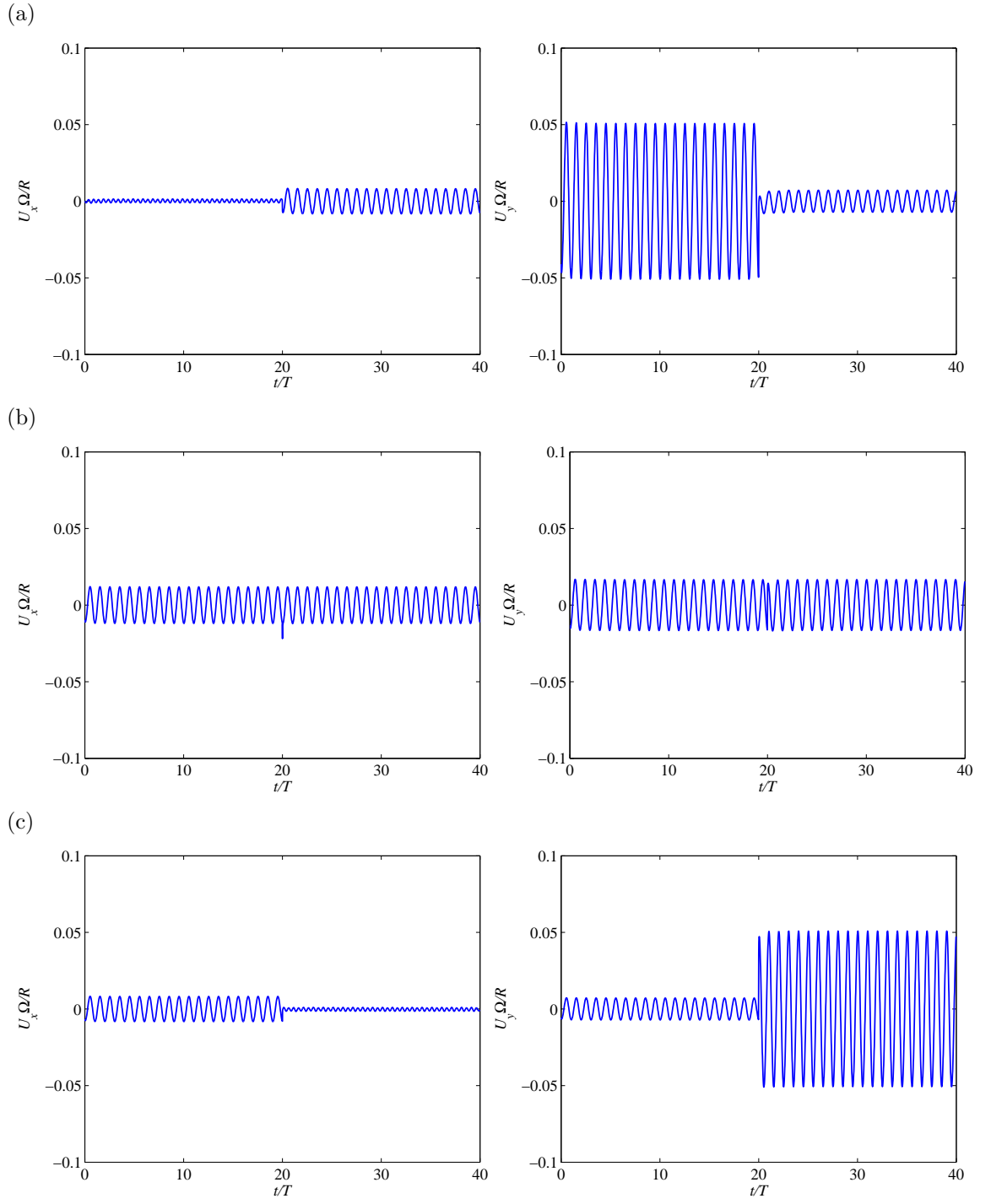


Figure 5.9: History of velocities,  $U_x$  and  $U_y$  at (a)  $(-2R, 2R)$ , (b)  $(0, 2R)$  and (c)  $(2R, 2R)$  during  $t/T = 0 \sim 40$ .

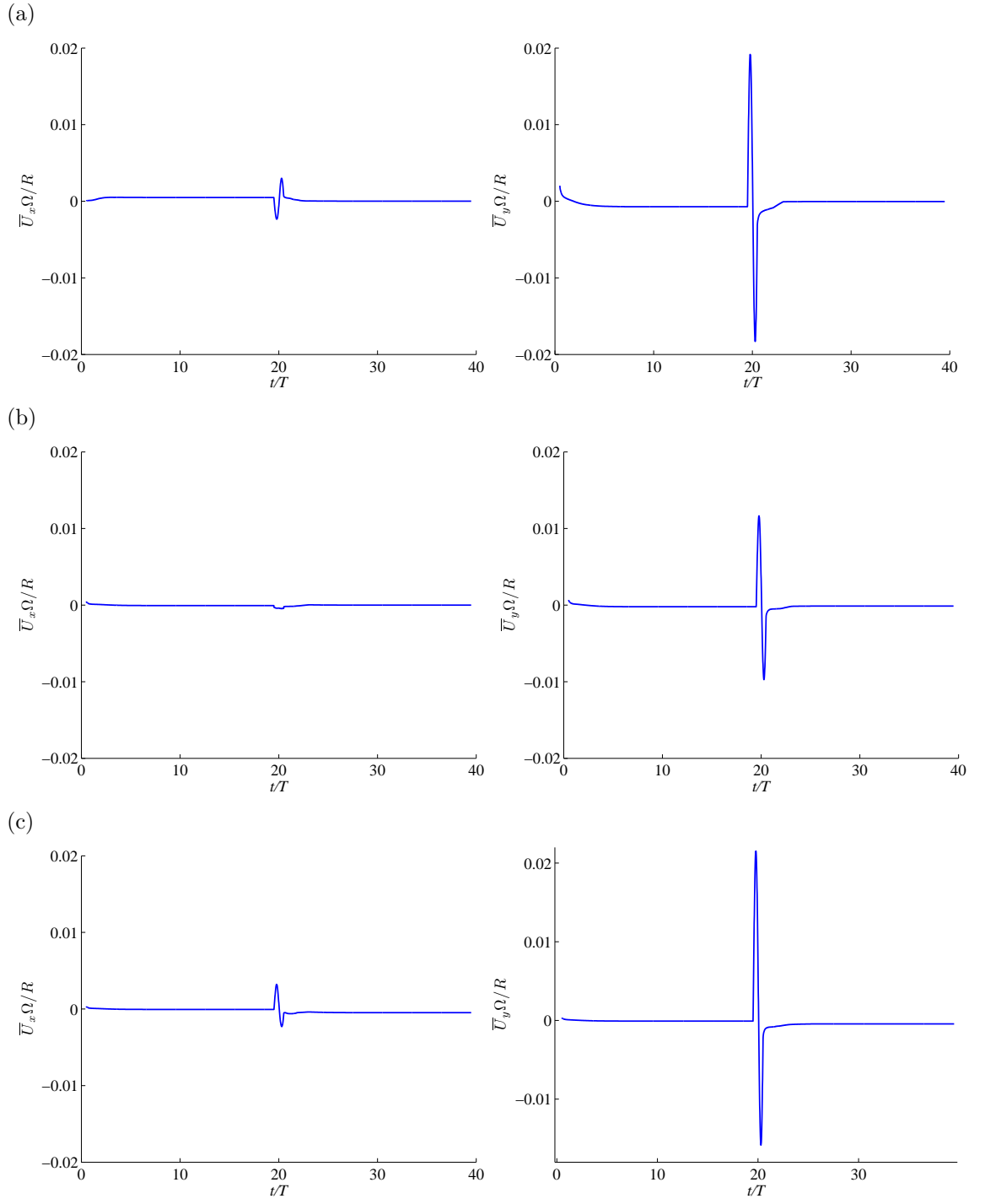


Figure 5.10: History of averaged velocities over one period oscillation,  $\bar{U}_x$  and  $\bar{U}_y$  at (a)  $(-2R, 2R)$ , (b)  $(0, 2R)$  and (c)  $(2R, 2R)$  during  $t/T = 0 \sim 40$ .

## 5.2 Modified Maxey-Riley Equation

The motion of inertial particle between cylinders is different from the motion in streaming flow generated by single oscillating cylinder in that the trapped inertial particle follows the outmost streamline by the streaming flow and approaches closely toward oscillating cylinder. Then it could experience liquid-solid interaction force inside thin lubrication layer between inertial particle and surface of cylinder, and moreover it could directly collide with the surface of cylinder. Therefore wall effect such as lubrication force and elastic collision force from the direct contact with cylinder are newly included. Here, Basset history force term is ignored for simplicity purpose as well as its relative small contribution in this study in figure 4.5 (b). Thus the final modified MR equation is,

$$\frac{d\mathbf{X}_p}{dt} = \mathbf{V}_p \quad (5.1)$$

$$\begin{aligned} m_p \frac{d\mathbf{V}_p}{dt} = & -6\pi\rho_f\nu a \left[ (\mathbf{V}_p(t) - \mathbf{u}(\mathbf{X}_p(t), t)) \lambda - \frac{1}{6}a^2\nabla^2\mathbf{u}(\mathbf{X}_p(t), t) \right] + m_f \frac{D\mathbf{u}}{Dt} \Big|_{\mathbf{X}_p(t)} \\ & - \frac{1}{2}m_f \left( \frac{d\mathbf{V}_p}{dt} - \frac{D\mathbf{u}}{Dt} \Big|_{\mathbf{X}_p(t)} - \frac{d}{dt} \left[ \frac{1}{10}a^2\nabla^2\mathbf{u}(\mathbf{X}_p(t), t) \right] \right) \\ & + 4K\rho_f a^2 (\nu |G|)^{1/2} \text{sgn}(G) |\mathbf{u} - \mathbf{V}_p| \mathbf{n} + F \left( \frac{\delta}{\delta_{ss}} \right) e_d W_o, \end{aligned} \quad (5.2)$$

where

$$\lambda = \frac{1}{2\delta} H \left( \frac{\delta}{\delta_{sl}} \right) + 1.0 \times \left[ 1 - H \left( \frac{\delta}{\delta_{sl}} \right) \right] \quad (5.3)$$

and

$$F \left( \frac{\delta}{\delta_{ss}} \right) = \begin{cases} \frac{e^{(-\delta/\delta_{ss})} - e^{-1}}{1 - e^{-1}} & 0 \leq \delta \leq \delta_{sq} \\ 0 & \delta > \delta_{ss} \end{cases} \quad (5.4)$$

and

$$W_o = \frac{4}{3}a^2 E^* \left( \frac{5\pi}{4E^*} \rho_p V_I^2 \right)^{3/5} \quad (5.5)$$

Each terms of right hand side of equation (3.45) represent mixed viscous drag force with Faxén corrections, unsteady force, added mass force, and elastic colli-

sion force respectively.  $\lambda$  represent mixed viscous drag force coefficient between lubrication force by G. I. Taylor and Stokes force, which are blended by smoothed Heaviside function,  $H(\delta/\delta_{sl}) = 1/(1 + e^{10(\delta/\delta_{sl}-1)})$ .  $\delta$  represent nondimensionalized gap distance between wall (surface of cylinder) and particle surface by particle diameter.  $\delta_{sl}$  is chosen as 0.5. As the gap distance decrease, viscous drag significantly increase and thus make inertial particle velocity approach quickly to background fluid velocity while viscous drag recovers Stokes drag force as the gap distance increase. Last term represents elastic collision force between inertial particle and cylinder based on Hertz elastic force by Timoshenko and Goodier [80] and Hunt, Li, and Colonius [90]. This elastic force  $W_o$  thus becomes active only when the gap,  $\delta$ , is less than  $\delta_{ss}$  and becomes unity when  $\delta$  approach to zero.  $\delta_{ss}$  and dry coefficient of restitution  $e_d$  is set as 0.017 and 0.97 respectively [90].  $V_I$  is particle impact velocity relative to velocity of oscillating cylinder and  $E^* = [(1 - \nu_1^2)/E_1 + (1 - \nu_2^2)/E_2]^{-1}$  is reduced modulus combining Young's Modulus  $E$  with Poisson ratio  $\nu$ . As in the previous equation in (3.45) it is more natural to utilize relative velocity between inertial particle and fluid,  $\mathbf{w} = \mathbf{V}_p - \mathbf{u}(\mathbf{X}_p)$ , then nondimensionalized form of above equation (5.2) by  $R$  and  $\Omega$  is

$$\begin{aligned} \left(\frac{\rho_p}{\rho_f} + \frac{1}{2}\right) \frac{d\mathbf{w}}{dt} = & -\frac{9}{2} Re_a^{-1} \mathbf{w} \lambda + (1 - \rho_p/\rho_f) \frac{d\mathbf{u}}{dt} \Big|_{\mathbf{X}_p(t)} - \frac{3}{2} \mathbf{w} \cdot \nabla \mathbf{u} \Big|_{\mathbf{X}_p(t)} \\ & + 3K Re_a^{-1/2} |G|^{1/2} \text{sgn}(G) |\mathbf{w}| \mathbf{n} + F \left(\frac{\delta}{\delta_{ss}}\right) e_d W_o \\ & + \frac{3}{4} Re_a^{-1} (a/R)^2 \nabla^2 \mathbf{u}(\mathbf{X}_p(t), t) + \frac{1}{20} (a/R)^2 \frac{d}{dt} [\nabla^2 \mathbf{u}(\mathbf{X}_p(t), t)]. \end{aligned} \quad (5.6)$$

where

$$W_o = \frac{R}{a} \left( \frac{5 \rho_p}{4 \rho_f} V_I^2 \right)^{3/5} \left( \frac{E^*}{\pi} \right)^{2/5} \quad (5.7)$$

In this problem, reduced modulus and Poisson ratio is respectively,  $E^* = 3\text{GPa}$ ,  $\nu = 0.35$ . According to the previous chapter 2, the convective time scale

for inertial particle to orbit the streaming cell is order of  $1/\epsilon^2$  oscillations, which may need more than several thousands steps of time integration. The computation efforts even increase if the inertial particle is located further from the cylinder, where fluid motion is weak. In this far-region, however Faxén corrections term is zero since the vorticity,  $\omega = -\nabla^2 \mathbf{u}$ , generated from cylinder oscillation is zero. Thus for neutrally buoyant inertial particle, it does not have any non-zero forcing terms and thus relative velocity is zero  $\mathbf{w} = 0$ , which leads inertial particle to behave as fluid particle. Therefore, in case of using VVPM to integrate inertial particle trajectory, the computation effort can be significantly reduced if the trajectory of inertial particle is integrated by Mean Lagrangian Velocity (MLV) [42, 65] in the region where the vorticity is zero,

$$\overline{\mathbf{U}} = \overline{\mathbf{u}} + \overline{\int_0^t \mathbf{u} \, d\tau \cdot \nabla \mathbf{u}}. \quad (5.8)$$

where the temporal mean  $\overline{(\cdot)}$  is defined in equation (2.45). The first term of right hand side of equation (5.8) is a mean Eulerian velocity which is a 2nd order steady velocity and second term is a mean Stokes drift which correct the difference between mean Lagrangian and mean Eulerian velocity. Therefore fluid particle is transported by mean Lagrangian velocity (5.8) and inertial particle can also be integrated using MLV once a period in a far-region, so that computational effort can be reduced significantly.

The comparison between trajectories from complete MR (blue line) and MLV (red line) equation is made in figure 5.11. Both inertial particles starts initially from  $(x, y) = (4R, 4R)$  and hardly exhibit deviation from each other until  $t/T = 21316$ , where the vorticity is not zero anymore and thus trajectory integration from MLV stops. This indicates using MLV can integrate the inertial particle trajectory not only precisely but also efficiently. Therefore, inertial particle is integrated by complete MR near the cylinder and MLV away from the cylinder.



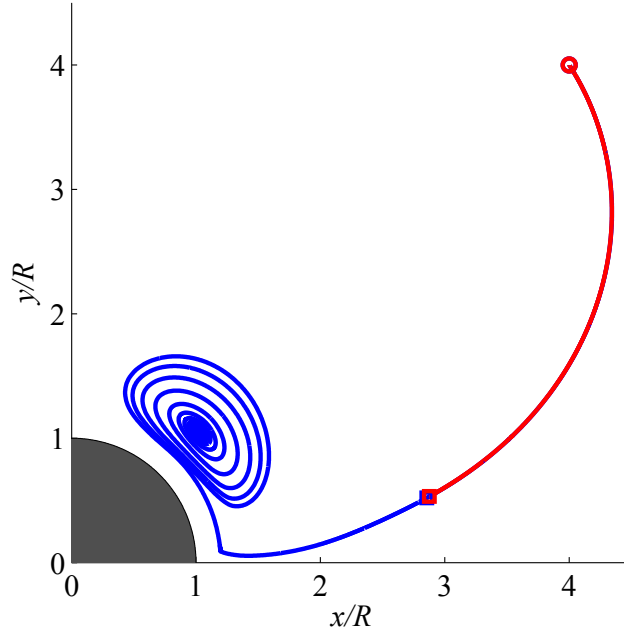


Figure 5.11: Inertial particle trajectory from complete MR (blue line) and MLV (red line) for  $Re = 40$ ,  $A/R = 0.1$ ,  $a/R = 0.175$  and  $\rho_p/\rho_f = 1$ . Each open circles and squares are positions of inertial particles at  $t/T = 0$  and 21316, respectively.

### 5.3 Transport inside Stokes layer

Simple inertial particle transport between oscillating cylinders inside inner streaming cell (Stokes layer) is considered first in figure 5.3. Streaming flow is first generated by VVPM with strategy in figure 5.1. Left cylinder oscillates until streaming flow reaches to steady state at  $t_{s1} = 20$  and right cylinder starts to oscillate until at  $t_{s2} = 40$ . Then inertial particle trajectory is integrated with modified MR equation (5.6) using each oscillating cycles ( $t/T \in [19, 20]$  and  $t/T \in [39, 40]$ ). Inertial particle first initiate its motion from  $(-2R, 2R)$  by the oscillation of left cylinder and becomes trapped inside the inner streaming cell after following inward swirling trajectory during  $t/T \in [0, 6784]$  (blue line). The trapped inertial particle starts to move toward right cylinder following the outmost stream line generated by the oscillation of right cylinder (red line). The speed of particle is

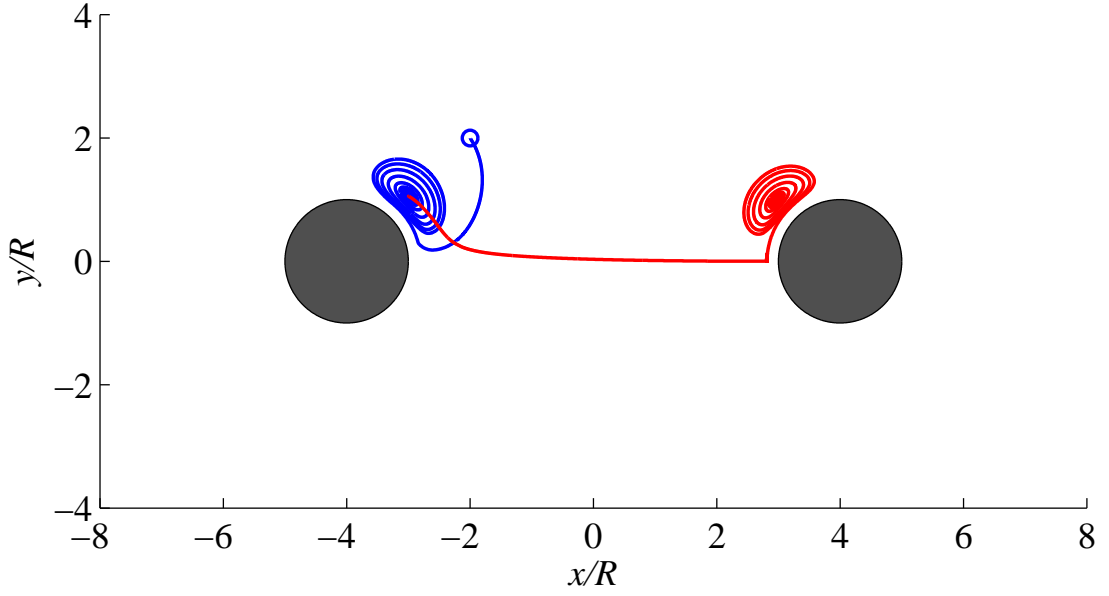


Figure 5.12: Inertial particle trajectory during the cycle  $t/T \in [0, 6784]$  (oscillation from left cylinder; blue line) and  $t/T \in [6785, 105963]$  (oscillation from right cylinder; red line) for  $Re = 40$ ,  $\epsilon = 0.1$ ,  $a/R = 0.175$  and  $\rho_p/\rho_f = 1$ . Initial location depicted with blue circle.

relatively small since the streaming motion becomes weaker after distance to the oscillator increases. In the proximity of left cylinder, however, the vorticity is still nonzero due to the interaction of still left cylinder to satisfy the no slip condition at its surface. Therefore, despite of this small streaming motion, complete modified MR equation is employed until the inertial particle escape the vortical region during long period of  $t/T \in [6785, 70957]$ .

After the inertial particle passed the vortical region and is located in non-vortical region between two cylinder, inertial particle behaves like a fluid particle since the inertial particle does not have any forcing term in this non-vortical region. As mentioned, MLV is thus employed to significantly reduce the computation efforts during  $t/T \in [70958, 97650]$ . Then inertial particle enters again into the vortical region, generated by right cylinder, in which complete modified MR

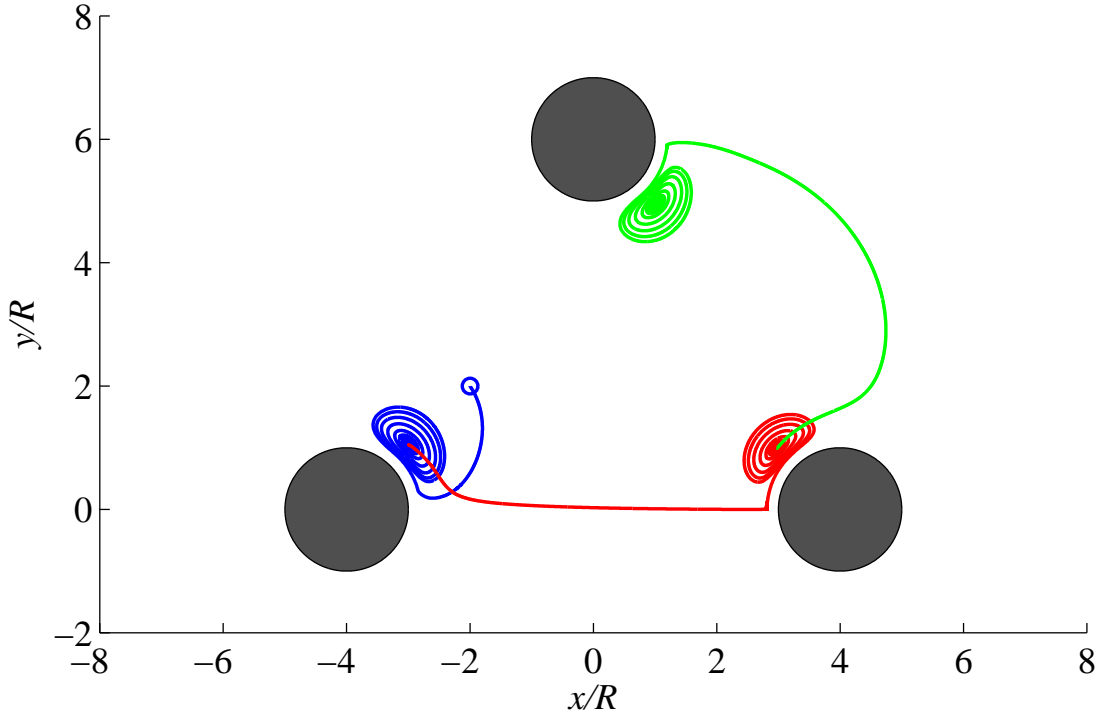


Figure 5.13: Inertial particle trajectory during the cycle  $t/T \in [0, 6784]$  (oscillation from lower left cylinder; blue line),  $t/T \in [6785, 105109]$  (oscillation from lower right cylinder; red line) and  $t/T \in [105110, 162754]$  (oscillation from upper cylinder; green line) for  $Re = 40$ ,  $\epsilon = 0.1$ ,  $a/R = 0.175$  and  $\rho_p/\rho_f = 1$ . Initial location depicted with blue circle.

equation is employed again during  $t/T \in [97651, 105963]$ . In this region, inertial particle has relatively fast speed and approaches close to the right cylinder since it followed the outmost streamline. When it is in close proximity to the right cylinder, viscous drag such as lubrication force increase and this drag suppress the acceleration of inertial particle. In this close proximity region,  $\delta < \delta_{ss}$ , elastic collision force  $W_o$  turns on several times and thus inertial particle exhibits uneven trajectory from this collision with right cylinder. After this proximity region, it is finally trapped again inside the inner streaming cell after swirling motion.

One can also transport inertial particle with oscillating cylinders in triangular

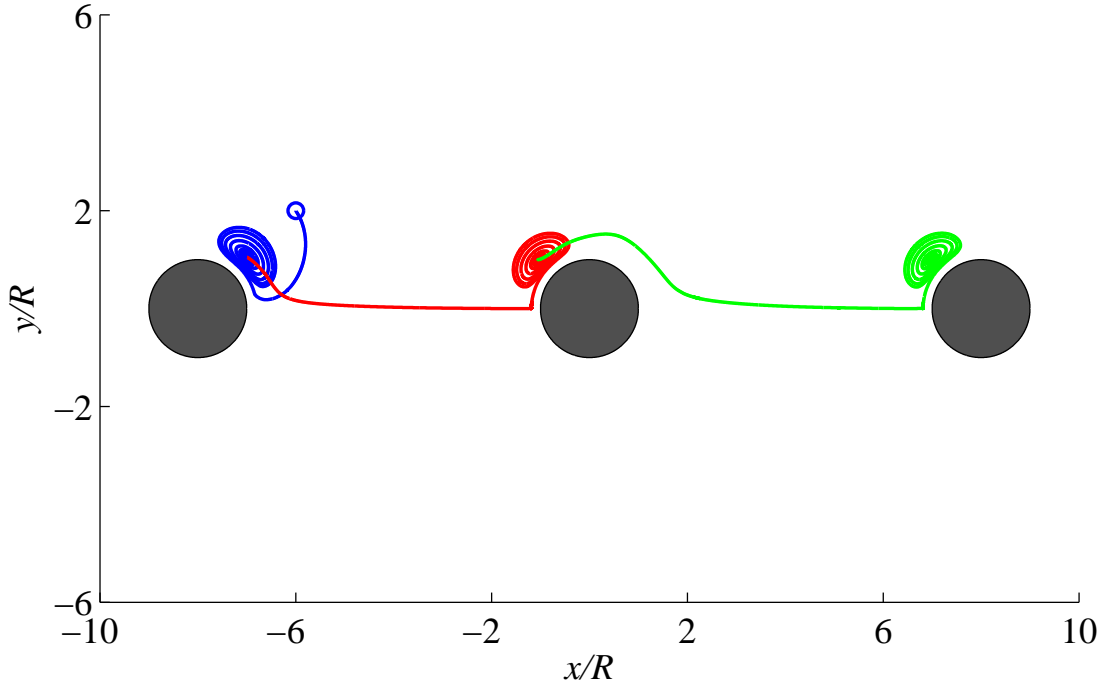


Figure 5.14: Inertial particle trajectory during the cycle  $t/T \in [0, 6784]$  (oscillation from left cylinder; blue line),  $t/T \in [6785, 105109]$  (oscillation from center cylinder; red line) and  $t/T \in [105110, 441381]$  (oscillation from right cylinder; green line) for  $Re = 40$ ,  $\epsilon = 0.1$ ,  $a/R = 0.175$  and  $\rho_p/\rho_f = 1$ . Initial location depicted with blue circle.

arrangement as in figure 5.13. Inertial particle is transported in similar manner as it is transported between two oscillating cylinder in figure . The trapped particle in the vicinity of lower right cylinder start to migrate toward upper cylinder as it follows the outmost streamline generated by upper cylinder during  $t/T \in [105110, 162754]$  (green line). Although it is not shown in this figure, the trapped particle by upper cylinder is transported back inside the center of streaming cell by lower left cylinder during  $t/T \in [162755, 239306]$ . This indicates that it is feasible to transport particles between oscillating cylinders in certain arrangement.

Inertial particle can also be transport in straight line arrangement as shown

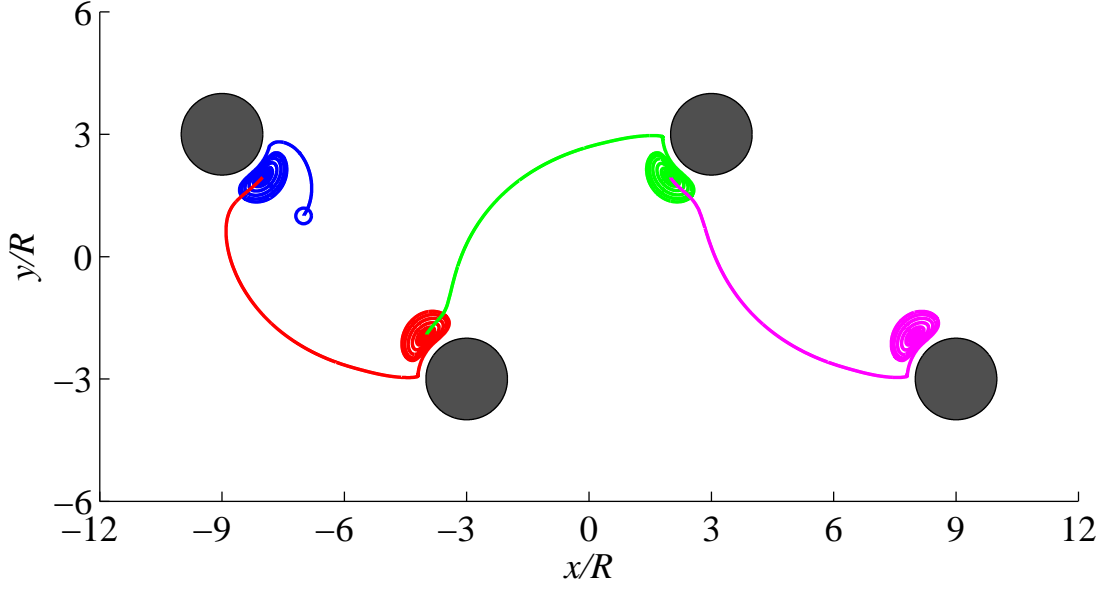


Figure 5.15: Inertial particle trajectory during the cycle  $t/T \in [0, 5891]$  (oscillation from upper left cylinder; blue line),  $t/T \in [5892, 88198]$  (oscillation from lower left cylinder; red line),  $t/T \in [88199, 202499]$  (oscillation from upper right cylinder; green line) and  $t/T \in [202500, 306366]$  (oscillation from lower right cylinder; magenta line) for  $Re = 40$ ,  $\epsilon = 0.1$ ,  $a/R = 0.175$  and  $\rho_p/\rho_f = 1$ . Initial location depicted with blue circle.

in figure 5.14. After the trapped inertial particle is transported toward the inner streaming cell generated by center cylinder during  $t/T \in [0, 6784]$  (blue line) and  $t/T \in [6785, 105109]$  (red line) respectively, it is slowly migrate toward right cylinder from the oscillation of right cylinder during  $t/T \in [105110, 441381]$  (green line). Since the streaming flow is weakly generated by the oscillation of right cylinder in the region of second quadrant of center cylinder, the migration speed of trapped inertial particle is very slow in those region. Although it is slow process, streaming flow can transport objects behind obstacles.

It took more than four hundred thousand oscillations to transport inertial particle approximately from  $(-8R, 0)$  to  $(8R, 0)$  in straight line arrangement in

figure 5.14. This transport speed can be improved if one can avoid weak streaming zone by arranging the oscillating cylinders as in figure 5.15. Similar strategy but avoiding weak streaming zone can transport inertial particle approximately from  $(-9R, 0)$  to  $(9R, 0)$  with three hundred thousand oscillations. This oscillations takes several hundreds seconds in practical experimental condition using several kilo hertz oscillation frequency.

Overall, inertial particle can be transported between oscillating cylinders inside Stokes layer in that streaming flow can drag the inertial particle into inner streaming cell and finally trap it inside the center of streaming cell. By controlled sequence of starting and stopping oscillation of cylinders, inertial particle is transported in a predictable manner. Computational effort significantly is reduced by using one oscillation cycle after the streaming flow reaches to state state as well as Mean Lagrangian Velocity (MLV) in vorticity-free region to compute the inertial particle trajectories. Inertial particle transport outside Stokes layer is dealt in next section 5.4.

## 5.4 Transport outside Stokes layer

As mentioned in chapter 3, simulations from VVPM cannot captures the correct streaming flow in outer region between oscillating cylinders due to computational efficiency. One can, however, obtain approximated outer region flow by BEM as shown in figure 5.16. The streaming flow in outer region directs flow from the direction perpendicular to oscillating axis ( $Y$  axis) to oscillating axis ( $X$  axis). Meanwhile, the flow in the region facing other cylinder need to satisfy the no slip condition on the surface of other cylinder, so that it forms closed loop of streaming cell and flow circulates around this streaming cell as the flows inside inner streaming cell. This BEM simulation serves as an approximate surrogate to capture the streaming flow between oscillating cylinders although it cannot

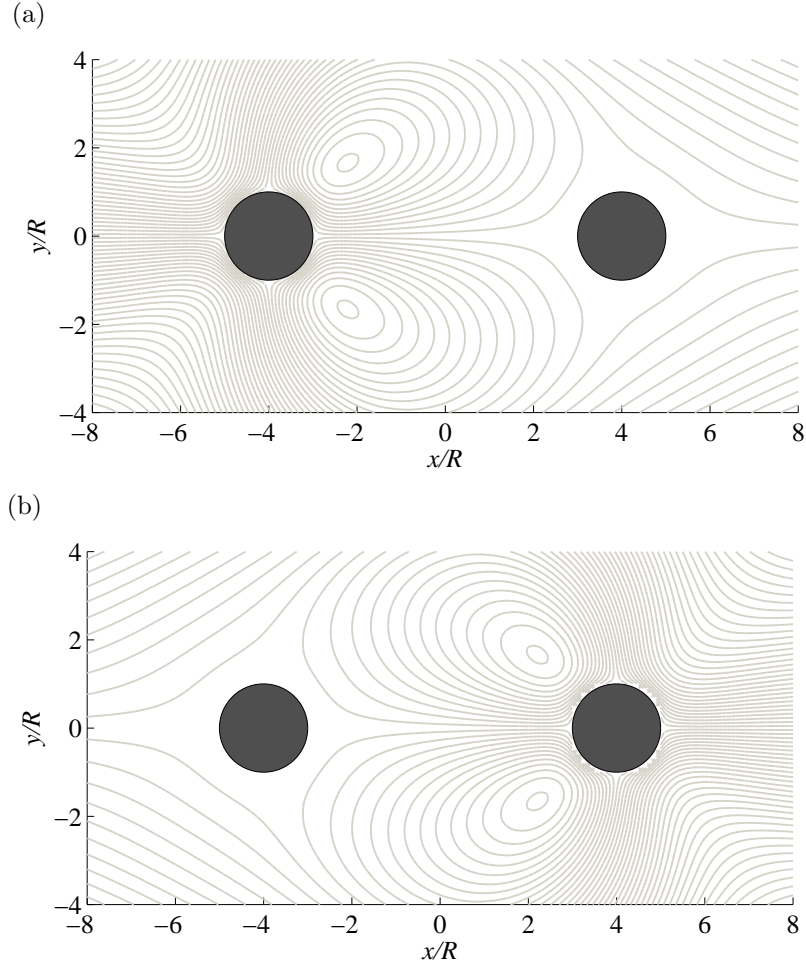


Figure 5.16: Contour of streamline of oscillating two cylinders from BEM . Streaming flows are obtained from oscillation of (a) left  $(-4R, 0)$  and (b) right  $(4R, 0)$  cylinder, respectively.

capture the inner streaming cell which is shrunk to zero.

Streaming flows between oscillating cylinders in triangular arrangement, line arrangement and zigzag arrangement from BEM are shown in figure 5.17, 5.18 and 5.19, respectively. Streaming flows exhibit similar behavior as flows are directed in the region not facing other cylinder, and circulates around the streaming cell in the region between cylinders.

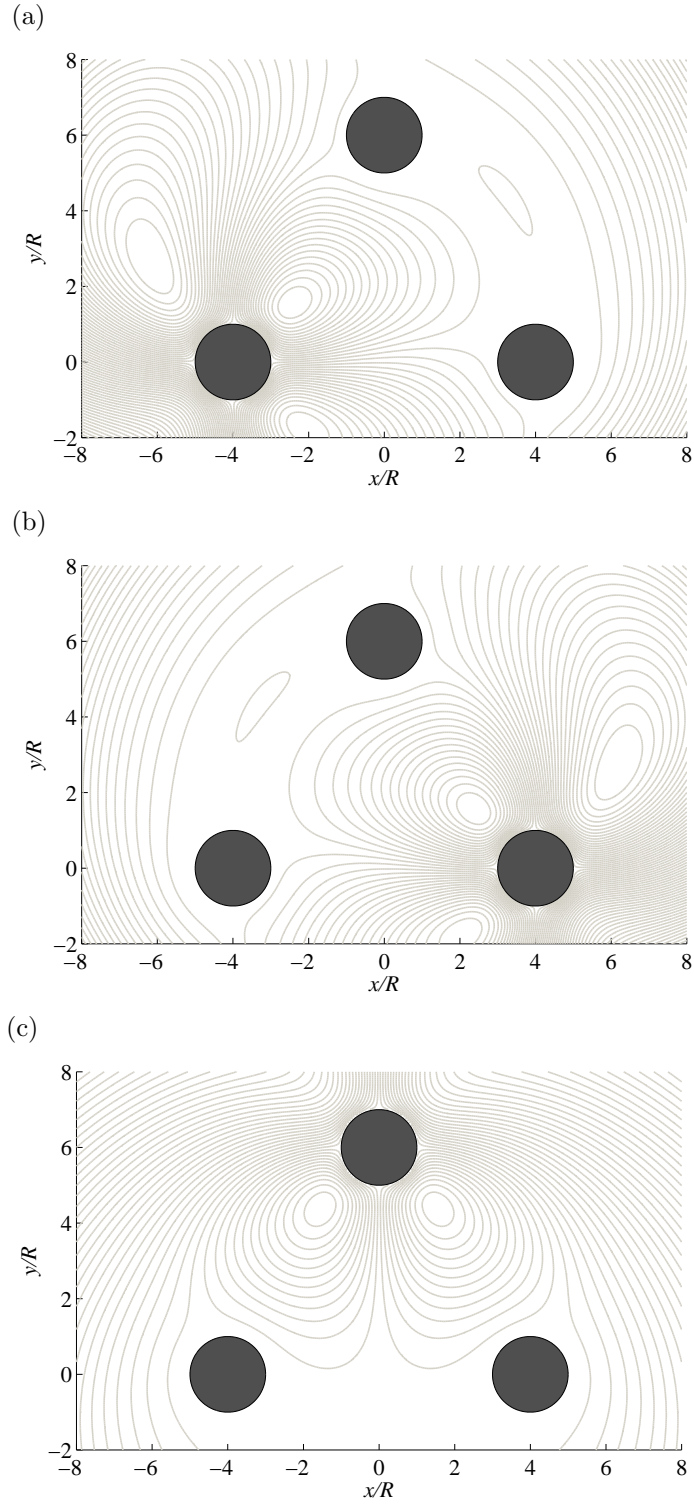


Figure 5.17: Contour of streamline of oscillating cylinders in triangular arrangement from BEM. Streaming flows are obtained from oscillation of (a) lower left  $(-4R, 0)$ , (b) lower right  $(4R, 0)$  and (c) upper  $(0, 6R)$  cylinder, respectively.



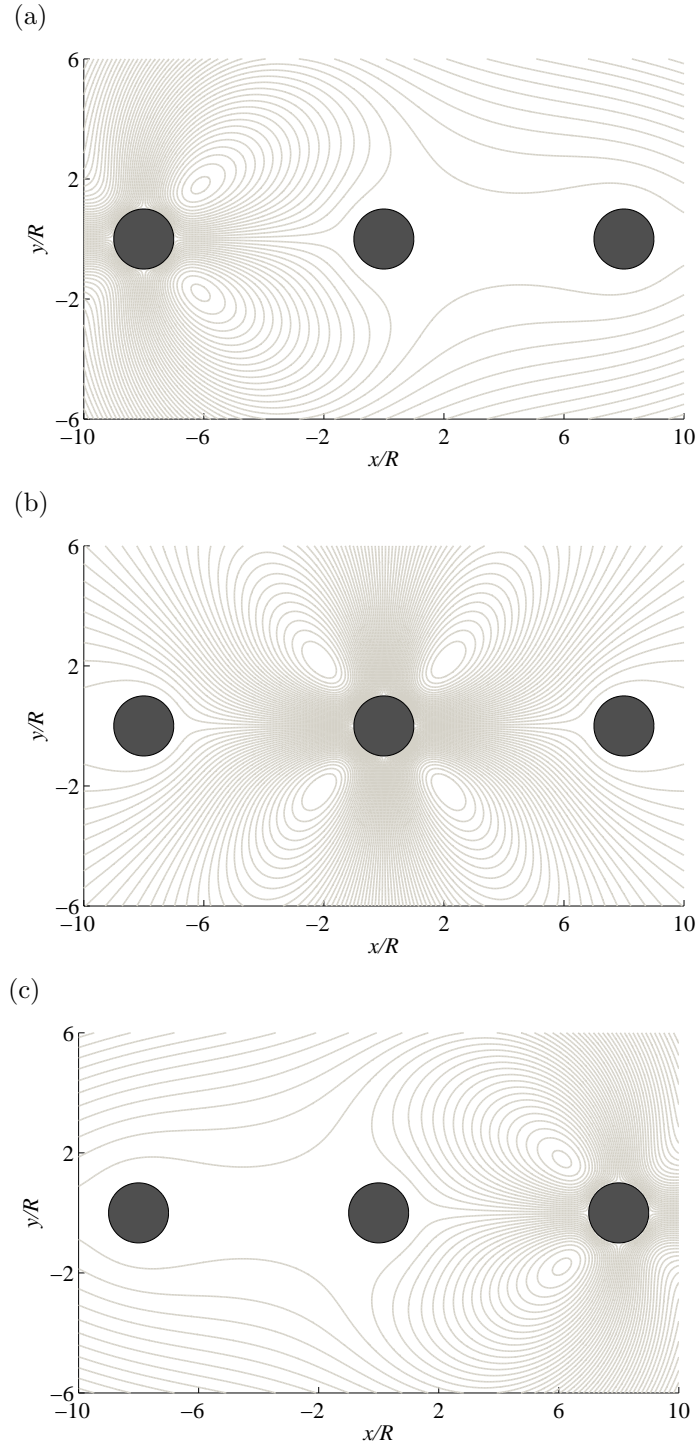


Figure 5.18: Contour of streamline of oscillating cylinders in line arrangement from BEM. Streaming flows are obtained from oscillation of (a) left  $(-8R, 0)$ , (b) center  $(0, 0)$  and (c) right  $(8R, 0)$  cylinder, respectively.

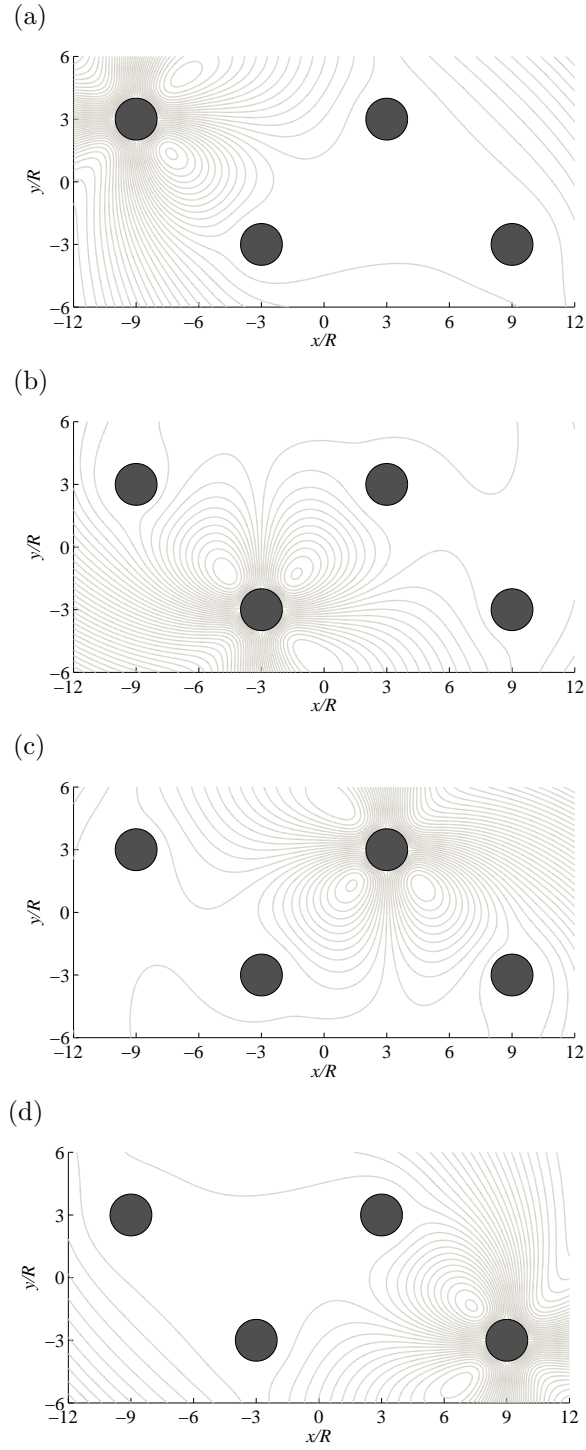


Figure 5.19: Contour of streamline of oscillating cylinders in line arrangement from BEM. Streaming flows are obtained from oscillation of (a) upper left  $(-9R, -3R)$ , (b) lower left  $(-3R, -3R)$ , (c) upper right  $(3R, 3R)$  and (d) lower right  $(9R, -3R)$  cylinder, respectively.

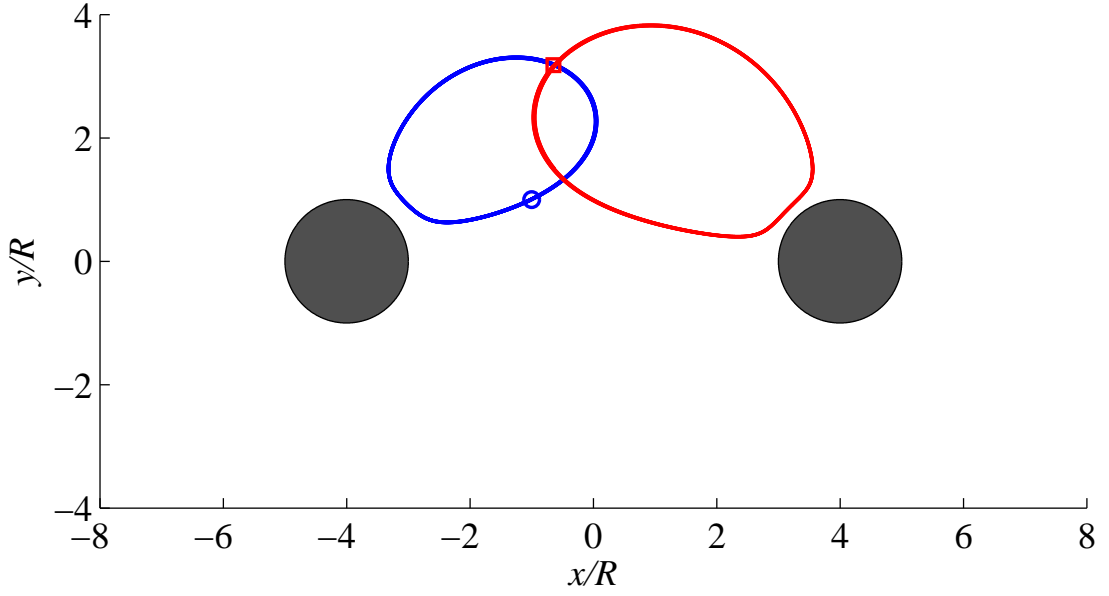


Figure 5.20: Inertial particle trajectory during the cycle  $t/T \in [0, 15934]$  (oscillation from left cylinder; blue line) and  $t/T \in [15934, 26388]$  (oscillation from right cylinder; red line) for  $Re = 40$ ,  $\epsilon = 0.1$ ,  $a/R = 0.175$  and  $\rho_p/\rho_f = 1$ . Particle's Initial location and transient location at  $t/T = 15934$  is depicted with blue circle and red square, respectively.

Inertial particle transport in outer region is considered for two oscillating cylinders in figure 5.20. The motion of inertial particle is also integrated with modified MR equation (5.6) using streaming flow from BEM in figure 5.16. Inertial particle initiates its motion in  $(-R, R)$  and undergoes slight inward spiral motion toward the center of streaming cell during  $t/T \in [1, 21105]$  (blue line). After left cylinder stop oscillating and right cylinder starts to oscillate, the inertial particle experienced spiraling clockwise around the center of streaming cell with slight inward motion is dragged toward right cylinder at  $(-2.15R, 2.47R)$  (red square), and starts to spiral counter-clockwise around the center of streaming cell generated by right cylinder with slight inward motion during  $t/T \in [21106, 37763]$ . The notable difference between this inertial particle transport in outer region and inner region

is inward motion.

In order to investigate this slight inward motion, the quantity  $\alpha$  and  $d\alpha/dt$  during the interval between  $t/T = 120$  and  $240$  is examined. Figure 5.21 (a) indicates that inertial particle experience slight inward motion as it approaches close to the cylinder but it experience smaller outward motion smaller than the previous inward motion as it recedes from the cylinder. Thus overall  $\alpha$  during this period is very small positive values compared to the values in figure 4.5, so that it experience a little inward motions. This insignificant inward motion comes from symmetric cancelation of contributions of each terms from modified MR equation. Faxén corrections terms (green line) initiates this inward motion as it approaches to the cylinder but reverse this motion as it recedes from the cylinder. Meanwhile, viscous drag term (black line) conversely acts to Faxén corrections terms, and convective term (cyan line) is almost negligible. Thus, the slight inward motion comes from the small positive Saffman lift term (blue line) which plays prominent role for inward motion.

Also the flowfield is steady second order solution of Stokes flow and thus the primary first order oscillatory flow is missing in integrating inertial particle transport trajectory. This implies that inertial forces closely related pressure type forces originating first order oscillatory motion are missing. Therefore it is necessary to enhance this approximated solution to include first order solution to correctly captures inward motion when the inertial particle is transported outside Stokes layer.

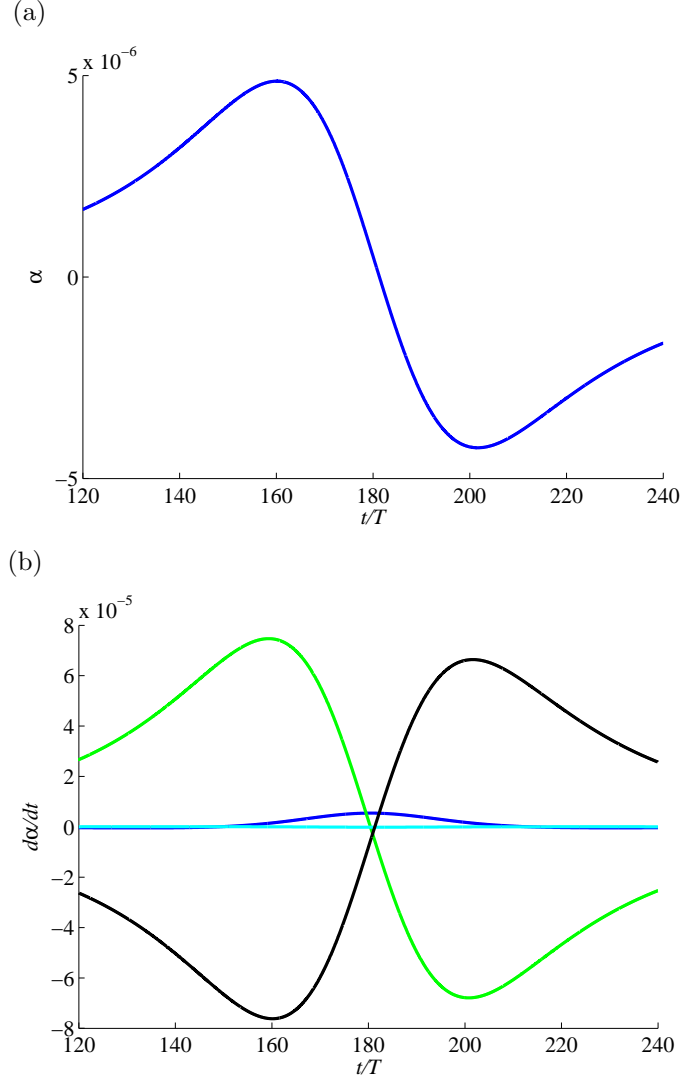


Figure 5.21: (a) History of  $\alpha$  during the cycle  $t/T \in [120, 240]$  for  $Re = 40$ ,  $a/R = 0.175$ ,  $\rho_p/\rho_f = 1$ . (b) Contributions to  $d\alpha/dt$  from each term in equation (4.5): Stokes drag (black); convective term (cyan); Saffman lift (blue); Faxén corrections (green);  $\overline{\mathbf{w}} \times d\overline{\mathbf{U}}/dt$  (yellow).

## CHAPTER 6

### Conclusion and Future Works

The behavior of inertial particles in a streaming flow generated by an oscillating circular cylinder has been examined by integrating the Maxey–Riley equation with Saffman lift force in an analytically-obtained flow field. The flowfield consists of a primary oscillatory and secondary streaming components, the latter of which consists of a set of four streaming cells surrounding the cylinder. Inertial particles released in the inner streaming cell of this flow exhibit an inward spiral toward a trapping point at the center of streaming cell, regardless of particle density, size and fluid Reynolds number. The most prominent force responsible for trapping is the Saffman lift force – which itself is activated by the Faxén corrections that divert the particle from the fluid particle trajectory – while viscous forces such as Stokes drag and the Basset history term resist this trapping.

The trapping speed for inertial particles has also been investigated. It has been found that lighter, larger particles are trapped faster, as are particles of a fixed density and particle Reynolds number at larger flow Reynolds number. These results have also shown that the particle is trapped at approximately the same location – the center of the streaming cell – regardless of its size, density, or initial location inside the cell. Particles initially outside the streaming cell, however, are repelled rather than trapped.

Inertial particle transport between multiple oscillating cylinder is also investigated. The flowfield for multiple oscillating cylinder is obtained by either high-fidelity simulation (VVPM) for transport inside Stokes layer and approximated

simulation (BEM) for transport outside Stokes layer. The transport motion is obtained by integrating the modified Maxey–Riley equation including wall effect such as lubrication force and elastic collision force. With controlled sequence of stopping and starting the oscillation inertial particle is transported in a predictable manner inside Stokes layer, while the inertial particle is transported without trapping motion due to weak inertial effect outside Stokes layers.

It has been shown that the oscillations to trap inertial particles inside the streaming cell take several thousand cycles, which is approximately couple of seconds for several kilo hertz oscillation frequency in practical experimental condition. This oscillations increase for inertial particle transport up to several hundred thousands cycles, which is approximately several hundreds seconds. This reveals that viscous streaming is an effective mechanism for microparticle trapping but transport due to the significant long transport times, which needs improvement.

Inertial particle transport take much more oscillations than particle trapping since the flow field generated by next oscillator is felt weak at current trapped position. Therefore if the transport strategy is enhanced in a manner that the current oscillator does not stop but oscillates again with next oscillator to generated streaming flow in a direction to transport the trapped particle to next designated points. With this approaches it is expected to reduce the oscillations for particle transport significantly. Also, by adding free stream flow to the direction in which inertial particle is transported, it may increase the particle transport speed without changing the streaming cell topology due to the free stream.

Moreover, inertial particle outside Stokes layer using approximated solution of Stokes flow is transported without significant inward motion. This is because the flowfield is steady second order solution of Stokes flow in which first order oscillatory flow is missing. Since it is computationally expensive to solve flowfield of multiple oscillating cylinders with high fidelity simulation, it is necessary to improve the current approximated solution of Stokes flow to include first order

oscillatory solution, so that it correctly captures the streaming flow and particle's transport motion without any significant computation efforts.



## APPENDIX A

### Analytical Solution of Coefficient Matrix

Most of derivation of coefficient matrix followed the work of Kelmanson [33].

Figure A.1 depicts the geometry of boundary segment  $\partial\Omega_j$  and notations. General field point  $p$  is located inside domain  $\Omega$  enclosed by boundary  $\partial\Omega$ .  $q_{aj}$  and  $q_{bj}$  are both endpoints of boundary segment  $\partial\Omega_j$  whose length is given by  $h$ .  $\mathbf{n}$  is unit normal vector of  $\partial\Omega$ ,

$$\begin{aligned} a &= |p - q_{aj}|, \\ b &= |p - q_{bj}|, \\ h &= |q_{aj} - q_{bj}|, \\ \beta &= \angle q_{bj}q_{aj}p, \\ \zeta &= \angle q_{aj}pq_{bj} \end{aligned} \tag{A.1}$$

Then analytic expressions for the integrals in (3.35) - (3.38) are

$$\int_{q \in \partial\Omega_j} \log' |q_i - q| d\omega(q) = \zeta, \tag{A.2}$$

$$\int_{q \in \partial\Omega_j} \log |q_i - q| d\omega(q) = a(\log a - \log b) \cos \beta + h \log b - h + a\zeta \sin \beta \equiv I, \tag{A.3}$$

$$\int_{q \in \partial\Omega_j} \left\{ |q_i - q|^2 \log |q_i - q| - |q_i - q|^2 \right\}' d\omega(q) = a(2I - h) \sin \beta, \tag{A.4}$$

$$\begin{aligned} & \int_{q \in \partial\Omega_j} \left\{ |q_i - q|^2 \log |q_i - q| - |q_i - q|^2 \right\} d\omega(q) \\ &= \frac{1}{3} \left\{ (h - a \cos \beta)^3 (\log b - \frac{4}{3}) + (a \cos \beta)^3 (\log a - \frac{4}{3}) \right\} \\ &+ (a \sin \beta)^2 \left\{ I - \frac{2}{3}h - \frac{1}{3}a\zeta \sin \beta \right\} \end{aligned} \tag{A.5}$$

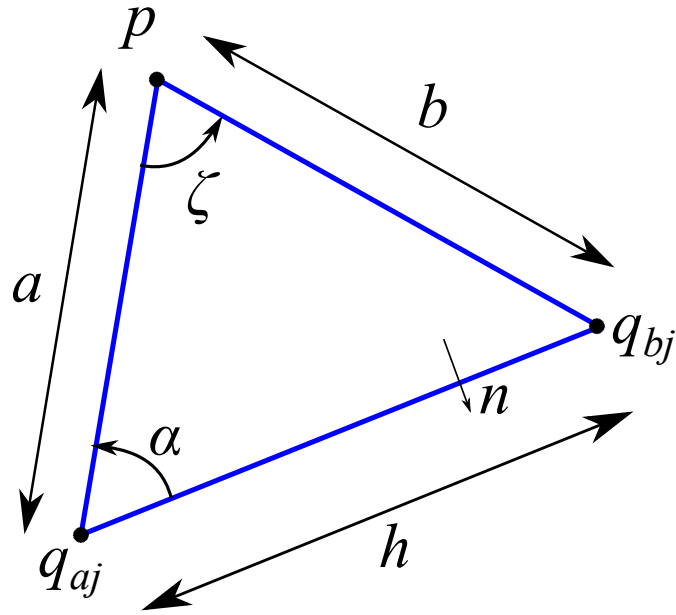


Figure A.1: Geometry of boundary segment  $\partial\Omega_j$  and notations for analytic solution of integration.

## REFERENCES

- [1] E. N. da C. Andrade. On the circulations caused by the vibration of air in a tube. *Proc. R. Soc. Lond. A*, 134:445–470, 1931.
- [2] J. M. Andres and U. Ingard. Acoustic streaming at low Reynolds numbers. *J. Acoust. Soc. Am.*, 25(5):932–938, 1953.
- [3] A. Ashkin. Acceleration and trapping of particles by radiation pressure. *Phys. Rev. Lett.*, 24(4), 1970.
- [4] A. B. Basset. *A Treatise on Hydrodynamics, Vol. II*. Deighton, Bell, London, 1888.
- [5] G. K. Batchelor. *An introduction to fluid dynamics*. Cambridge University Press, Cambridge, UK, 1967.
- [6] J. T. Beale. On the accuracy of vortex method at large times. Workshop on comput. Fluid Dyn. and React. Gas Flows, 1986.
- [7] A. Bertelsen, A. Svardal, and S. Tjøtta. Nonlinear streaming effects associated with oscillating cylinders. *J. Fluid Mech.*, 59(3):493–511, 1973.
- [8] T. A. Bongso, A. H. Sathananthan, P. C. Wong, S. S. Ratnam, S. C. Ng, C. Anandakumar, and S. Ganatra. Human fertilization by micro-injection of immotile spermatozoa. *Human Reproduction*, 4:175–179, 1989.
- [9] J. Boussinesq. *Theorie Analytique de la Chaleur, Vol II*. L'Ecole Polytechnique, Paris, 1903.
- [10] F. Candelier, J. R. Angilella, and M. Souhar. On the effect of the Boussinesq–Basset force on the radial migration of a Stokes particle in a vortex. *Phys. Fluids*, 16:1765–1776, 2004.
- [11] F. Candelier, J. R. Angilella, and M. Souhar. On the effect of inertia and history forces on the slow motion of a spherical solid or gaseous inclusion in a solid-body rotation flow. *J. Fluid Mech.*, 545:113–139, 2005.
- [12] J. Carrier, L. Greensgard, and V. Rohklin. A fast adaptive multipole algorithm for particle simulations. *SIAM J. Sci. and Stat. Comput.*, 9(4):669–686, 1988.
- [13] P. Y. Chiou, A. T. Ohta, and M. C. Wu. Massively parallel manipulation of single cells and microparticles using optical images. *Nature*, 436:370–372, 2005.
- [14] J.-P. Choquin and J.-H. Cottet. Sur l'analyse d'une classe de méthodes de vortex tridimensionnelles. *C.R. Acad. Sci. Paris*, 306:247–273, 1988.

- [15] A. J. Chorin. Numerical study of slightly viscous flow. *J. Fluid Mech.*, 57, 1973.
- [16] G. H. Cottet. Large time behavior of deterministic particle approximations to the navier-stokes equations. *Math. Comput.*, 56:45–59, 1991.
- [17] G. H. Cottet and Koumoutsakos P. *Vortex Method: Theory and Applications*. Cambridge Univ. Press, Cambridge, UK, 2000.
- [18] Anton Daitche and Tamás Tél. Memory effects are relevant for chaotic advection of inertial particles. *Phys. Rev. Lett.*, 107:244501, 2011.
- [19] P. Degond and S. Mas-Gallic. The weighted particle method for convection-diffusion equations. i. the case of an isotropic viscosity; ii. the anisotropic case. *Math Comput.*, 53(188):485–507, 1989.
- [20] Dino Di Carlo, Nima Aghdam, and Luke P. Lee. Single-cell enzyme concentrations, kinetics, and inhibition analysis using high-density hydrodynamic cell isolation arrays. *Anal. Chem.*, 78:4925–4930, 2006.
- [21] Dino Di Carlo, Liz Y. Wu, and Luke P. Lee. Dynamic single cell culture array. *Lab on a Chip*, 6:1445–1449, 2006.
- [22] J. Eldredge. Numerical simulation of the fluid dynamics of 2d rigid body motion with the vortex particle method. To be published, 2006.
- [23] J. D. Eldredge, T. Colonius, and A. Leonard. A vortex particle method for two-dimensional compressible flow. *J. Comput. Phys.*, 179:371–399, 2002.
- [24] H. E. Fettis. On the integration of a class of differential equations occurring in boundary-layers and other hydrodynamic problems. In *Proc. 4th Mid West Conf. Fluid Mech.*, volume 128, pages 93–114. Purdue University, 1955.
- [25] D. J. Shippy G. Fairweather, F. J. Rizzo and Y. S. Wu. On the numerical solution of two-dimensional potential problems by an improved boundary integral equation method. *J. Comput. Phys.*, 31:96–112, 1979.
- [26] L. Greengard and V. Rokhlin. A fast algorithm for particle simulations. *J. Comput. Phys.*, 73(2):325–348, 1987.
- [27] Albrecht Haake, Adrian Neild, Gerald Radziwill, and Jurg Dual. Positioning, displacement, and localization of cells using ultrasonic forces. *Biotechnology and Bioengineering*, 92(1), 2005.
- [28] O. H. Hald. Convergence of vortex methods for Euler’s equations, II. *SIAM J. Numer. Anal.*, 16:726–755, 1979.
- [29] H. M. Hertz. Standing-wave acoustic trap for nonintrusive positioning of microparticles. *J. Appl. Phys.*, 78:4845–4849, 1995.

- [30] J. Holtmark, I. Johnsen, T. Sikkeland, and S. Skavlem. Boundary layer flow near a cylindrical obstacle in an oscillating, incompressible fluid. *J. Acoust. Soc. Am.*, 26(1):26–39, 1954.
- [31] M. P. Hughes. Strategies for dielectrophoretic separation in laboratory-on-a-chip systems. *Electrophoresis*, 23:2569–2582, 2002.
- [32] Li jeany Zhang and Jeff D. Eldredge. A viscous vortex particle method for deforming bodies with application to biolocomotion. *Int. J. Numer. Metho. Fluids*, 59:1299–1320, 2009.
- [33] M. A. Kelmanson. An integral equation method for the solution of singular slow flow problems. *J. Comput. Phys.*, 51:139–158, 1983.
- [34] P. Koumoutsakos, A. Leonard, and F. Pepin. Boundary conditions for viscous vortex methods. *Journal of Comput. Phys.*, 113(1):52–61, 1994.
- [35] Stuart Smith Kwitae Chong, Scott D. Kelly and Jeff D. Eldredge. Inertial particle trapping in viscous streaming. *Phys. Fluids*, 25:033602, 2013.
- [36] A. Leonard. Review: Vortex methods for flow simulations. *J. of Comput. Phys.*, 37(3):289–335, 1980.
- [37] A. Leonard. Computing three-dimensional incompressible flows with vortex elements. *Annu. Rev. Fluid Mech.*, 17:523–559, 1985.
- [38] A. Leonard, D. Shiels, J. K. Salmon, G. S. Winckelmans, and P. Ploumhans. Recent advances in high resolution vortex methods for incompressible flows. In *13th AIAA Computational Fluid Dynamics Conf.*, Snowmass Village, CO, 1997.
- [39] Paul C. H. Li, Laurent de Camprieux, Jia Caia, and Monika Sangar. Transport, retention and fluorescent measurement of single biological cells studied in microfluidic chips.
- [40] V. H. Lieu, T. A. House, and D. T. Schwartz. Hydrodynamic tweezers: Impact of design geometry on flow and microparticle trapping. *Anal. Chem.*, 84:1963–1968, 2012.
- [41] M. J. Lighthill. Introduction: Boundary layer theory. In L. Rosenhead, editor, *Laminar Boundary Layers*. Clarendon Press, 1961.
- [42] M. S. Longuet-Higgins. Mass transport in water waves. *Phil. Trans. R. Soc. Lond. A*, 245(903):535–581, 1953.
- [43] B. R. Lutz. personal communication, June 2012.

- [44] Barry R. Lutz, Jian Chen, and Daniel T. Schwartz. Microscopic steady streaming eddies created around short cylinders in a channel: Flow visualization and Stokes layer scaling. *Phys. Fluids*, 17:023601, 2005.
- [45] Barry R. Lutz, Jian Chen, and Daniel T. Schwartz. Hydrodynamic tweezers: 1. Noncontact trapping of single cells using steady streaming microeddies. *Anal. Chem.*, 78:5429–5435, 2006.
- [46] P. Marmottant, J. P. Raven, H. Gardeniers, J. G. Bomer, and S. Hilgenfeldt. Microfluidics with ultrasound-driven bubbles. *J. Fluid Mech.*, 568:109–118, 2006.
- [47] Philippe Marmottant and Sascha Hilgenfeldt. Microacoustics: Controlled vesicle deformation and lysis by single oscillating bubbles. *Nature*, 423:153–156, 2003.
- [48] Philippe Marmottant and Sascha Hilgenfeldt. A bubble-driven microfluidic transport element for bioengineering. *Proc. Natl. Acad. Sci.*, 101:9523–9527, 2004.
- [49] M. R. Maxey and J. J. Riley. Equation of motion for a small rigid sphere in a nonuniform flow. *Phys. Fluids*, 26(4):883–889, 1983.
- [50] D. L. Miller. Particle gathering and microstreaming near ultrasonically activated gas-filled micropores. *J. Acoust. Soc. Am.*, 84(4):1378–1387, 1988.
- [51] J. E. Molloy and M. J. Padgett. Lights, action: optical tweezers. *Contemp. Phys.*, 43:241–258, 2002.
- [52] J. J. Monaghan. Particle methods for hydrodynamics. *Comp. Phys. Rep.*, 3:71–124, 1985.
- [53] N. Mordant and J.-F. Pinton. Velocity measurement of a settling sphere. *Eur. Phys. J. B*, 18:343–352, 2000.
- [54] M. Oishi Nagai, N. Sakaki, O. Ducloux, M. Oshima, H. Asai, and H. Fujita. Application of vorticella’s feeding mechanism as a micromixer – characterization of vortices generated by cilia motion. In *Proceedings of the 21st IEEE International Conference on Micro Electro Mechanical Systems*, pages 555–558, 2008.
- [55] Jeroen H. Nieuwenhuis, Artur Jachimowicz, Peter Svasek, and Michiel J. Vellekoop. Optimization of microfluidic particle sorters based on dielectrophoresis. *IEEE Sensors Journal*, 5(5):810–816, 2005.
- [56] B. K. Nowakowski, S. T. Smith, B. A. Mullany, and S. C. Woody. Vortex machining : Locallized surface modification using an oscillation fiber probe. *Machining Science and Technology*, 13:561–570, 2009.

- [57] C. W. Oseen. *Neuere Methoden und Ergebnisse in der Hydrodynamik*. Akademische Verlagsgesellschaft, Leipzig, 1927.
- [58] R. L. Panton. *Incompressible Flow*. John Wiley and Sons, New York, 2nd edition, 1996.
- [59] Jungyul Park, Seng-Hwan Jung, Young-Ho Kim, Byungkyu Kim, Seung-Ki Leeb, and Jong-Oh Park. Design and fabrication of an integrated cell processor for single embryo cell manipulation. *Lab Chip*, 5, 2005.
- [60] Xing Yue (Larry) Peng and Paul C. H. Li. A three-dimensional flow control concept for single-cell experiments on a microchip. 1. cell selection, cell retention, cell culture, cell balancing, and cell scanning.
- [61] P. Ploumhans and G. S. Winckelmans. Vortex methods for high-resolution simulations of viscous flow past bluff bodies of general geometry. *J. of Comput. Phys.*, 165(2):354–406, 2000.
- [62] P. Ploumhans and G. S. Winckelmans. Vortex methods for direct numerical simulation for three-dimensional bluff body flows: application to the sphere at  $Re=300$ , 500 and 1000. *J. of Comput. Phys.*, 178:427–463, 2002.
- [63] P. Ploumhans, G. S. Winckelmans, and Salmon J. K. Vortex particles and tree codes. i. flows with arbitrary crossing between solid boundaries and particle redistribution lattice; ii. vortex ring encountering a plane at an angle. In *Third International Workshop on Vortex Flows and Related Numerical Methods*, Toulouse, 1998.
- [64] Ales Prokop, Zdenka Prokop, David Schaffer, Eugene Kozlov, John Wikswo, David Cliffl, and Franz Baudenbacher. Nanoliterbioreactor: Long-term mammalian cell culture at nanofabricated scale.
- [65] W. P. Raney, J. C. Corelli, and P. J. Westervelt. Acoustical streaming in the vicinity of a cylinder. *J. Acoust. Soc. Am.*, 26(6):1006–1014, 1954.
- [66] Lord Rayleigh. On the circulation of air observed in Kundt’s tubes, and on some allied acoustical problems. *Phil. Trans. R. Soc. Lond.*, 175:1–21, 1884.
- [67] C. Rehbach. Numerical calculation of three-dimensional unsteady flows with vortex sheets. *AIAA*, 1978.
- [68] N. Riley. Oscillating viscous flows. *Mathematika*, 12:161–175, 1965.
- [69] N Riley. Steady streaming. *Annual Reviews of Fluid Mechanics*, 33:43–65, 2001.
- [70] L. Rosenhead. The formation of vortices from a surface of discontinuity. In *Proceedings of the Royal Society of London. Series A*, volume 134. The Royal Society, 1931.

- [71] L. Rosenhead. The point vortex approximation of a vortex sheet. In *Proceedings of the Royal Society of London. Series A*, volume 134. The Royal Society, 1932.
- [72] Youcef Saad and Martin H. Schultz. Gmres : A generalized minimal residual algorithm for solving nonsymmetric linear systems. *SIAM J. Sci. Stat. Comput.*, 7(3):856–869, 1986.
- [73] P. G. Saffman. The lift on a small sphere in a slow shear flow. *J. Fluid Mech.*, 22:385–400, 1965.
- [74] H. Schlichting. Berechnung ebener periodischer Grenzschichtströmungen. *Physikal. Z.*, 33:327–335, 1932.
- [75] J. Seo, C. Ionescu-Zanetti, J. Diamond, R. Lal, and L. P. Lee. Integrated multiple patch-clamp array chip via lateral celltrapping junctions. *Appl. Phys. Lett.*, 84, 2004.
- [76] Martin B. Short, Cristian A. Solari, Sujoy Ganguly, Thomas R. Powers, John O. Kessler, and Raymond E. Goldstein. Flows driven by flagella of multicellular organisms enhance long-range molecular transport. *Proc. Natl. Acad. Sci.*, 103(22), 2006.
- [77] J.T. Stuart. Double boundary layers in oscillatory viscous flow. *J. Fluid Mech.*, 24:673–687, 1966.
- [78] C. M. Tchen. *Mean values and correlation problems connected with the motion of small particles suspended in a turbulent fluid*. PhD thesis, Delft University of Technology, 1947.
- [79] Jerry P. Gollub Themistoklis P. Sapsis, Nicholas T. Ouellette and George Haller. Neutrally buoyant particle dynamics in fluid flows: Comparison of experiments with lagrangian stochastic models. *Phys. Fluids*, 23:093304, 2011.
- [80] S. P. Timoshenko and J. N. Goodier. *Theory of Elasticity, 3rd edn*. McGraw Hill, 1970.
- [81] K. K. Tio, A. Liñán, J. C. Lasheras, and A. M. Gañán-Calvo. On the dynamics of buoyant and heavy particles in a periodic Stuart vortex flow. *J. Fluid Mech.*, 254:671–699, 1993.
- [82] M. A. T. van Hinsberg, J. H. M. ten Thijs Boonkkamp, and H. J. J. Clercx. An efficient, second order method for the approximation of the Basset history force. *J. Comput. Phys.*, 230:1465–1478, 2011.
- [83] S. Vogel. *Comparative Biomechanics: Lifes Physical World*. Princeton University Press, 2003.



- [84] C. Wang, S. V. Jalikop, and S. Hilgenfeldt. Size-sensitive sorting of microparticles through control of flow geometry. *Appl. Phys. Lett.*, 99:034101, 2011.
- [85] Chang-Yi Wang. On high-frequency oscillatory viscous flows. *J. Fluid Mech.*, 32(1):55–68, 1968.
- [86] Aaron R. Wheeler, William R. Thordset, Rebecca J. Whelan, Andrew M. Leach, Richard N. Zare, Yish Hann Liao, Kevin Farrell, Ian D. Manger, and Antoine Daridon. Microfluidic device for single-cell analysis.
- [87] G. S. Winckelmans and Leonard A. Contributions to vortex particle methods for the computation of three-dimensional incompressible unsteady flows. *J. Comput. Phys.*, 109:247–273, 1993.
- [88] J. C. Wu. A theory for aerodynamic forces and moments. Georgia Institute of Technology Rept., June 1978.
- [89] Junru Wu. Acoustical tweezers. *J. Acoust. Soc. Am.*, 89:2140–2143, 1991.
- [90] Melany L. Hunt Xiaobai Li and Tim Colonius. A contact model for normal immersed collisions between a particle and a wall. *J. Fluid Mech.*, 691:123–145, 2012.
- [91] Y. Yamakoshi, Y.; Noguchi. Micro particle trapping by opposite phases ultrasonic travelling waves. *Ultrasonics*, 36:873–878, 1998.
- [92] Mengsu Yang, Cheuk-Wing Li, and Jun Yang. Cell docking and on-chip monitoring of cellular reactions with a controlled concentration gradient on a microfluidic device.